University of Naples Federico II

Department of Physics "Ettore Pancini"

XXXVIII Cycle of the Doctorate School

Doctoral Dissertation in Physics

Multi-Level Assessment of 5G Electromagnetic Human Exposure

Author
Francesca Lodato

Supervisors
Prof. Rita Massa
University of Naples Federico II, Naples, Italy

Prof. Maxim Zhadobov
University of Rennes, CNRS, IETR, Rennes, France

Chapter 5 and Chapter 6 of this dissertation are under embargo

This doctoral dissertation was developed under an international co-direction agreement between the University of Naples "Federico II", Department of Physics "Ettore Pancini" (Naples, Italy) and the University of Rennes, "Institut d'Electronique et des Technologies du numéRique (IETR)" (Rennes, France).

Acknowledgements

The research activities carried out in this thesis were supported by the European Union under the Italian National Recovery and Resilience Plan (NRRP) of NextGenerationEU, partnership on "Telecommunications of the Future" (PE00000001 - program "RESTART", Structural Project 6GWINET) and the thesis project proposal was awarded by the "France Excellence Program 2024".

Abstract

The rising trend of data traffic, driven by the demands of applications with increasing performances, calls for fast, reliable, and high-capacity telecommunication networks. This challenging growth represents a significant opportunity for the development of a novel telecommunication infrastructure that is progressing through a wider communication bandwidth like those used in Industry 4.0 for edge-computing or the Internet of Things. Indeed, fourth generation (4G) networks appear to be insufficient to fulfill the requirements associated with latency and quality of the data transmitted. These issues have a common solution that the scientific community has identified in fifth generation (5G) communications technologies. As a matter of fact, the progress achieved with 5G and beyond networks is well known for the enhancements introduced in telecommunications, providing at the same time key advantages in many fields of application, notably digital healthcare services, smart cities or autonomous vehicles. Although 5G systems are becoming a commercial reality, there is already significant interest in systems beyond 5G, referred to as the sixth generation (6G) of wireless systems. To achieve high performance, 5G systems rely on the employment of advanced communication technologies together with the exploitation of unutilized high-frequency spectrum. However, these technologies gave rise to new propagation scenarios in which information about electromagnetic field levels are extremely relevant. Indeed, moving to higher frequencies, in particular to the millimeter wave (mmWave) spectrum, demonstrated a significant increment of signal propagation losses, resulting in a high signal attenuation. Furthermore, the use of mmWave spectrum introduced new exposure scenarios for the population due to the higher frequencies involved. This generated concerns about the safety of these new technologies in relation to their interactions with human body and at the same time the necessity to employ advanced strategies to enhance the signal strength and ensure a sufficient network coverage. Nevertheless, providing a good coverage while complying with human exposure limits is currently a big challenge for 5G systems. A lot of attention has been focused on these issues, but more work is needed to

understand how new 5G technologies might impact on human exposure and assure the compliance of mmWave technologies with existing exposure guidelines before their introduction on the market. In this thesis, the problem of human exposure assessment at 5G frequencies is faced at two levels: population and skin level. More in detail, computational and experimental analyses are carried out to assess population exposure in different real propagation scenarios, supporting the deployment of 5G systems with essential information for their safe widespread. Furthermore, human body exposure at skin level is investigated, providing reliable and innovative methodologies for dosimetry evaluations at mmWaves.

Contents

List of Figures

List of Tables

List of Acronyms

Acronym	Meaning
1G	first generation
3GPP	3rd Generation Partnership Project
4G	fourth generation
5G	fifth generation
6G	sixth generation
AAS	Active Antenna System
APD	Absorbed Power Density
BS	Base Station
CDF	Cumulative Distribution Function
DAK	Dielectric Assessment Kit
E-CDF	Empirical Cumulative Distribution Function
EIRP	Equivalent Isotropic Radiated Power
FCC	Federal Communications Commission
FDTD	Finite-Difference Time-Domain
GTD	Geometry Theory of Diffraction
HP	Horizontal Plane
ICNIRP	International Commission on Non Ionizing Radiation Protection
IDL	Interactive Data Language
IR	InfraRed
LOS	Line Of Sight
mmWave	millimeterWave
MIMO	Multiple Input Multiple Output
N-LOS	Non Line Of Sight
NIR	Non Ionizing Radiation
NR	New Radio
OTA	Over The Air

PBCH	Physical Broadcast Channel
PCI	Physical Cell Identity
PDMS	polydimethylsiloxane
PEP	polyethylene powder
REs	Resource Elements
RF	Radio Frequency
RSRP	Reference Signal Received Power
SAR	Specific Absorption Rate
SAWAP	Small Area Wireless Access Point
SBR	Shooting Bouncing Rays
SNR	Signal to Noise Ratio
SPEAG	Switzerland-based company Schmid and Partner Engineering AG
SS	Synchronisation Signal
SSS	Secondary Synchronisation Signal
STD	Standard Deviation
TE	Transverse Electric
TEM	Transverse Electro Magnetic
TM	Transverse Magnetic
TX	Triton X
UE	User Equipment
UTD	Uniform Theory of Diffraction
VNA	Vector Network Analyzer
VP	Vertical Plane
VPL	Vertical Plane Launch
WHO	World Health Organization

List of Symbols

Symbol	Unit	Description
δ	m	Depth of Penetration (Skin Depth)
ε	F/m	Absolute Complex Permittivity
ε_0	F/m	Permittivity of Vacuum
ε_r^*	-	Relative Complex Permittivity
ε_r	-	Real Part of Relative Complex Permittivity
ε_i	-	Imaginary Part of Relative Complex Permittivity
λ	m	Wavelength
μ	H/m	Absolute Complex Permeability
μ_0	H/m	Permeability of Vacuum
μ_r^*	-	Relative Complex Permeability
ρ	$\mathrm{kg/m^3}$	Density
σ	S/m	Electrical Conductivity
ω	rad/s	Angular Frequency
ω_b	$\mathrm{s^{-1}}$	Blood Perfusion Rate
A	-	Absorption Coefficient
c	m/s	Speed of Light
$c_{p,t}$	$\mathrm{J/(kg \cdot K)}$	Specific Heat at Constant Pressure
E	V/m	Electric Field
f	Hz	Frequency
H	A/m	Magnetic Field
h	$\mathrm{W/(m^2{\cdot}K)}$	Heat Transfer Coefficient
h_p	$\mathrm{J \cdot s}$	Planck's constant
i	-	Imaginary Unit
k_t	$\mathrm{W/(m \cdot K)}$	Thermal Conductivity
m	kg	Mass
P_{diss}	W	Dissipated Power

P_{RX}	W	Received Power
R	-	Power Reflection Coefficient
r	-	Reflection Coefficient
T	°C	Temperature
S_{inc}	W/m^2	Incident Power Density
t	s	Time
t	-	Transmission Coefficient
V	m^3	Volume
W	J	Energy

Chapter 1

Introduction

In this Chapter an overview of 5G systems main features is provided. The basic concepts of electromagnetic fields interaction with human body at 5G frequencies are introduced, together with the definition of exposure limits according to current guidelines. Main challenges introduced by new 5G technologies are discussed and the research question of this thesis is defined.

1.1 Insight on 5G Key Technologies

The increasing demand for high data rates, lower latencies, amount of transmitted data, and number of simultaneously connected devices has driven the transition from 4G to 5G systems. Indeed, 5G technologies promise to provide fast and reliable telecommunications, enabling the connection not just between people but also between things, with significant improvements in different fields of applications such as smart cities, automotive, smart healthcare, smart homes, and Internet of Things [1], [2], [3], [4], [5]. To satisfy these requirements, one of the key features introduced by new 5G networks is the employment of higher frequencies, up to the mmWave spectrum, involving frequencies from 24 GHz up to 300 GHz [6], [7]. Indeed, moving to higher frequencies offers orders of magnitude greater bandwidths that can be easily 200 times greater than all cellular allocations under 3 GHz [8], [9], [10], [11], allowing to overcome the global bandwidth shortage. On the other hand, exploring the mmWave spectrum requires careful consideration of signal attenuation, since the increase in frequency also results in higher path-loss attenuation [11], [12].
Moreover, due to the small wavelengths, the interaction between electromagnetic fields and atmospheric agents, including rain and fog, may lead to a further increase in signal attenuation due to absorption and scattering phenomena [6], [8], [10], [11].

For these reasons, the coverage area of 5G networks decreases significantly with respect to previous generation systems, and new 5G base stations (BS) can serve only cells of about 100 meters, that are named "micro cells" [6], [13]. This means that to ensure the high performances promised by 5G technologies and to increase the area spectral efficiency, a massive installation of antennas is needed in large environments, with several small access points [7], as represented in Fig. 1.1. Indeed, small-cell BS represents a turning point to explore the full potential of 5G networks, expanding the network in urban areas, densely populated regions, indoor environments, and low-coverage zones [14].
In addition to this, to ensure a reliable connection and increase the signal strength, 5G systems employ other techniques, such as massive Multiple Input Multiple Output (MIMO), beamforming and beam steering. Indeed, massive MIMO is a configuration in which the BS is usually equipped with a very large number of antennas, organized as an array, operated fully coherently and adaptively to serve multiple users devices, each equipped with one or more antennas [15]. A comparison between conventional and massive MIMO antenna is shown in Fig. 1.2. The beamforming technique is employed if the multiple antennas transmit the same signal at an identical wavelength and phase, generating a single more focused beam, and increasing in this way the spectrum and energy efficiency [16]. On the other hand, with the beam sweeping and beam steering the phase of the input signal on all radiating elements is changed, allowing the signal to be targeted at a receiver that is located in a specific position [17], and to follow interactively the user's movements. A schematic representation of beamforming and beam steering techniques is provided in Fig. 1.3. All these technologies are introduced to compensate path losses in the mmWave spectrum but at the same time introduce new exposure scenarios for public, in which the electromagnetic field levels are increasingly complex to assess. Furthermore the exploitation of the mmWave spectrum completely changes the electromagnetic interaction also with human body, since due to the small depth of penetration, surface tissues such as skin and eyes are mainly involved [18]. This makes it necessary to define suitable methods and parameters to evaluate safety for human exposure.

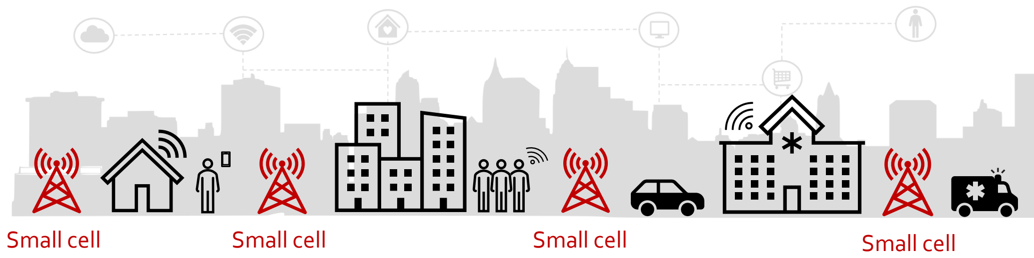

Figure 1.1: Small cell deployment in urban scenario.

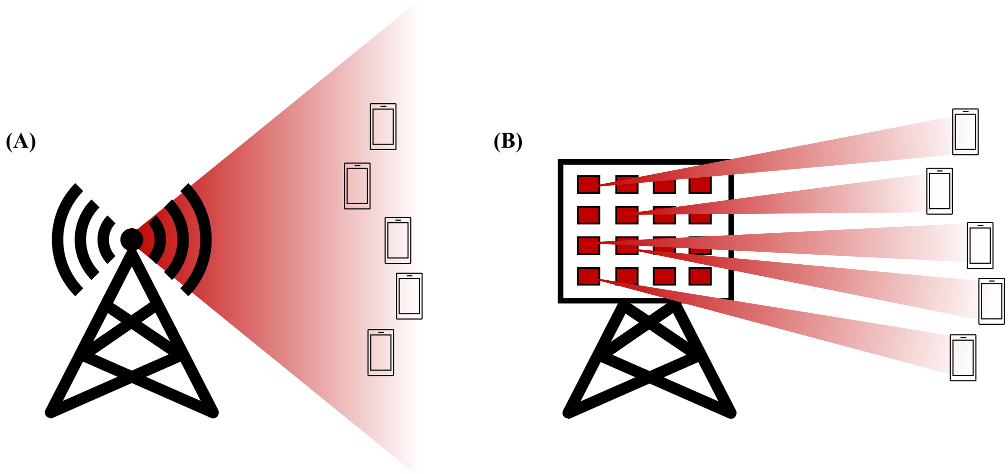

Figure 1.2: Working principle of conventional antenna (A) and massive MIMO antenna (B).

1.2 5G Bands Allocation in the Electromagnetic Spectrum

Three main frequency bands are identified for 5G applications: FR1 band (below 6 GHz), FR1 (C) (4 GHz - 8 GHz), FR2 band (above 24.25 GHz) and FR3 band (7 GHz –24 GHz) [19], [20], [21], [22], [23]. The spectrum allocation for each band is different according to the specific country. In many European countries, for example, frequencies in the FR1 range 700 MHz and 3.4 GHz - 3.8 GHz and in the FR2 range 24.5 GHz – 27.5 GHz are assigned for telecommunication services [24], [25], [26]. The FR3 band is recently proposed for its promising performances, but since now it is mostly subject of research studies and it is not employed by telecom operators [27]. All these frequency bands fall within the electromagnetic spectrum

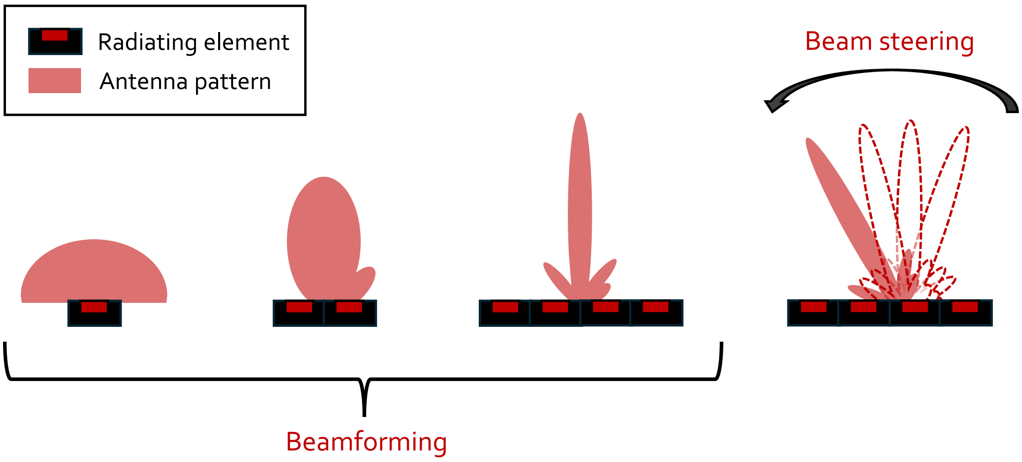

Figure 1.3: Schematical representation of beamforming and beamsteering techniques.

of non-ionizing radiation (NIR), which refers to electromagnetic radiation that does not have enough energy to remove electrons from atoms or molecules, through a process called "ionization" [18]. This characteristic distinguishes them from ionizing radiation, such as X-rays or gamma rays, which, on the other hand, have enough energy to induce ionization and, consequently, can potentially cause biological damage. Both frequency ranges are shown in the full electromagnetic spectrum reported in Fig. 1.4.

Generally, electromagnetic waves can be defined by one of the following physical parameters: frequency (f), wavelength (λ) and photon energy (E_p), in which the wavelength is inversely proportional to frequency and is defined as the distance between successive peaks of an electromagnetic wave, while the photon energy represents the energy associated to each photon of the electromagnetic wave and is inversely proportional to the wavelength [28]. The mathematical expressions of wavelength and photon energy are reported in eq. 1.1 and eq. 1.2, respectively:

$$\lambda = \frac{c}{f} \tag{1.1}$$

$$E_p = h_p f = \frac{h_p c}{\lambda} \tag{1.2}$$

with $c = 3 \cdot 10^8$ m/s speed of light and $h_p = 6.626 \cdot 10^{-34}\ J \cdot s$ Planck's constant. The electromagnetic spectrum is generally divided into different bands, from lower to higher frequency with the following denominations: radio waves and microwaves (from Hz-GHz to which corresponds a wavelength range from a few centimeters to many thousands of kilometers), infrared (IR) (around THz), visible light (hundreds of THz to which corresponds wavelength range that covers all colors from blue at 400 nm to red at 700 nm, with blue light having more energy than red light), ultraviolet (around PHz), X-rays (from tens to tens of thousands PHz), and gamma rays ($>$ EHz). In each of these bands, the electromagnetic waves have different characteristics, starting from the way in which they can be generated to the way in which they interact with matter. Indeed, as previously discussed, the wave energy increases until the spectrum of ionizing waves is reached and the energy required to induce ionization is exceeded.

In addition to this, the values of wavelength provide information about the dimensions of the objects with which the electromagnetic wave can interact. More in detail, when the dimension of the interacting object is comparable to the wavelength (typically $\lambda/2$), maximum coupling is established with intense scattering, absorption and resonance phenomena [29], [30]. This explains why when mmWaves are employed for telecommunications, the atmospheric absorption increases, since the wavelength is comparable to rain and fog droplets dimensions. Moreover, according to the specific spectrum range, electromagnetic fields can be employed in different practical applications and this strongly depends on the frequency-dependent effects that can be induced. Indeed, in the radio and microwave spectrum, main applications include heating of tissues for therapeutic purposes [31], [32], [33], [34] or agronomy-oriented treatments [35], [36], [37]. On the other hand, in the IR spectrum typical applications include thermal imaging [38], [39] or IR spectroscopy [40], while ultraviolet radiations are typically employed for sterilization and disinfection [41], [42].

Finally, in the radio frequency (RF) spectrum the most widespread implementation of electromagnetic fields is the telecommunications, and with the new introduction of 5G systems this is extended also up to the 30 GHz - 300 GHz spectrum, that is called mmWave spectrum due to the wavelengths involved (from 10 mm up to 1 mm) [18]. It can be seen from the iconographic representations in Fig. 1.4, that evident advances in the field of telecommunications have been obtained over the years by using increasingly higher frequency portions of the spectrum. Indeed, this lead to the analog-based communications of first generations (1G) systems, that employed frequencies of hundreds of MHz [43], [44], to the actual 5G advanced configurations [6].

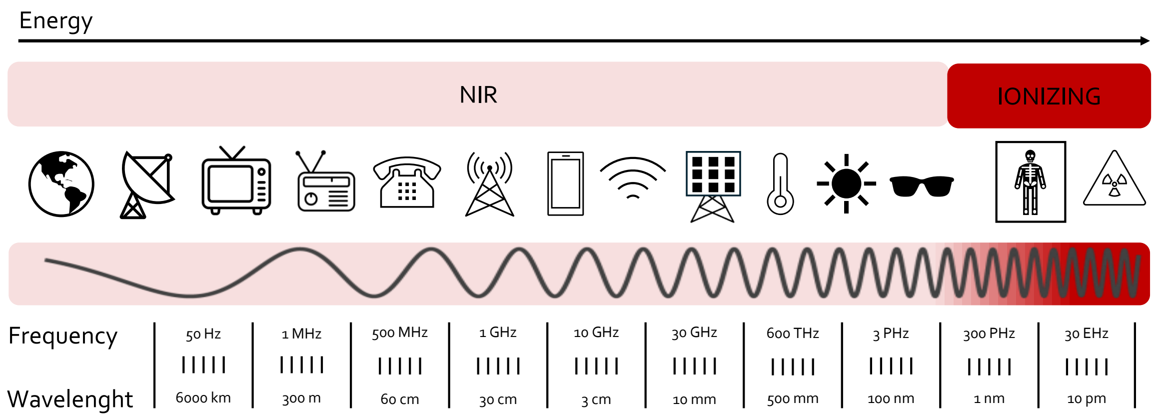

Figure 1.4: Electromagnetic spectrum.

1.3 Electromagnetic Fields Interaction with Human Body at 5G Frequencies

As described in previous section, frequencies employed for 5G communications fall within the RF spectrum, in which the only demonstrated effect of electromagnetic fields on human body is heating [45]. To discuss where this outcome came from, it is necessary to introduce some fundamental physical parameters. It is well known that the interaction between electromagnetic fields and materials can be described by means of Maxwell's equations [30], [34] and is strictly related to the constitutive parameters of the medium and the frequencies involved. More in detail, this interaction is related by fundamental physical parameters: the permittivity and permeability, which describe the behavior of a medium in the presence of an external electromagnetic field. In the frequency domain, the effective relative permittivity (ε_r^*), that is the complex permittivity expressed with respect to that of vacuum ($\varepsilon_0 = 8.854 \cdot 10^{-12} F/m$), is characterized by two terms: the real part (ε_r), that is related to the capacity of the medium to store electromagnetic energy and the imaginary part (ε_i), that describes the dissipative behavior of the medium. More in detail, its expression can be written in the following form:

$$\varepsilon_r^* = \varepsilon_r - i(\varepsilon_{rp}'' + \frac{\sigma_s}{\omega \varepsilon_0}) = \varepsilon_r - i\varepsilon_i \tag{1.3}$$

where ε_r represents the real part of the relative permittivity and the imaginary part is expressed as the sum of two different contributions: ε_{rp}'' that describes losses into the medium due to polarization mechanisms related to the presence of polar molecules and σ_s that is the static conductivity (S/m) related to the presence of free electric charges inside the material. Finally, $\omega = 2\pi f$ is the angular frequency. This expression of the permittivity clearly shows that, according to the frequency of the electromagnetic field, different effects can be induced into a loss medium. In particular, two limiting cases can be identified:

1. In the case of low RF frequencies ($\omega \to 0$), the contribution of σ_s is dominant.
2. In the case of high RF frequencies ($\omega >> 0$), the contribution of ε''_{rp} is prevalent.

This means, from a physical point of view, that according to the RF considered, heating effect can be generated into a loss medium (i.e. human tissues) due to the presence of the electromagnetic field, and it can be induced by two different mechanisms:

- Due to the movement of ionic charges inside the tissue (for lower frequencies in the RF spectrum). Indeed, due to the presence of the electromagnetic field, ionic charges inside the tissue start moving, continuously colliding with surrounding atoms and molecules. This ionic agitation induces a temperature increase inside the tissue due to the conversion of the kinetic energy generated by continuous collisions into thermal energy, with a physical mechanism known as Joule heating effect.
- Due to the oscillations of polar molecules into the medium (for higher frequencies in the RF spectrum) that try to align their direction with the one of the applied field. Indeed, due to oscillatory movements of electromagnetic fields, polar molecules oscillate, continuously colliding with each other, according to the dipolar or orientation polarization phenomenon. The high friction between molecules gives rise to energy dissipation into the medium due to dielectric losses, that is converted into a temperature increase.

Since 5G networks are intended to work at higher frequencies of the RF spectrum (from 700 MHz up to 300 GHz), their main effect on human body is the heating due to the dipolar polarization phenomenon. Indeed, human tissues are composed by an high percentage of water, that is a well known polar molecule, in a quantity that is typically around 70% of the total tissue composition [46]. In Fig. 1.5 a representation of dipolar polarization for water molecules is reported. As can be seen, water molecules are permanent dipoles since a partial negative ($\delta-$) charge is present in proximity of oxygen molecule (O), while a partial positive charge ($\delta+$) is present near hydrogen molecule (H). Due to the oscillations of the external electromagnetic fields, water molecules rotate continuously for aligning with the direction of the field.

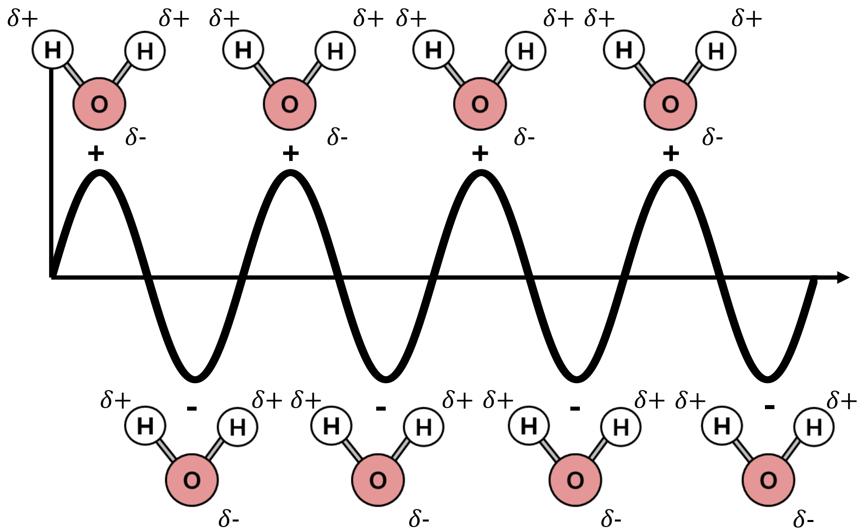

Figure 1.5: Dipolar or orientation polarization of water molecules subject to an oscillating electromagnetic field.

1.4 Dosimetry Assessment at 5G Frequency Bands according to ICNIRP Guidelines

To assess the effect of electromagnetic fields on human body at 5G frequencies, the most widely adopted reference guidelines are published by the International Commission on Non-Ionizing Radiation Protection (ICNIRP). The ICNIRP is an independent, non-governmental, international scientific organization, recognized by the World Health Organization (WHO), established with the aim to assess the health risks of exposure to NIR frequencies and to harmonize electromagnetic field exposure standards at an international level. This organization is responsible for publishing guidelines and recommendations for safe exposure levels in the whole NIR band, ranging from static fields to visible and ultraviolet radiation [47]. These recommendations represent a scientific guidance and, even if not legally binding, are adopted as a reference for national regulations worldwide. The human exposure is evaluated introducing different dosimetry parameters, based on the considered range of frequencies, that allow to quantify the effect of electromagnetic fields on the human body according to the physical mechanism underlying their interaction. Threshold values for the different parameters are estimated considering a certain reduction factor with respect to the operational adverse health effect threshold, that are the values for which a certain effect due to exposure to the electromagnetic field has been detected.

In addition to this, another reduction factor is applied, differently for the case of occupational and general public exposure. Indeed, the general public cannot be expected to be aware of exposure guidelines and thus to mitigate risk, an higher reduction factor is applied. Published guidelines are divided depending on the frequency spectrum and are periodically updated based on research studies. As a matter of fact, due to the large-scale deployment of 5G systems, guidelines for RF electromagnetic fields (ranging from 100 kHz to 300 GHz) have been updated in 2020 [45], to examine in depth the mmWave spectrum and its effects on the human body. More in detail, in this new version, a distinction is made between electromagnetic field interaction with human body below 6 GHz and above 6 GHz. In both cases, the only demonstrated potential adverse effect is heating, following discussions carried out in the previous section, but, due to the different frequencies involved, two dosimetry parameters are introduced. In the following, a detailed description of these parameters is provided.

1.4.1 Dosimetric Quantity for the Exposure Assessment in the FR1 Band

As previously discussed, 5G FR1 band involves frequencies below 6 GHz. According to ICNIRP guidelines the dosimetric quantity that describes the effect of electromagnetic fields on human body in this RF spectrum is the Specific Absorption Rate (SAR). This parameter was already present in the previous version of the guideline, but was intended up to 10 GHz [48]. With the introduction of the latest 2020 version, the local SAR has been replaced above 6 GHz by a new dosimetric quantity. In both cases, the SAR represents a quantitative measure of RF power absorbed in a living body [18]. It can be generally defined as the time derivative of the incremental energy (dW) absorbed by (dissipated in) an incremental mass (dm) contained in a volume element (dV) of given mass density (ρ) [49], with the following expression [50], [51]:

$$SAR[\frac{W}{kg}] = \frac{d}{dt}(\frac{dW}{dm}) = \frac{d}{dt}(\frac{dW}{\rho dV}) \tag{1.4}$$

Moreover, it can also be expressed as the dissipated power (P_{diss}) per unit mass (m) or as a function of the electric field distribution inside the tissue and its properties (mass density and conductivity (σ)), according to the following expressions [18], [52]:

$$SAR[\frac{W}{kg}] = \frac{P_{diss}}{m} = \frac{P_{diss}}{\rho dV} = \frac{\sigma|E|^2}{2\rho} = \frac{\sigma|E_{rms}|^2}{\rho} \tag{1.5}$$

where E and E_{rms} are the peak and root-mean-square value of the electric field, respectively [52]. It should be noted that σ, E, and ρ are all functions of the position within the tissue exposed. Another expression for the SAR can be obtained considering a homogeneous non-perfused material (t $\geq$ 0) [18] :

$$SAR[\frac{W}{kg}] = c_p\frac{\Delta T}{\Delta t} \tag{1.6}$$

with c_p specific heat of the tissue (J/kg/°C), ΔT temperature increase and Δt duration of exposure. According to ICNIRP guideline [45], SAR is specified over different masses to better match particular adverse health effects; SAR_{10g} represents the power absorbed (per kg) over a 10 g cubical mass, while the whole-body average SAR represents power absorbed (per kg) over the entire body. More in detail, a 10 g mass is used because, although there can initially be temperature heterogeneity within that mass, heat diffusion rapidly distributes the thermal energy to a much larger volume that is well-represented by a 10 g cubic mass. In Table 1.1, SAR thresholds for human exposure are reported both for the whole body and local SAR in the case of occupational and general public. It should noted that the whole-body SAR is still valid up to 300 GHz.

Exposure Scenario	**Whole-Body SAR [W/kg]**	**Local Head/Torso SAR [W/kg]**	**Local Limb SAR [W/kg]**
Occupational	0.4	10	20
General Public	0.08	2	4

Table 1.1: SAR limits below 6 GHz according to ICNIRP guidelines. Whole-body SAR is to be averaged over 30 min while local SAR exposures are to be averaged over 6 min.

It can be seen that different SAR values are reported, since they derive from different adverse health effect thresholds resulting from experiments. Moreover, it should be noted that the whole body SAR is always averaged over the entire body mass and 30 min interval, while the local SAR over a 10 g cubic mass and 6 min interval. Indeed, a whole body average SAR of 4 W/kg is taken as the exposure level corresponding to the operational adverse health effect threshold for an increase in body core temperature of 1°C. A reduction factor of 10 is applied for occupational exposure to account for scientific uncertainty, differences in thermal physiology across individuals and variability in environmental conditions and physical activity levels [45]. Thus, the basic restriction for occupational exposure becomes a whole body average SAR of 0.4 W/kg, while a reduction factor of 50 is applied to the general public, obtaining a SAR restriction for the general public of 0.08 W/kg.

As regards the local SAR, head, torso and limb are considered. For head and torso guidelines take a SAR of 20 W/kg, as the local exposure level corresponding to the operational adverse health effect threshold for the head and torso. A reduction factor of 2 is applied to this value for occupational exposure, thus, obtaining a restriction of SAR_{10g} equal to 10 W/kg. On the other hand, a reduction factor of 10 is applied for the general public, obtaining a SAR_{10g} of 2 W/kg. For limb, the guidelines take a SAR of 40 W/kg as the local exposure level corresponding to the operational adverse health effect threshold. The same reduction factors of head and torso are applied, obtaining a SAR_{10g} for occupational exposure of 20 W/kg, while 4 W/kg for general public. Finally, it should be noted that when the long axis of the human body is parallel to the electric field vector, and under plane-wave exposure conditions (i.e., far-field exposure), whole-body SAR reaches maximal values [48].

1.4.2 Dosimetric Quantity for the Exposure Assessment in the FR2 (mmWave) and FR3 Bands

As discussed, the exploitation of the mmWave spectrum, has led to an updated version of ICNIRP guidelines in the RF frequencies, obtaining the actual latest version of the year 2020 [45]. More in detail, with respect to the previous version, the main change is the introduction of a new dosimetric quantity above 6 GHz, replacing the local SAR, that is the Absorbed Power Density (APD) or S_{ab}. It is specified into the guideline that there is uncertainty with regard to the precise frequency for the change from SAR to APD, and 6 GHz is chosen because at that frequency, most of the absorbed power is within the cutaneous tissue and, thus, within the upper half of a 10 g SAR cubic volume (that can be represented by the 2.15 cm x 2.15 cm surface of the cube). To understand why the APD is introduced, it is necessary to define an important electromagnetic parameter, known as the penetration depth (δ). Specifically, when RF fields interact with the human body, that is from an electromagnetic point of view a loss medium, a portion of the electromagnetic wave penetrates into the tissues and exponentially decays from the surface to deeper regions. This phenomenon is characterized according to the penetration depth, that can be expressed as follows [53]:

$$\delta = \frac{1}{\omega\sqrt{\frac{\mu_0\mu_r^*\,\varepsilon_0\varepsilon_r^*}{2}\left(\sqrt{1+\left(\frac{\sigma}{\omega\varepsilon_0\varepsilon_r^*}\right)^2}-1\right)}} \tag{1.7}$$

with μ_0 magnetic permeability of vacuum equal to $\mu_0 = 4\pi10^{-7}F/m$, μ_r^* relative magnetic permeability that is equal to 1 for human tissues, and σ tissue conductivity. This expression can be simplified for high loss materials ($\sigma >> \omega\varepsilon_r^*$), obtaining the formula (1.8) in which the inverse proportionality between frequency and penetration depth is very clear:

$$\delta = \sqrt{\frac{2}{\omega\mu_0\mu_r^*\sigma}} \tag{1.8}$$

This parameter is also defined as the distance from the surface where 86% of the RF power is absorbed [45]. As can be seen, it depends on the electromagnetic characteristics of the medium and is inversely proportional to the frequency. In fact, if human skin is considered, the corresponding penetration depth at 6 GHz is 8.1 mm, while at 60 GHz it is 0.49 mm [45], meaning that the higher the frequency, the less penetration of the electromagnetic field is obtained into the human body and the power absorption is confined within very superficial regions, such as the skin. For this reason, APD is introduced as a new dosimetric quantity. Indeed, differently from the SAR that evaluates the absorbed power in a volume, the APD represents the power absorbed per surface area unit [W/m^2]. Its expression can be derived using the Poynting vector definition as [54]:

$$APD[\frac{W}{m^2}] = \iint_A Re[\mathbf{E}\times\mathbf{H^*}]\frac{d\mathbf{s}}{A} \tag{1.9}$$

Where **E** and **H** are the electric and magnetic field vectors, respectively, calculated inside the human body, while d**s** is the integral variable vector with its direction normal to the integral area A on the body surface. Another expression can be found if the incident power density (S_{inc}) is considered:

$$APD[\frac{W}{m^2}] = S_{inc}(1 - |r|^2) \tag{1.10}$$

in which r is the reflection coefficient. It should be noted that in the case of far-field or transverse electromagnetic (TEM) plane wave, the expression of the incident power density simply becomes:

$$S_{inc} = \frac{|E_{0rms}|^2}{Z_0} = Z_0|H_{0rms}|^2 \tag{1.11}$$

with Z_0 the characteristic impedance of free space, i.e., 377 Ω. According to ICNIRP guidelines, restrictions values for APD are reported in Table 1.2.

Exposure Scenario	**Local APD [W/m^2]**
Occupational	100
General Public	20

Table 1.2: APD limits from 6 GHz to 300 GHz according to ICNIRP guidelines. APD exposures are to be averaged over 6 min.

The guidelines take an absorbed power density of 200 W/m^2, averaged over 6 min and a square 4 cm^2 surface area of the body, as the local exposure corresponding to the operational adverse health effect threshold for head, torso, and limb regions. As in the previous case, a reduction factor of 2 is applied for occupational exposure and of 10 for the general public. Values are to be averaged over 6 min and a square 4 cm^2 surface area of the body. Furthermore, to account for focal beam exposure from >30 to 300 GHz, absorbed power density averaged over a square 1 cm^2 surface area of the body must not exceed 2 times that of the 4 cm^2 basic restrictions for workers or the general public.

1.5 Reference Levels for Exposure Assessment at 5G Frequencies

The exposure restrictions presented in previous sections are also named "basic restrictions" according to the ICNIRP guidelines. As discussed, they relate the external RF source directly with the power absorbed inside the human body, providing a quantification of the electromagnetic field exposure effects. However, both SAR and APD require the knowledge of physical parameters inside the body to be assessed. Indeed, SAR is related to the electric field distribution or to the temperature

elevation inside the exposed tissue, as well as the APD according to its definition should be retrieved at the human skin surface. This definitely means that dosimetric parameters, in the way they are defined, are not easily measurable *in vivo* for ethical issues. For this reason, the ICNIRP introduces different quantities that are more easy to evaluate, named "reference levels" [45]. These quantities are derived from a combination of computational and measurement studies to provide a more practical way to assess compliance with guidelines, ensuring the same degree of protection as the basic restrictions. In this way, the exposure is taken to be compliant with the guidelines if it is shown to be below either the relevant basic restrictions or the relevant reference levels [45]. Following a conservative approach, reference levels have been established so that, even under worst-case exposure scenarios, the resulting exposure will remain comparable to that defined by the basic restrictions. In this way compliance with the reference levels leads to exposure levels that are significantly below those of the corresponding basic restrictions.
The reference level quantities relevant for 5G exposure assessment are incident electric field strength (E_{inc}) and the incident incident power density (S_{inc}). It should be noted that another quantity, the plane wave equivalent incident power density (S_{eq}), can be considered above 2 GHz, with the expression reported in eq.(1.11). Indeed, at these frequencies, RF fields generally follow the characteristics of plane wave or far-field exposure conditions and the incident power density or the equivalent incident power density can be used as reference levels in this frequency region. Moreover, the reactive near-field exists very close to a RF source in this frequency region. Indeed, the typical boundary of the reactive near-field and the radiative nearfield is defined as $\lambda/(2\pi)$ (e.g., 8 mm at 6 GHz) [45].
Finally, with the latest version of ICNIRP guidelines, the whole-body reference levels have been extended from below 6 GHz, up to 300 GHz. The exposure restrictions are reported in Table 1.3, considering the range between 2 GHz and 300 GHz. As can be seen, in the Table "NA" signifies "not applicable", meaning that the corresponding parameter does not need to be taken into account when determining compliance. However, since with the assumption of far field exposure the incident power density and the electric field can be easily related, it is possible to define as limit for the occupational 137 V/m and for the general public 61 V/m, but only if the far field assumption is valid.

As discussed, ICNIRP limits are used as a reference in most countries worldwide. There are some exceptions, such as the United States that adopt their own independent exposure standards. Indeed, in this case, the reference authority that

Exposure Scenario	**Incident E-field strength; E_{inc} [V/m]**	**Incident power density; S_{inc} [W/m^2]**
Occupational	NA	50
General Public	NA	10

Table 1.3: Reference levels for exposure according to ICNIRP guidelines, averaged over 30 min and the whole body, in the frequency range > 2-300 GHz (unperturbed rms values).

is the Federal Communications Commission (FCC) [18], a government agency responsible for regulating telecommunications and establishing safety limits for RF emissions, relies on other standards such as the IEEE Standard C95.1 [50]. In most EU countries, even if the limits provided into the guidelines are already conservative, government institutions implement stricter levels of safety, further reducing the threshold values compared to the reference levels recommended by the standards. As a case in point, in Italy the exposure limits in terms of the incident electric field strength were reduced by a factor of 10 up to 300 GHz for the general public with respect to ICNIRP guidelines since 2023. A new law no. 214 of 30 December 2023, partially modified exposure restrictions, increasing the reference levels up to 15 V/m to meet the needs of network operators for providing a high-quality service [55]. This is also in line with what recommended into ICNIRP guideline, in which it is specified that when "reference level quantities are associated with greater uncertainty, reference levels must be applied more conservatively" [45]. Additionally, ICNIRP-based limits are also time-averaged, and some Member States apply more restrictive limits specifically for long-term or continuous exposure in residential and sensitive environments.

1.6 Challenges in the Exposure Assessment at 5G Frequencies

Based on the above considerations, it turns out that the assessment of electromagnetic field levels generated by new 5G systems can be very challenging, since it may require to evaluate the human exposure at two different levels:

- population level: assessment of electromagnetic fields in the environment to ensure that the compliance with reference levels is respected;
- skin level: quantification of the electromagnetic field effects close the human

body, considering the absorbed power into the tissues and the compliance with basic restrictions.

As regarding the first point, different technical standards have been introduced, both at international and European level, with the aim to provide procedures for accurately measuring and assessing exposure to 5G RF electromagnetic fields. The most widely used is the IEC standard 62232, which provides methods for the determination of RF field strength, power density and specific absorption rate (SAR) near BS in the range 110 MHz to 300 GHz [56], [57]. More in detail, the standard defines methods to evaluate RF electric field strength [V/m] both *in situ* and in laboratories, and recognizes numerical simulations as a valid method for RF exposure evaluation, especially when direct measurements are insufficient or need to be supported by prediction analysis. Among numerical methods, ray-based methods are considered as a worthwhile technique for far field electromagnetic evaluation in real propagation scenarios and also for simulations in large scale [58],[59]. However, due to the base advanced and adaptive techniques employed by 5G BS, both simulations and measurements of their behavior are not straightforward [60]. Moreover, several ray-based algorithms are currently available and this may lead to different predictions of electric field levels due to the different algorithms adopted [61].
On the other hand, to assess the effect of electromagnetic field levels close to the human body, without involving human or animal subjects, equivalent phantoms mimicking tissues properties represent a very efficient and promising solution [62]. Nevertheless, while up to 10 GHz standardized procedures for the evaluation of dosimetric quantities have been introduced and widely validated [63], [64], [65] also through the employment of human phantoms [66], [67], this is not true for frequencies above 10 GHz. Indeed, due to the recently introduction of the APD as dosimetric quantity at mmWaves, there is still a lack of methodologies and studies. In addition to this, it should be noted that for a reliable exposure assessment, human phantoms should be carefully optimized both from the electromagnetic and thermal point of view. This aspect increases the need of trustworthy optimization algorithms for an accurate phantom realization, without waste of materials.

1.7 Research Question

The final aim of this thesis is to assess the electromagnetic field levels generated by new 5G systems at both population and skin levels, providing reliable methodologies for human exposure assessment. Indeed, thesis main objectives are:

- the definition of harmonized and innovative frameworks for human exposure assessment at population and skin level up to the mmWave spectrum;
- provide reliable tools for the safety-critical design of 5G networks and optimized dosimetry experiments up to the mmWave spectrum;
- investigate and provide information about existing electromagnetic field levels in the environment up to the mmWave spectrum with a fair degree of reliability;
- the design and realization of new innovative phantoms for the assessment of APD and testing of wireless devices with advanced techniques.

To these purposes, a comprehensive analysis that involves analytical, numerical and experimental approaches is performed. More in detail, to assess population exposure, both computational and experimental methods are employed, relying on ray-based algorithms and measurement campaigns carried out in both FR1 and FR2 bands. To enhance results trustworthiness, this activity involves antenna operators, which provide detailed information on the BS characteristics, and benchmarking with external research institutions expert in the field. The comprehensive undertaken study leads to the definition of harmonized and standardized frameworks to assess population exposure in several real-life scenarios, providing essential information on current exposure levels and what to expect from the deployment of new 5G technologies. Additionally, the same analysis supports the optimized design of 5G networks to ensure an efficient radio coverage. However, dosimetry at the skin level is investigated above 10 GHz by means of analytical, numerical, and experimental approaches. Indeed, analytical models to optimize the design phantoms at mmWaves, both from the electromagnetic and thermal point of view, are developed and numerically validated, introducing fundamental tools for dosimetry assessment and resulting in the definition of a multi-physics optimization protocol. The effectiveness of the proposed optimization approach is proven numerically and experimentally, leading to the realization of a new innovative phantom to test the performance and safety of wireless devices in the mmWave spectrum. Moreover, a thorough analysis on phantom design is carried out, providing key information on the electromagnetic characteristics of materials employed for phantom realization.

1.8 Thesis Overview

In this Chapter key innovations related to 5G technologies and their implications on the exposure assessment are discussed, giving an overview of the main challenges they introduced. The next Chapters are organized as follows:
Chapter 2: an in-depth analysis of the state of the art on ray-based algorithms and phantoms mimicking human tissues is performed, pointing out the main gaps currently present in the literature. Moreover, the original contributions of this research are presented.
Chapter 3: the ray-based algorithm employed in this thesis is presented and carefully described from the physical point of view. Afterwards, its application for the population exposure assessment in the FR1 and FR2 band is presented in different real case scenarios.
Chapter 4: the computational analyses carried out for the exposure assessment are extensively numerically and experimentally verified. In addition to this, a workflow for ray-based tools assessment is presented.
Chapter 5: electromagnetic and thermal modeling of solid reflectivity-based phantoms at mmWaves is presented. Therefore, analytical models are developed and numerically validated in different configurations.
Chapter 6: a multi-physics optimization approach is developed and implemented for the broadband design of reflectivity-based skin phantom at mmWaves. Additionally, the design, realization and characterization of a new solid phantom for Over-The-Air (OTA) testing is presented.

Chapter 2

State of the Art

In this Chapter a literature review is presented to introduce the state of the art on ray-based algorithms employed in human exposure assessment, together with solid phantoms realized to retrieve the APD. Moreover, the main methods actually proposed in the literature to evaluate APD are discussed. Research gaps are highlighted with the aim to clarify the overall thesis original contributions.

2.1 Ray-Based Algorithms for the Assessment of Exposure Reference Levels at 5G Frequencies

The assessment of electromagnetic field levels in the environment generated by new 5G networks can be very challenging. Indeed, differently from previous generations, 5G systems can be characterized by two different electric field levels [60]:

- "always on" electric field level due to broadcast beams that are used to send control signals for User Equipment (UE) access;
- traffic beams electric field level existing "in the air" only in the presence of a UE.

The electric field levels, due to the broadcast beams, can be measured by numerous portable automatic measurement systems offered on the market (i.e. spectrum analyzers, 5G phone with proper software and so on). They are relatively easy to measure, but their knowledge is not sufficient for the complete assessment of human exposure. Indeed, traffic beams may have a significant impact on the total electromagnetic field levels when multiple users are connected. However, measure electric field levels generated by traffic beams is not straightforward for 5G technologies due to the time and space variance of these signals [68]. To this end, different extrapolation techniques have been developed [56], trying to estimate the maximum level of electromagnetic field that a BS can radiate, but due to the unpredictability of the transmitted power, an accurate exposure assessment may become quite complex [68]. In this context, ray-based algorithms are increasingly employed in many propagation studies on 5G systems, both in the FR1 band and in the FR2 band, and overall results demonstrate that the method is a valuable support for the electromagnetic field assessment in 5G scenarios [58], [69], [70], [71], [71], [59], [72], [73], [74], [75], [76], [77]. This is explainable by several reasons [78]:

- high accuracy in simulations for the high frequencies involved in 5G networks. Indeed, due to the small wavelengths, deterministic models as ray tracing can accurately follow multi-paths and detailed characteristics of environments;
- accurate modeling of transmission and receiver angle, necessary for massive MIMO and beamforming techniques, together with future implementations in 5G environments such Reconfigurable Intelligent Surfaces [79];
- the ability to plan radio coverage in large and complex environments, considering different antenna or environmental parameters, and to implement calibration for accurate description of buildings and other scenario objects;
- the possibility to provide an accurate dataset for the training of neural networks models, useful for the establishment of future Digital Twins [80], [81].

Ray-based propagation simulations can be carried out by means of different algorithms. More in detail, following the distinction made in [61], [82], ray-based models can be differentiated into ray tracing approach and ray launching approach. Below, a brief description of these methods is provided.

Ray Launching: is a technique for simulating radio wave propagation. In this approach, the transmitter launches rays separated by a set angular distance across both azimuth and elevation to cover the simulation environment. Each ray travels through the scenario and interacts with different objects, giving rise to reflection and diffraction phenomena. According to the specific implementation, after a certain number of interactions, the algorithm determines whether a ray reaches the target receiver, and the rays that intersect the receiver are used to calculate the final electromagnetic field distribution. A more detailed description of this technique will be provided in the following chapters.

Ray Tracing: is a propagation modeling technique that simulates electromagnetic wave behavior by computing all significant ray paths connecting the transmitter to each specific receiver point. For every receiver location, ray tracing systematically determines a comprehensive set of rays, ensuring that all relevant propagation mechanisms, including reflections, diffraction, and scattering, are taken into account. Differently from the ray launching, all the possible propagation paths that connect the receiver and the transmitter are determined.

Some of the most widespread approaches based on these two methods are briefly reported below [83], [84], [85], [86], [82], [61].

Image Method: is a point-to-point propagation simulation method based on the above-discussed ray tracing approach. The algorithm is based on the following working principle: given the positions of the transmitter, receiver, and reflecting surfaces, it determines the exact reflection point on each surface that satisfies the law of reflection by transforming the reflected path into an equivalent straight line. The intersection of this line with the surface defines the reflection point. The same process can be extended for multiple reflections, and diffraction can be computed either by the Geometry Theory of Diffraction or the Uniform Theory of Diffraction (GTD/UTD) [61], [87].

Shooting and Bouncing Rays (SBR): is a realization of the ray launching approach. Indeed, a set of rays is launched from the transmitter with a given angular separation. The launched rays are propagated in the environment up to a maximum number of interactions with surfaces and are considered to reach the receiver if they meet a specific reception condition [82]. For each ray multiple bounces are considered.

Overall, following the classification for path-loss prediction models proposed in [83], ray-based algorithms can also be defined, together with the finite-difference time-domain (FDTD) method, as site-specific or deterministic models. In addition to this, path-loss can be computed by means of semi empirical models, a set of equations derived from extensive field measurements [83]. An example is represented by the Walfisch-Ikegami model, a model that considers total attenuation

as a combination of different basic components, both in Line Of Sight (LOS) and Non-LOS (N-LOS) [88]. Finally, theoretical models can be employed, physically derived assuming some ideal conditions. Among these, there are the UTD, GTD and Knife-Edge diffraction theories [89].
Ray-based techniques are widely used for channel modeling of 5G systems to study network performances [69], [70], [90], [91], but their use is increasingly spreading for human exposure assessment. A literature review is carried out by means of the EMF-portal that summarizes systematically scientific research data on the effects of electromagnetic fields [92]. More in detail, using together the keywords "ray tracing" "exposure" "5G" and "ray launching" "exposure and "5G" 24 works are found, starting from the year 2019. Extending the research using only the keywords "exposure" and "5G", 803 studies are present, so among them only the ones referred to ray-based algorithms are considered from the year 2019, keeping in mind that the 3rd Generation Partnership Project (3GPP) completed Release 15 in June 2018, marking the birth of 5G [93]. Therefore, the literature review of ray-based simulation study on human exposure assessment at 5G frequencies is reported in Table 2.1. More in detail, studies are classified considering frequency band, numerical validation with *on-site* measurements and comparison with other ray-based tools. As can be seen, most of the studies are related to the FR1 band, since it has been the first to be introduced and is currently widespread throughout the territory. On the other hand, very few works are presented in the FR2 band, also due to the lack of available operative antennas. Moreover, only two papers analyze the comparison between results of different ray tracing tools, and both of them compare two ray-based algorithms.

2.2 Tissue-mimicking Phantoms for Human Exposure Assessment at 5G Frequencies

As discussed, in the reactive near-field region, reference levels cannot be used to determine human exposure, and in many scenarios (i.e. simply a person who uses the phone close to his head) basic restrictions need to be considered. Moreover, moving to higher frequencies, especially to the mmWave spectrum, increases the potential to develop wearable antennas, given the short wavelengths [120], [121], which are intended to come into direct contact with the human body. Therefore, to assess compliance with new exposure limits, but also wireless device performances

Reference	Frequency band	Measurements (y/n)	Other tools (y/n)
[76]	FR1	y	y (2)
[94]	FR1	y	n
[95]	FR1	n	n
[96]	FR1	n	n
[97]	FR2	n	n
[98]	FR1	y	n
[98]	FR1	n	n
[99]	FR1	n	n
[100]	FR1 and FR2	n	n
[101]	FR2	n	n
[102]	FR1	n	n
[103]	FR1	y	y (2)
[72]	FR1	n	n
[104]	FR1	n	n
[105]	FR1	n	n
[106]	FR1	n	n
[107]	FR1 and FR2	y	n
[108]	FR2	y	n
[109]	FR1	y	n
[110]	FR1	n	n
[111]	FR1 and FR2	y	n
[112]	FR1	y	n
[113]	FR1	y	n
[114]	FR1	y	n
[115]	FR2	y	n
[116]	FR1	n	n
[117]	FR1	n	n
[118]	FR1 and FR2	n	n
[119]	FR1	n	n

Table 2.1: Ray-based simulation studies on human exposure assessment at 5G frequencies.

equivalent tissue-mimicking phantoms represent the most widespread solution [62]. Overall, phantoms are classified in three main categories, considering the degree of solidity, namely, liquid, semisolid, and solid phantoms. Moreover, due to the frequency-dependence of tissue properties, they are also divided into narrow band and broadband phantoms, depending on the target frequency range. Indeed, narrow band solutions target only a small frequency band of interest, while broadband phantoms aim to mimic tissue properties in a wider range of frequencies [122].

2.2.1 Liquid and Semi-Solid Phantoms

Liquid phantoms represent the most easy and less expensive solution. They are usually prepared as a mixture of different ingredients that in appropriate concentrations help to achieve the desired dielectric properties of the tissue. Most of the proposed liquid phantoms are realized as a mix of water together with sugar and sodium chloride (NaCl). The water is chosen as the base ingredient since, as previously discussed, tissues are water-based themselves, while sugar is known to lower permittivity of the water, and this effect becomes more pronounced as its concentration increases [123], [124]. Differently, NaCl has the function to increase the conductivity of the solution when mixed with water [125]. These two components are the most widely used due to their low toxicity and easy accessibility. In addition to this, Triton X (TX)-100 and diacetin are also proposed to lower the permittivity of the solution [126], [127]. Liquid phantoms are suitable to perform measurements inside the phantom, as any probe can move freely, and for this reason are widely employed for measurements of implantable antennas/sensors and SAR assessment of body-area devices [126].

On the other hand, semisolid phantoms, also named gel phantoms, while more viscous than liquid phantoms, are less rigid than solid phantoms and represent an intermediate solution between these two. As for liquids, they are realized by mixing in appropriate proportions different ingredients, tuning their concentrations until the target tissue properties are achieved. In addition to this, another step is necessary to thicken the solution. Therefore, a thickening agent (agar, synthetic polymer, gelatin, or thickening additive) should be added to the liquid mixture, altering its final density. The mixture is then transferred into a mold with the desired geometric characteristics that can be either anatomical or conventional shapes. Typically, agar-based phantoms are the most widely used because of the physical and mechanical properties of this agent that are similar to those of human tissue. These phantoms are usually composed by edible materials, such as deionized water, polyethylene powder (PEP), sodium chloride mixed with agar. Their most widespread applications include hyperthermia [128], [129], [130] or SAR assessment [131], [132], [67], [133]. Thanks to the semi-solid structure, these phantoms can also emulate compound tissue, such as skin, fat, gland, and tumor tissue together [134].

Both liquid and semi-solid phantoms are widely established in literature for SAR measurements up to 6 GHz [62], [135], and very recently are introduced also for the APD assessment. Indeed, in [136], [137] a composite phantom emulating skin reflection coefficient in the frequency range from 24 - 30 GHz is developed. Specifically, the phantom is composed by a skin tissue simulating liquid contained above a shell. Additionally, in [138] a liquid skin phantom is used for APD assessment in the range 10 - 60 GHz and in [139] an agar-based phantom is proposed to mimic skin properties at mmWaves (28 GHz) and to quantify the impact of human body on the antenna perfomances.

2.2.2 Solid Phantoms

Differently from liquid and semi-solid phantoms, solid phantoms are characterized by a longer stability, since they overcome main limitations such as dehydration and deterioration due to invasion of bacteria or mold [140], [62]. As in the previous cases, they are designed as a mixture of different ingredients to achieve the desired dielectric properties. However, they are not water-based, thus advanced and specialized materials are employed and the realization process is much more challenging, generally requiring the doping of a lower-permittivity base (i.e., plastic or silicone) with conductive and high permittivity additives during the curing process [62]. Some solutions are proposed in literature, based on the use of different materials.
In [140], [141], [142] a mixture of ceramic and graphite powder bonded with a resin is employed for the realization of a phantom mimicking brand and muscle tissue at 900 MHz. More in detail, ceramic powder is chosen to control permittivity, while graphite powder is used to increase phantom conductivity. The phantom is designed for SAR assessment by means of thermographic techniques with the aim to evaluate the safety of devices operating in the ultra-high field band, such as portable radios [140]. Additionally, in [143], a flat solid phantom composed by ceramic powder, graphite powder, and bonding resin is proposed. More in detail, the phantom is realized to mimic head properties at 900 and 1950 MHz for SAR assessment. To overcome the complexity in the realization of ceramic-based phantoms, new solutions are proposed to develop solid conducting plastic phantoms, typically based on titanium dioxide and carbon black, mixed into a plastic, as the plastic cures [62]. Indeed, titatium dioxide is used to control the permittivity while carbon black to increase the conductivity. A phantom mimicking human muscle properties, based on this mixture, is proposed in [144], covering a frequency range between 300 MHz to 900 MHz and intended to be used in any setting over the microwave spectrum

requiring a stable, solid, high-loss material that simulates biological tissues. A similar composition is proposed in [145], in which a multi-layer phantom is designed to match the properties of fat and gray matter tissues from 1 MHz to 10 GHz. Another possible solution is represented by phantoms composed of silicone rubber and various forms of carbon. This combination allows to match both high and low-permittivity tissues across a wide frequency band [62]. Indeed, varying the type of carbon nanotubes in silicone base, in [146] both fat and muscle tissue phantoms are obtained at 430 MHz and 2.45 GHz and employed for SAR assessment using a thermograph camera. Moreover, in this study it is specified that the proposed type of phantom can be used to simulate any arbitrary tissue or group of tissues by selecting the proper weight ratios of the carbon fibers.

On the other hand, in [147] a muscle phantom in 1 GHz - 6 GHz range composed by carbon nanotubes and silicone rubber is proposed with the aim to perform experimental SAR assessment. A similar combination is used in [148] in which a hand phantom based on carbon-loaded silicones is developed in the frequency range 600-6000 MHz to be involved in SAR assessment. A phantom with the same characteristics is proposed in [100] to mimic human head in the context of 4G long term evolution bands for smart glasses applications. Two ranges of frequency are targeted (824–960 MHz and 1710–2690 MHz) for SAR evaluation. Overall, silicone-based phantoms are also sold by the Switzerland-based company Schmid and Partner Engineering AG (SPEAG) [149] for many different applications from low frequencies (10 MHz) up to higher frequencies (100 GHz). Additionally, in [150], a phantom mimicking human skin proprieties at 60 GHz band coefficient is presented. The phantom is composed of carbon nanotubes, silicone rubber, and carbon black and is used to assess skin temperature rise through thermography. All the presented phantoms are designed to emulate human tissue electromagnetic properties.

However, another approach is presented in [151], in which a breast phantom mimicking the reflection coefficient of the skin is realized to test and validate microwave breast imaging prototypes. The phantom is developed in a frequency range 1 GHz - 10 GHz and is based on silicone-carbon combination. Moreover, in [152] a solid phantom reproducing skin reflection coefficient at 28 GHz is proposed. The phantom is realized using polyphenylene-ether (PPE), typically used for antenna substrates, to be used for APD assessment. In addition to this, recently, reflectivity-based phantoms are introduced also for the exposure assessment at mmWaves. A solution based on a mix of metallized polydimethylsiloxane (PDMS) filled with carbon black powder is firstly proposed in [153] and then in other works [154], [155], [156],

[157], [158], [159], [38]. The phantom is designed, differently from previous solutions, to emulate not the same properties of human tissue, but the same reflection coefficient at the air/phantom interface as at the air/skin interface properties in the 58 - 63 GHz frequency range to assess the APD. The realization, implementation, and advantages of this phantom will be discussed further below. In Table 2.2 a review of solid phantoms in the frequency range 0-100 GHz proposed in literature are reported, specifying the frequency range, the target tissue parameter that can be either the complex permittivity (ε) or the amplitude of reflection coefficient (r), and its application in terms of dosimetry. As can be seen, most of them are realized at low frequencies for SAR assessment. For some of them in which Not Applicable (NA) is indicated, the specific application for the phantom is not provided in the study. On the other hand, where ΔT is reported, this means that the phantom is tested to assess the temperature increase, without specify the corresponding dosimetric parameter.

Reference	**Frequency range**	**Target**	**Dosimetry**
[140], [141], [142]	900 MHz	Muscle ε	SAR
[143]	900 and 1950 MHz	Head ε	SAR
[144]	300–900 MHz	Muscle ε	NA
[145]	1 MHz–10 GHz	Fat and Gray Matter ε	NA
[146]	430 MHz and 2.45 GHz	Fat and Muscle ε	SAR
[147]	1–6 GHz	Muscle ε	SAR
[148]	600 MHz–6 GHz	Hand ε	SAR
[100]	824–960 MHz and 1710–2690 MHz	Head ε	SAR
[150]	60 GHz	Skin ε	ΔT
[151]	1–10 GHz	Skin r	NA
[152]	28 GHz	Skin r	APD
[38], [153], [154], [155], [156], [157], [158], [159]	53–63 GHz	Skin r	APD

Table 2.2: Solid phantoms proposed in literature around 5G frequency bands.

2.2.3 Solid Reflectivity-Based Phantoms for APD Assessment at mmWaves through IR Techniques

As discussed, SAR estimation using phantom mimicking human tissues is a widely assessed method, supported also by numerous standardized procedures to perform accurate measurements [63], [64]. Furthermore, a large number of studies are presented in literature, demonstrating that either liquid, semi-solid and solid phantoms allow to accurately assess human exposure below 6 GHz [62], [135]. Overall, two methods can be employed to measure the SAR by means of phantoms: the probe and thermography methods. The probe method consists in the electric field measurement directly inside the phantom to derive the SAR. For this reason, this technique is limited only to liquid phantoms and sometimes semi-solid phantoms, since it is necessary to move the probe to obtain the internal field distribution. On the other hand, thermography or IR method can be used with solid and semisolid phantoms. Following this approach, an electromagnetic source is used to illuminate the phantom, and the induced temperature rise is measured to calculate SAR [66]. Differently, for the APD assessment, a standard for the experimental evaluation is introduced in [65] for frequencies in the range 6 - 10 GHz, in which it is still possible to derive the APD from SAR measurement systems specified in [64]. More in detail, it is possible by applying a simple conversion factor. However, for frequencies above 10 GHz, there are no standardized dosimetric testing systems available for APD assessment [137]. Therefore, following SAR methods, some attempts have been undertaken to scale the probe in-phantom measurement method to frequencies above 10 GHz, using liquid phantoms [136], [137], [138], [160] . However, they faced physical limitations due to prohibitively high losses in biological tissues and the consequent strong spatial APD gradient in measurements. Indeed, several aspects should be considered when employing this technique [137]:

- the probe used to determine the electric field distribution needs to measure as close as possible to the phantom surface (< 1 mm);
- the frequency range has to extend from 10 GHz to 30 GHz with a bandwidth of $>$ 800 MHz to capture all 5G signals;
- the probe should be able to operate calibrated traceable in the phantom liquid medium and not disturb the field distribution;

- isotropic error should be less than 1 dB and linearity error smaller than 0.4 dB over the dynamic range from 1% to 10 times the APD general public limit.

Thus, due to the aforementioned requirements, the probe design options are limited. Additionally, to perform electric field measurements inside liquid phantoms, the mixture should be put inside a shell. It has been demonstrated, that the presence of the shell can lead to an overestimation of electromagnetic field levels [161]. To overcome these limitations, a new method to retrieve APD is proposed in [154], [162] based on free space electric field measurement. More in detail, a reflectivity based solid phantom mimicking scattering characteristics of human skin at 60 GHz is employed, based on a Carbon+PDMS mixture. According to this technique, the phantom is illuminated on one side, while the electric field is measured on the back using a probe, then back propagated in space to retrieve APD at the phantom surface. Alternatively, the same phantom is proposed to retrieve APD through temperature-based method [38], [158], [162], [163]. Principles of this technique are schematically represented in Fig. 2.1. As shown, the antenna under test is placed at a certain distance from the phantom, designed with the same scattering properties of the human skin to perturb the antenna in the same way as it would be perturbed by the presence of the human body. The mmWave energy generated by the antenna is converted into heat inside the phantom due to dielectric losses and the temperature increase at the surface S2 is recorded using an IR camera. Indeed, the intensity of the IR signal emitted is directly proportional to the surface temperature. Finally, the APD at the evaluation surface S1 is reconstructed from the measured temperature rise.

It should be noted that the phantom optimization is tailored according to the specific technique employed. Indeed, for probe measurements in [154] phantom should be optimized to maximize the through-phantom transmission to ensure a measurable electric field behind the phantom. On the other hand, for IR based measurements, phantom should enhance the absorption to accurately convert the absorbed power into a heat pattern measured by an IR camera [38]. Finally, the use of a solid reflectivity-based phantom is very promising since can allow accurate assessment under realistic conditions, as it consider also the antenna/body interaction that may cause enhancement of user exposure levels and can have strong impact on device performances [164].

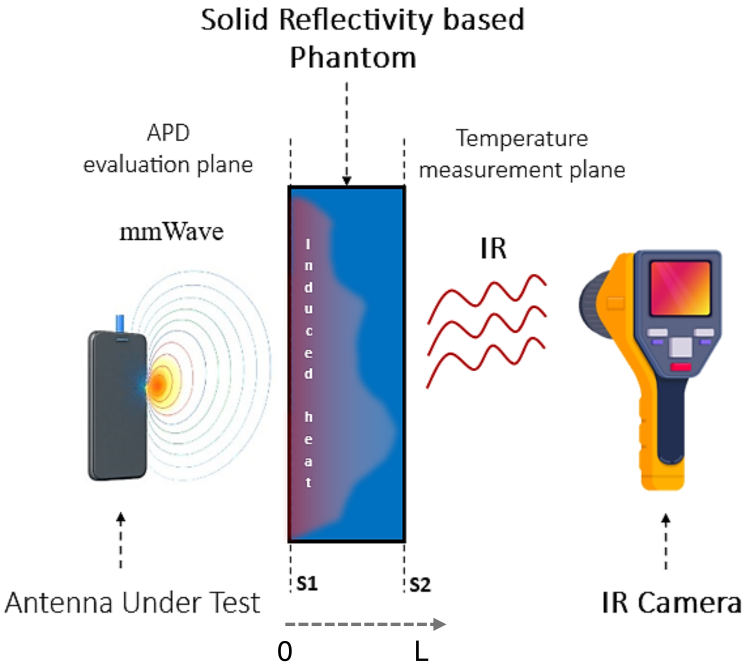

Figure 2.1: Schematical representation of the thermal-based APD measurement approach.

2.3 Research Gaps and Problem Formulation

As argued in previous sections, the assessment of human exposure generated by new 5G systems can require two different levels of evaluation: at public level and at the skin level. Indeed, the assessment of reference levels, considering directly RF fields in the environment, is a widespread approach to monitoring population exposure at newly installed BS antennas. In this context, as discussed above, ray-based techniques represent a very promising solution. However, before using them in real exposure scenarios, it is necessary to ensure high accuracy in simulation results, especially when different algorithms are employed and may provide slightly dissimilar electromagnetic field level predictions. Despite in literature this topic has been faced in several studies, an harmonized framework that allows to perform a fair comparison of the varying outcomes obtained with different algorithms has not been introduced so far.

Moreover, as can be deduced from Table 2.1, most of the presented works are carried out in the FR1 band. This is primarily related to the fact that 5G systems working in the FR1 band have been first introduced and deployed throughout the territory. Therefore, considerably more BS antennas are available and operative to carry out measurement campaigns and numerical simulations. Conversely, operative 5G networks in the FR2 band are not as widely diffused since they have been introduced quite recently and, due to the high frequencies involved, network design is much more complex. Moreover, wherever present, measuring and simulating electric field levels generated by mmWave antennas is very challenging due to the advanced and adaptive technologies they implement, such as beamforming or beam steering, that make repeatable measurements not straightforward to perform. In addition to this, to simulate the real BS behavior is extremely critical, since in many cases accurate information about the antenna is not provided and even when available, they only refer to the antenna envelope diagram.

On the other hand, since the exposure assessment with respect only to reference levels in the near field is not enough, an in-depth research study is also necessary to assess exposure close to the human body at the skin level. More in detail, as previously discussed, according to the 5G frequency band considered, two basic restrictions have been introduced: SAR and APD. While the SAR assessment is well established by means of tissue-mimicking phantoms and standardized protocols have been developed to perform compliant measurements, this is not the same for APD evaluation. Indeed, standardized dosimetric testing systems above 10 GHz have not been established so far. Some potential methods are proposed in the literature, based on electric field or thermal measurements and preliminary results suggest that solid phantoms are the most suitable solution for APD measurements, since they overcome main limitations of liquid and semi-solid phantoms.

More in detail, solid reflectivity based phantoms seem to be the most promising configuration, since they allow taking into account the antenna/body interaction. Focusing on thermal-based measurements, they are particularly suitable for power density assessment at mmWaves due to increasing with frequency losses resulting in a more effective conversion of the electromagnetic energy to heat. However, limited sensitivity is the major bottleneck of IR-based measurements. Indeed, the APD is directly obtained from temperature rise, therefore for an accurate reconstruction it's essential to enhance the Signal to Noise Ratio (SNR). To this aim, a possible solution is proposed in [158], in which a spectral frequency-domain filtering of the thermal noise, using the lock-in technique, is proposed. In this way, the ambient IR noise can be filtered, and the heat conduction effect can be mitigated. In addition to this, phantom characteristics play a crucial role in the sensitivity enhancement of the proposed approach since the temperature increase is strictly related to dielectric losses inside the structure, so phantom configuration should be carefully chosen to ensure measurable heating during the exposure. Therefore, it is clear that the phantom optimization both from the electromagnetic and thermal point of view is an essential step to perform reliable and accurate APD measurements using IR-based techniques. However, the optimization process is not straightforward since it involves several parameters that can also influence each other both from the electromagnetic and thermal point of view.

In addition to this, due to the recent introduction of 5G systems working at the mmWaves, studies in literature reproducing solid phantoms at these frequencies are very limited, as can be seen also from Table 2.2. For this reason, further analysis is necessary to investigate innovative techniques for phantoms design and development. Moreover, most of the works are focused on the realization of phantoms that emulate skin properties, but another important application for phantom is their employment in the OTA testing of wireless devices at mmWaves.

2.4 Thesis Original Contributions

Based on previous observations, in this thesis, the following research gaps with respect to the literature are addressed:

- development of an harmonized and systematic framework for the accurate assessment of different ray-based algorithms employed in population exposure evaluation;
- perform an extensive and comprehensive experimental and ray-based investigation on population exposure levels in the FR2 band, near an operative BS massive MIMO antenna.
- implementation and validation of analytical models for the electromagnetic and thermal design of solid reflectivity based phantoms is proposed and numerically validated;
- development and implementation of new optimization frameworks for the design of solid reflectivity-based phantoms employed in APD assessment through IR techniques;
- estimation of basic materials electromagnetic characteristics for phantom realization;

- design, development and characterization of a new phantom for OTA testing through innovative and advanced techniques.

Chapter 3

A Ray-Based Algorithm for the Assessment of Human Exposure in 5G Scenarios

This Chapter introduces the ray-based algorithm that is employed in this thesis for all forthcoming population level exposure analyses. A detailed description of the underlying working principles and theoretical bases is provided. Then, the algorithm is employed in several case studies to assess the electromagnetic field levels in different environments, ranging from urban to hospital scenarios, in both FR1 and FR2 bands. The outcomes are compared with safety limits for 5G frequencies, providing a comprehensive overview on population exposure levels through a statistical evaluation of computational results.

3.1 Ray-Based Algorithm Description

The ray-based algorithm that will be described in the following sections is implemented in a proprietary tool, named *Exact* and for this reason it will be referred with this denomination hereafter. *Exact* is an academic tool for the radio wave propagation in urban environments developed by the University of Naples Federico II [165]. The tool is written in IDL (Interactive Data Language) and it is able to simulate different propagation scenarios, regardless of size. The tool has been widely used for simulations in first and second generation system, up to the fourth generation system, providing valuable and reliable results, also compared to *on-site* measurements [166].

3.1.1 Working Principle and Theoretical Bases

Exact ray-based algorithm is implemented by means of the Vertical Plane Launch (VPL) technique, following the footsteps of the pioneer work by Liang and Bertoni [167]. Therefore, field computation involves three main steps that are described in detail below:

- Rays definition;
- Space scanning;
- Electromagnetic modeling.

Rays definition

In the algorithm, rays are fully described by their horizontal and vertical extensions. In the horizontal plane (HP), the area illuminated by the antenna is divided in angular sectors (referred to as *anxels*), whose width $d\theta$, for the sake of simplicity, can be here assumed constant and is set according to the maximum separation that the user can define between two rays dr, as shown in Fig. 3.1 (A). In this Figure, the *anxels* represent the HP trace of the radiated rays, and provide a discretization of the scanned area in the HP plane. In the vertical plane (VP), the antenna radiation diagram defines the ray intensity, see Fig. 3.1 (B). No discretization is provided in the VP because, as hereafter detailed, the propagation is studied in the VP plane via closed form equations.

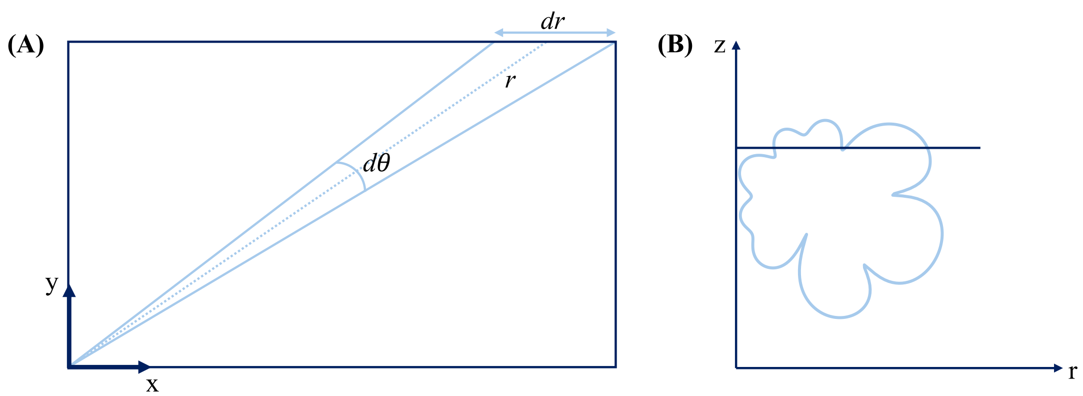

Figure 3.1: Definition of *anxel* in the horizontal plane (A) and in the vertical plane (B).

Space scanning

The 3D space is scanned with a two-steps procedure in the HP and in the VP. First, in the HP, the intersections of each anxel with the urban elements (i.e. buildings walls and vertexes) are identified and stored in a dynamic database. In Figure 3.2 (A), the light blue area represents an anxel originating from the antenna. The urban elements belonging to the anxel are stored and ordered by their distance from the source. Then, the VPs are scanned, by considering the vertical trace set by the radiation diagram and the urban elements identified in the HP scansion. The vertical pattern of the ray is modified by the interaction of the field with the buildings. As an example, in Fig. 3.2 (B) the ray hits the wall w_1 that reflects the incident field, while w_2 changes the vertical extension of the ray. The walls w_3 and w_4 are not hit by the incident ray, and the wall w_5 blocks the propagation of the field.
The interaction between a ray and a building can also be source of diffraction from the horizontal edges of the wall. According to the UTD [87], when a plane wave impinges on a vertical wall, a new set of rays departs from each edge and vertex of the wall. In the HP, each ray can be seen as generated by an image source d_i, which is identified and stored, as illustrated in Fig. 3.3 (B). More in detail, this Figure shows the HP representation of the diffracting sources ($d_1, \ldots\ d_n$) position generated by the field radiated by the primary source (Antenna), placed at distance r from the edge. When all the anxels from one (j-level) source have been analyzed, the set of the new found (j+1-level) sources of reflections and diffractions is stored and the algorithm restarts by scanning them with the same principle.

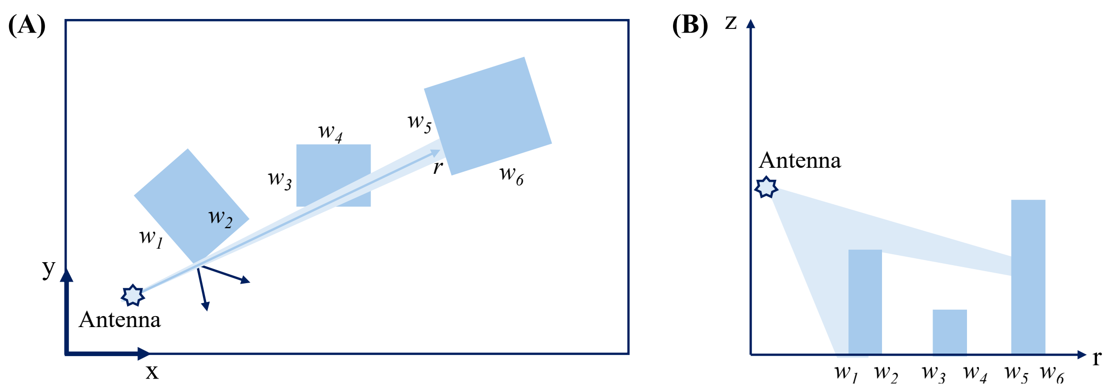

Figure 3.2: Horizontal (A) and vertical (B) space scansion.

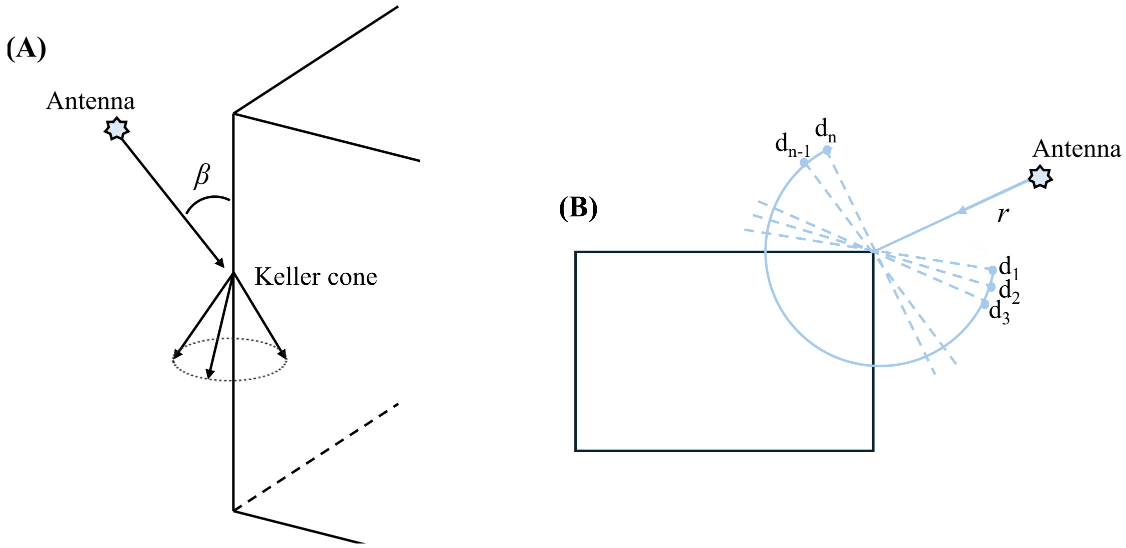

Figure 3.3: Keller cone (A) and visualization of the sources of diffraction in the horizontal plane (B).

Electromagnetic modeling

The electromagnetic theory that describes reflection, scattering and diffraction phenomena is not straightforward to implement in a numerical tool [87], [168], [169], [170],[171]. *Exact* employs only closed form solutions, with a significant computational time reduction, as detailed in the following. Most of the commercial antennas radiate a linearly polarized field: hence, a reference coordinate system centered at the phase center of the antenna is assumed and the field vector radiated by the antenna ($\mathbf{E}_i$) can be written as:

$$\mathbf{E_i} = \hat{e}_i \frac{E_0}{k_i r} e^{-j\mathbf{k_i}\cdot\mathbf{r}} \tag{3.1}$$

where E_0 is the field amplitude parameter related to the radiated power, $\mathbf{k}_i$ is the electromagnetic wavenumber, $\hat{e}_i$ defines the wave polarization, whose direction is usually perpendicular or parallel to the plane identified by the vectors $\mathbf{k_i}$ and $\mathbf{r}$, $\mathbf{r}$ being the vector pointing from the antenna center. Anyway, the tool can manage each polarization state.

Reflection from buildings is accounted by means of the Fresnel coefficients, in accordance with the hypothesis of flat building walls. More in detail, when an incident field encounters impedance mismatches, a portion of it is reflected, while the remaining portion is transmitted inside the medium. If a stack of N layers with planar boundaries is considered (see Fig. 3.4), each of them characterized by its own relative permittivity and permeability (ε^*_{ri}, μ^*_{ri}), according to Fresnel's laws it is possible to define reflection (r) and transmission (t) coefficients, for Transverse Electric (TE) and Transverse Magnetic (TM) polarization, at each interface. Taking into account the mth plane interface, which separates the m and $m+1$ homogeneous media, r and t can be written as [172]:

$$r^{TE}_{m(m+1)} = \frac{\mu^*_{r(m+1)} k_{zm} - \mu^*_{rm} k_{z(m+1)}}{\mu^*_{r(m+1)} k_{zm} + \mu^*_{rm} k_{z(m+1)}} \tag{3.2}$$

$$r^{TM}_{m(m+1)} = \frac{\varepsilon^*_{r(m+1)} k_{zm} - \varepsilon^*_{rm} k_{z(m+1)}}{\varepsilon^*_{r(m+1)} k_{zm} + \varepsilon^*_{rm} k_{z(m+1)}} \tag{3.3}$$

$$t^{TE}_{m(m+1)} = \frac{2\mu^*_{r(m+1)} k_{zm}}{\mu^*_{r(m+1)} k_{zm} + \mu^*_{rm} k_{z(m+1)}} \tag{3.4}$$

$$t^{TM}_{m(m+1)} = \frac{2\varepsilon^*_{r(m+1)} k_{zm}}{\varepsilon^*_{r(m+1)} k_{zm} + \varepsilon^*_{rm} k_{z(m+1)}} \tag{3.5}$$

Where $k_0 = \omega\sqrt{\mu_0 \varepsilon_0} = \omega/c = 2\pi/\lambda$ is the free-space wavenumber, $k_m = k_0\sqrt{\mu^*_{rm}\varepsilon^*_{rm}}$ is the wavenumber in the mth layer,

$$k_{zm} = \sqrt{k_m^2 - |\mathbf{k}_\perp|^2} \tag{3.6}$$

and $\mathbf{k}_\perp$ is the projection of the incident wavenumber vector on the plane $z = 0$.

The electromagnetic diffraction plays a key role in the urban propagation, mainly in cities where the density of buildings is extremely high. In this ray-based algorithm, an appropriate formulation of the UTD is used, as detailed in the following. When a single ray impinges on a vertical edge, the diffracted field is distributed on a cone, named as the Keller cone, with axes given by the edge, and aperture β equal to the incident angle, see Fig. 3.3 (A). The diffracted field ($\mathbf{E}^d$) is expressed in terms of a diffraction coefficient D [170]:

$$\mathbf{E^d} = \mathbf{E_i} \cdot DAe^{(-j\mathbf{k}\cdot\mathbf{r}_F)} \tag{3.7}$$

where $\mathbf{r}_F$ is the vector distance between the edge and the evaluation point, $\mathbf{E}_i$ is the incident field, A is a spatial attenuation factor.

Whenever natural surfaces are under concern, as it is the case to study diffusion from the rough terrain surrounding the buildings, the use of the fractal geometry gives a huge improvement to the existing classical models [168]. In *Exact* algorithm,

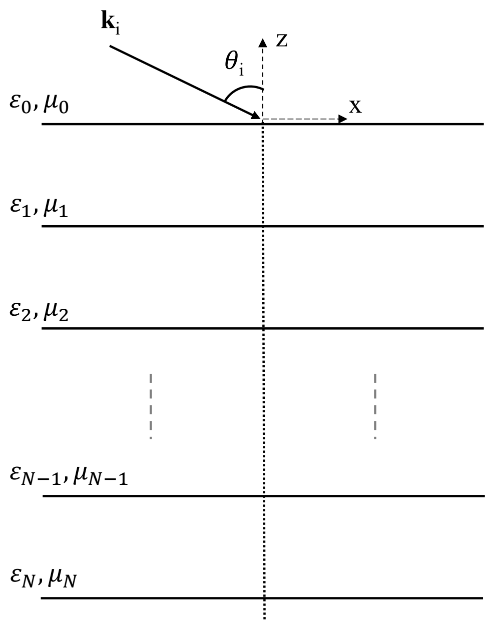

Figure 3.4: Schematic representation of a flat-layered structure with a plane wave incident on the stratification.

the roughness is provided in terms of the fractional Brownian motion (fBm) model. The fBm, characterized by only two parameters (the fractal dimension D and the topotesy T), is widely considered as the most appropriate model of natural surfaces. Depending on the surface roughness the field from a natural surface can be evaluated with different approaches [169]. For instance, for small roughness [169], the scattered field power density is evaluated, in the frame of the small perturbation model, as, [168],[169]:

$$\left|\langle E_q^2\rangle\right|^2 = \frac{4A_i|k^2 cos\theta_2 cos\theta_2 \beta_{pq}|^2}{2\pi R} \cdot \frac{S_0}{\eta_{xy}^{\alpha}} \tag{3.8}$$

where A_i is the illuminated area, θ_1 is the incident angle, θ_2 is the scattered angle, β_{pq} is a coefficient that depends on the polarization incidence and scattering angles and complex dielectric constants [168], η_{xy} is a parameter dependent on incident and scattered wavenumbers, S_0 is a spectral parameter dependent on both D and T [168], $\alpha = 8 - 2D$.

3.1.2 Input settings and parameters

The algorithm requires as input the most relevant elements for propagation, such as buildings and topography as well as all parameters about transmitting antenna. Buildings are described only by vertex position and heights. In *Exact* they are modeled as prisms with walls perpendicular to the ground and their base polygons are accepted of any, however irregular, shape. Their relative permittivity and conductivity, as well as that of the ground, are stored and can be set by the user for each individual object present in the simulated scenario. More in detail, for each element present in the scenario it is necessary to define:

- Real part of wall relative permittivity (ε_{rw});
- Imaginary part of wall relative permittivity (ε_{iw});
- Effective indoor specific attenuation factor (α_w);
- Real part of glass relative permittivity (ε_{rg});
- Imaginary part of glass relative permittivity (ε_{ig});
- Wall thickness;
- Glass thickness;
- Percentage of window area in the wall (% window);.

These parameters can be set independently by the user, or it is also possible to select a specific type of area (residential, historical or office) with default geometrical and dielectric characteristics, reported in Table 3.1.

Characteristic	**Residential Area**	**Historical Area**	**Office Area**
ε_{rw}	5.50	5.50	5.50
ε_{iw}	0.03	0.03	0.03
α_w [dB/m]	0.80	0.80	0.80
ε_{rg}	4.00	4.00	4.00
ε_{ig}	0.02	0.02	0.02
Wall thickness [m]	0.35	0.50	0.35
Glass thickness [m]	0.02	0.02	0.04
% window	0.10	0.10	0.35

Table 3.1: Default dielectric characteristics of buildings in different areas.

The complex permittivity of terrain used for reflection, diffraction and rough surface scattering calculation is defined as follows:

$$\varepsilon_r^*(f) = \varepsilon_\infty - j\frac{\sigma}{2\pi f \varepsilon_0} \tag{3.9}$$

Where $\varepsilon_\infty = \varepsilon_r^*(f \to \infty)$, and f is the frequency.

As for buildings, also for the terrain it is possible for the user both to set custom properties or to select the default values proposed by the tool for different terrain types, reported in Table 3.2.

Constants	**Downtown**	**Suburban**	**Agricultural and Vegetated Land**
ε_∞	5.00	4.00	8.75
σ	0.01	0.01	0.17

Table 3.2: Default dielectric characteristics of the terrain.

Antenna description is provided by means of its position and altitude, radiated power, polarization and 3D radiation diagram. The 3D radiation diagram is described by considering the projection of the radiation diagram onto the horizontal and vertical planes. More in detail, the vertical projection refers to planes passing by the secant of the angular sectors identified in the horizontal plane projection.

3.1.3 Calculation output

In this algorithm, the field is computed on a regular grid with a pixel dimension chosen by the user. The resulting field evaluated in each point of this output grid is formed by the contribution of direct, reflected and diffracted field. Due to the random nature of the urban environment and on the output pixel dimension with respect with the electromagnetic wavelength, the field phases have to be modeled as uniformly distributed random variables. In fact, a coherent contributions' sum would cause a wrong interference fringes effect in the output electromagnetic field map; then an incoherent contributions' sum is performed in this tool.
The computation stops when for each single ray the field intensity decreases below a threshold value (which will be discussed in the following chapters) independently set by the user and no limits are set for the number of possible reflections and diffractions. This characteristic represents a remarkable added value of the algorithm compared to the existing ones, in which usually the maximum number of reflections and diffractions is limited. Indeed, using this approach, only contributions that have a significant impact on the propagation are evaluated. The threshold value can be

appropriately set, in accordance to the goal of the prediction.
The overall performances of the algorithm, in terms of precision and computational time, are related to the choice of the anxel width, the input power and the field threshold. In this thesis, the main outputs of the tool that will be considered are intensity maps of electric field [V/m] and received power [dBm] (see Fig. 3.6 (B)), but it is possible to perform other analysis, i.e. best server evaluation (see Fig. 3.5 (B)), indoor coverage prediction (see Fig. 3.6 (C)), power density distribution and evaluation of pulse delay and spreading information. It should be noted that if a point in the intensity map lays in an area occupied by a building, the computed value refers to the electromagnetic field at a given height over the building roof. If a point in the intensity map lies in an area free from buildings, the computed value refers to the field evaluated at the same height over the ground.

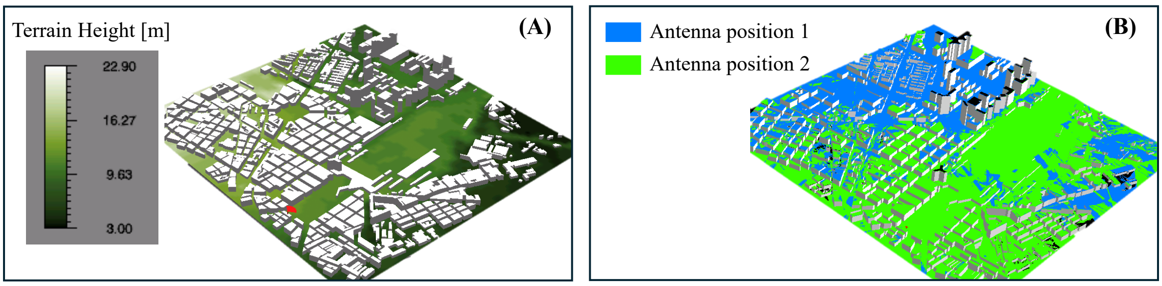

Figure 3.5: Visualisation of urban scenario with corresponding terrain height (A) and example of best server evaluation with two different antenna positions (B). The antenna height is 47 m.

3.2 Assessment in the FR1 Band

In this section the ray-based algorithm previously described is employed for exposure assessment in the FR1 band, specifically at 3.7 GHz, in three different types of scenario: urban, suburban, and hospital environment. For each of these cases, the exposure levels are evaluated considering the following metrics: maximum (max), 50th percentile (50p), 95th percentile (95p), average and standard deviation (STD) of the electric field.

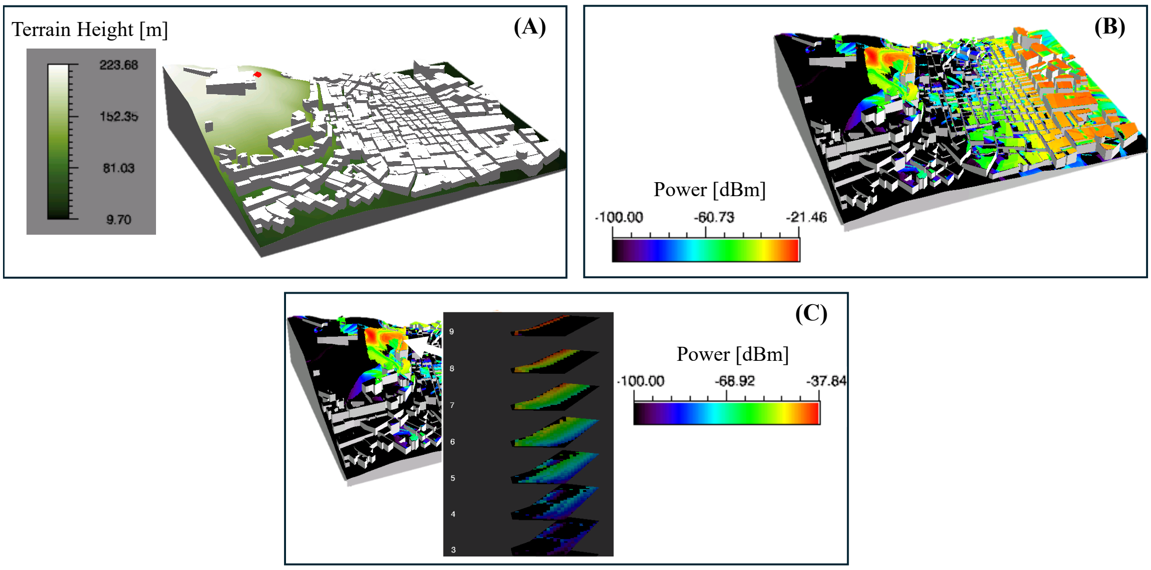

Figure 3.6: Visualisation of urban scenario with corresponding terrain height (A); power intensity map [dBm] (B); indoor evaluation in the building pointed with the white arrow at different evaluation plane; reported power levels [dBm] are computed inside the building with specific α_w (C).

3.2.1 Suburban scenario

The scenario selected for the first analysis consists of a very small portion (80 m x 84 m) of a suburban area located in Napoli (Italy), characterized by the presence of 4 buildings [173]. Its representation is depicted in Fig. 3.7, in which the antenna position is marked in yellow, while the buildings considered for the simulation are outlined in green and blue color.

In this scenario, a standard 5G Active Antenna System (AAS) New Radio (NR) system operating at 3.7 GHz has been placed, operating with the envelope antenna diagram shown in Fig. 3.8. Using the envelope antenna diagram represents a "worst case scenario" since the exposure is evaluated taking into consideration all the possible beams and the instantaneous irradiation produced by a single beam in the event of traffic; this approach, that will be proposed also in future analysis, certainly leads to an overestimation of the global exposure. However, this information is usually the only one available about the 5G antennas, and represents also the best choice to compare numerical simulation results with respect to *on-site* measurements of broadcast beam, which is static and not dynamically beam formed like traffic beams.

The simulations have been carried out considering two different 5G NR deploy-

Figure 3.7: Suburban scenario situated in Napoli (Italy); in yellow antenna position is marked; simulated buildings are outlined in green and blue. *© 2026 IEEE*

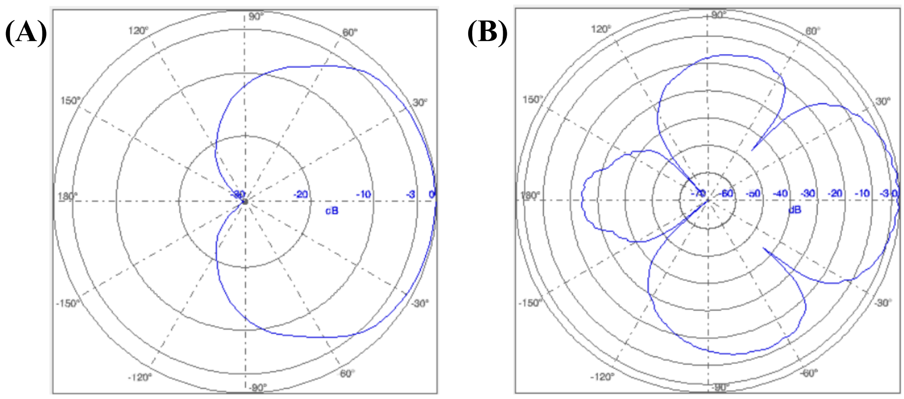

Figure 3.8: 5G NR envelope antenna diagram at 3.7 GHz; (A) horizontal radiation pattern; (B) vertical radiation pattern.

ments [174]:

- Macro-cellular system (see Table 3.3 for details);
- Small cell system system (see Table 3.3 for details).

Building materials are set as residential area (see Table 3.1), while their heights are reported in Table 3.4. Characteristics about the simulated scenario have been

Parameter	**Macro cell**	**Small cell**
Frequency	3.7 GHz	3.7 GHz
Antenna	5G AAS – envelope	5G AAS – envelope
BS Height	20 m	3 m
BS location	450479.77, 4511481.38	450479.77, 4511481.38
Beam pointing	110°	110°
Power	1 W	0.01 W
Downtilt	6°	0°
Simulation plane	Horizontal	Horizontal
Simulation plane height	1.5 m from the ground	1.5 m from the ground
Pixel dimension	1 m x 1 m	1 m x 1 m
Map dimensions	80 m x 84 m	80 m x 84 m

Table 3.3: Simulation parameters for macro cell and small cell scenarios. *© 2026 IEEE*

extrapolated using OpenStreetMap [175] and Google Earth map [176], and its visualization in *Exact* tool is shown in Fig. 3.9. Ray launching analyses have been carried out considering one single diffraction and a threshold for rays propagation equal to -135 dBm for both macro and small cell configuration.

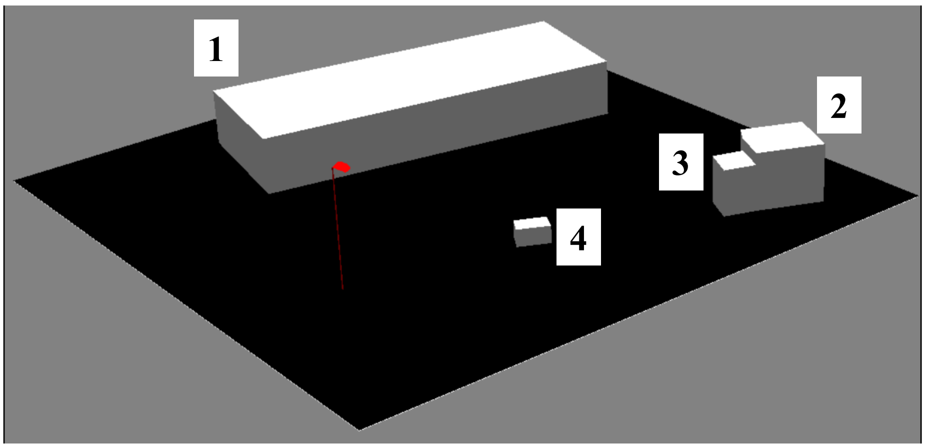

Figure 3.9: Simulated scenario for ray launching simulations; in red antenna in the case of macro cellular scenario is marked.

Building	**Height** [m]
Building 1	10
Building 2	10
Building 3	8
Building 4	3

Table 3.4: Building heights.

Macro cell scenario

Simulation output in the case of macro-cell scenario is reported in Fig. 3.10. The output shows the electromagnetic field levels at a receiver height of 1.5 meters from the ground. If the points in the intensity map lay in the area occupied by a building, the output value refers to the electromagnetic field at 1.5 meters over the building roof. If a point in the intensity map lies in an area free from buildings, the output value refers to the field evaluated at the same height over the ground. Statistical analysis of ray launching results is reported in Table 3.5. As can be seen, 95p and max values are far below exposure limits for popoluation, both considering ICNIRP and actual Italian regulations.

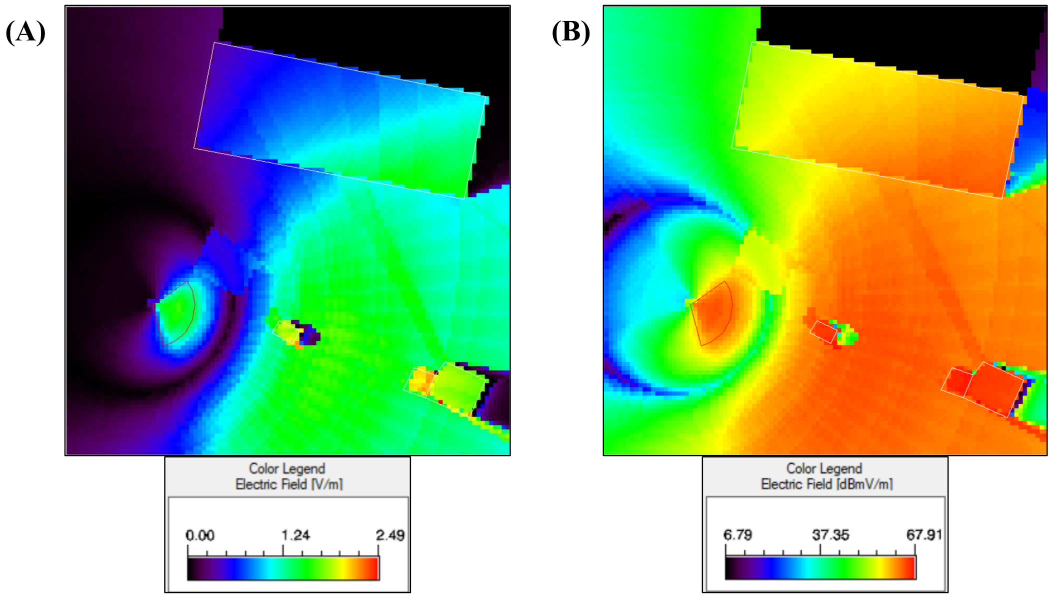

Figure 3.10: Electric field levels for macro cellular scenario; (A) V/m and (B) dBmV/m. © *2026 IEEE*

50p	95p	max	Mean	STD
0.68	1.56	2.49	0.71	0.59

Table 3.5: Statistical analysis of numerical results for macro cell scenario. All values are given in V/m.

Small cell scenario

On the other hand, the electric field levels obtained from the simulations for small cell are reported in Fig. 3.11. As in the case of macro cell scenario, the output shows the electric field levels at 1.5 meters receiver height. Statistical analysis of computational results is reported in Table 3.6. As can be seen, 95p and max values are also in this case far below exposure limits for population, both considering ICNIRP and actual Italian regulations. Moreover, as expected, electric field levels are lower than the macro cell scenario, since this configuration is intended to serve small areas.

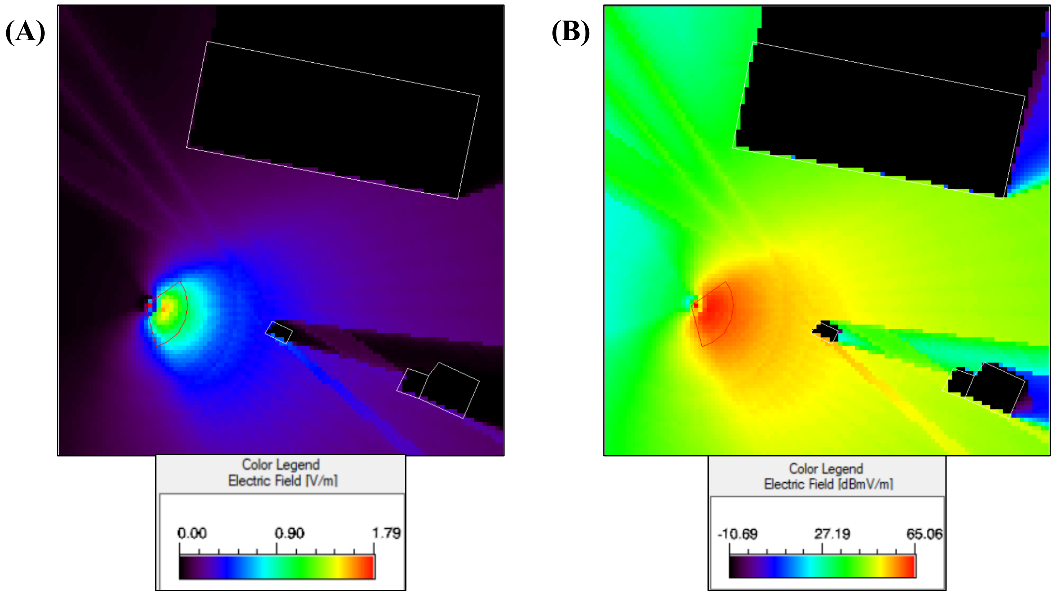

Figure 3.11: Electric field levels for small cellular scenario; (A) V/m and (B) dBmV/m. © *2026 IEEE*

50p	95p	max	Mean	STD
0.084	0.45	1.79	0.14	0.18

Table 3.6: Statistical analysis of numerical results for small cell scenario. All values are given in V/m.

3.2.2 Urban Scenario

A different urban scenario is selected, located near a 3.7 GHz BS antenna in Rome (Italy). Its representation is reported in Fig. 3.12, in which the antenna position is marked in yellow and is characterized by the radiation shown in Fig. 3.13. Five buildings are present in the scenario, with the height characteristics reported in Table 3.7 and simulated as residential area. The final simulated scenario is depicted in Fig. 3.14 while details about simulation parameters are reported in Table 3.8.

Computational analyses have been carried out considering one single diffraction and a threshold for rays propagation equal to -135 dBm. Results in terms of electric field levels in V/m and dBmV/m are shown in Fig. 3.15. The output depicts the electromagnetic field levels at a receiver height of 1.5 meters from the ground. As in the previous case, following the rationale of the tool, the output values of points in the intensity map that lay in the area occupied by a building refers to the electromagnetic field at 1.5 meters over the building roof. On the other hand for points in the intensity map that are located in areas free from buildings, the corresponding simulated values refer to the field evaluated at the same height over the ground. Statistical analysis on electric field levels (see Table 3.10), proved that both 95p and max are below exposure limits for population, both considering ICNIRP and actual Italian regulations and this result will be confirmed by experimental analysis carried out in the following Chapter.

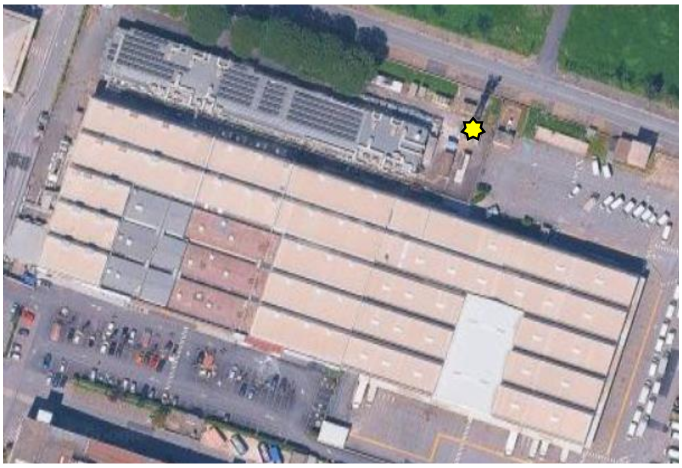

Figure 3.12: Urban scenario situated in Rome (Italy); in yellow antenna position is marked.

Building	**Height** [m]
Building 1	8
Building 2	7
Building 3	6
Building 4	18
Building 5	18

Table 3.7: Building heights.

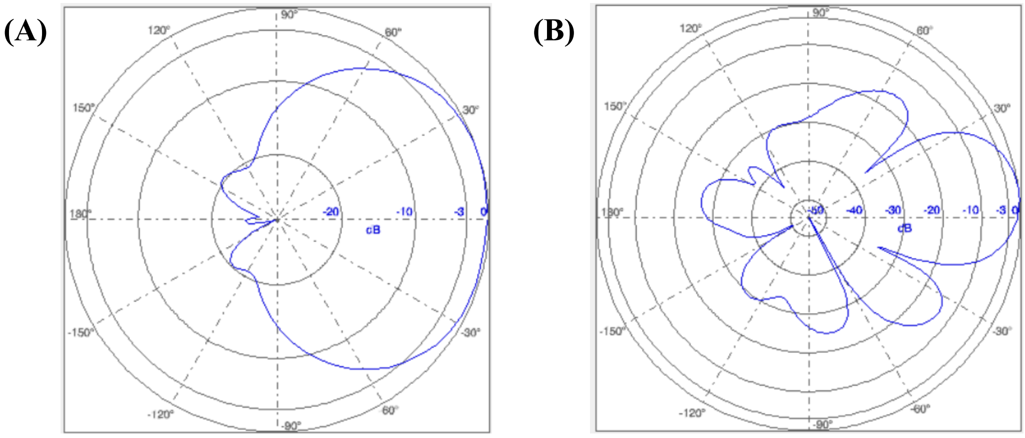

Figure 3.13: Antenna diagram at 3.7 GHz; (A) horizontal radiation pattern; (B) vertical radiation pattern.

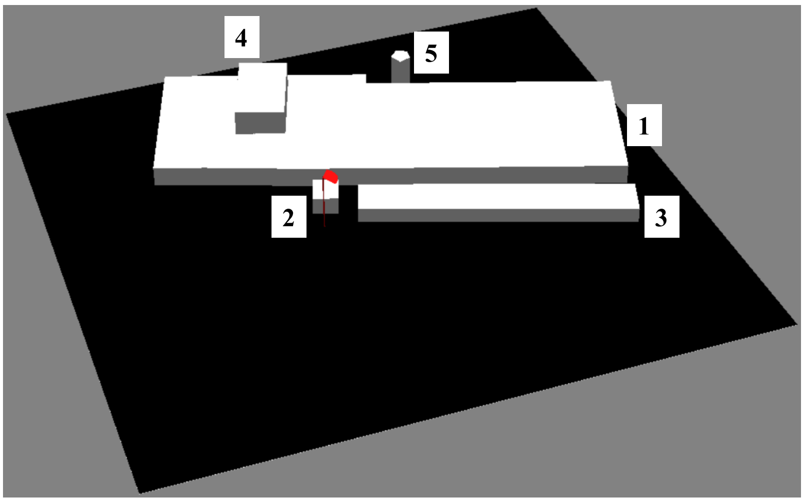

Figure 3.14: Simulated scenario for ray launching simulations in Rome (Italy); in red antenna position is marked.

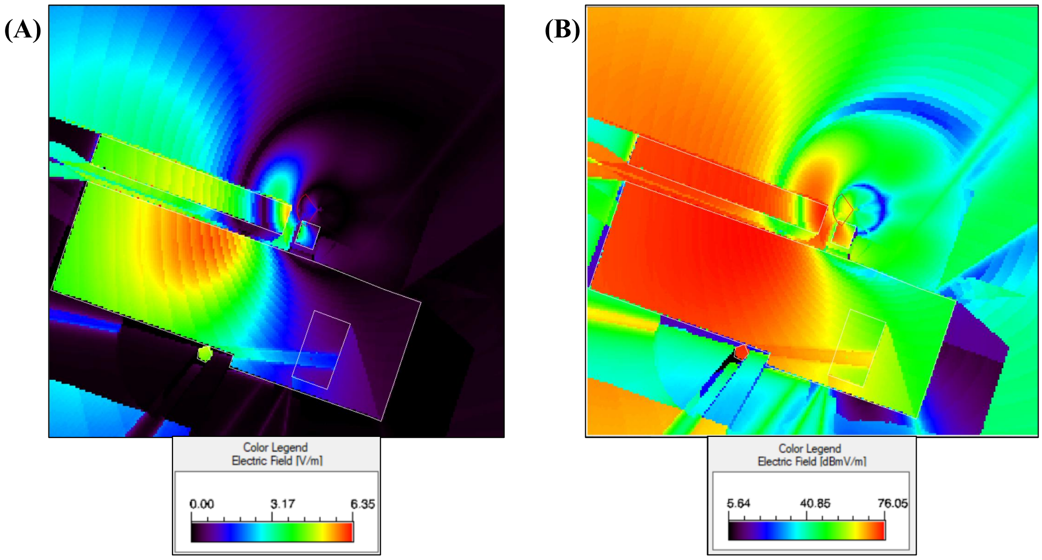

Figure 3.15: Electric field levels; (A) V/m and (B) dBmV/m. © *2026 IEEE*

Parameter	**Value**
Frequency	3.7 GHz
Antenna	5G - envelope
BS Height	22.1 m
BS location	299858.67, 4636959.48
Beam pointing	270°
Power	22 W
Downtilt	6°
Maximum Gain	22.9 dBi
Simulation plane	Horizontal
Simulation plane height	1.5 m from the ground
Pixel dimension	1 m x 1 m
Map dimensions	229 m x 217 m

Table 3.8: Simulation parameters for Rome scenario.

50p	**95p**	**max**	**Mean**	**STD**
0.32	4.92	6.35	1.39	1.7

Table 3.9: Statistical analysis of numerical results for Rome scenario. All values are given in V/m.

3.2.3 Hospital scenario

The hospital scenario selected for this simulation study is the Department of Haematology of "Ospedale Maggiore di Parma", situated in Parma (Italy) and depicted in Fig. 3.16 [177]. In this environment, assessing electric field levels plays a crucial role for two main reasons: first, the continuity and quality of service is essential to provide reliable digital healthcare services and, second, in hospital environments, where several medical devices work by means of electromagnetic fields, potential interferences also need to be considered. In this context, 5G non-public networks represent a promising solution for healthcare ecosystem and for this reason, the European Regulation EU 2020/1070 [178] allows the installation with a simplified authorization procedure of low operating power access points in limited areas, known as Small Area Wireless Access Point (SAWAP). This simplified procedure can be applied to class E2 with Equivalent Isotropic Radiated Power ($EIRP$) ≤ 2 W and class E10 with $EIRP \leq 10$ W small cell deployments, defined in the IEC 62232 European standard [56]. Therefore, ray launching analyses are carried out in this real hospital-case scenario, assuming the installation of 5G non-public network working at 3.7 GHz in two different configurations:

- Class E10 small cell with 40 dBm (10 W EIRP) antenna input power and 4-meter-high BS antenna;
- Class E2 small cell with 33 dBm (2 W EIRP) antenna input power and 2-meter-high BS antenna.

The antenna envelope diagram employed in this analysis is the one presented in Fig. 3.13.

Figure 3.16: Hospital scenario situated in Parma (Italy); in yellow antenna position is marked

As shown in Fig. 3.16, the hospital department consists of three buildings with different heights (see Table 3.10), simulated with the electromagnetic characteristics of a residential area. All details about simulation parameters are reported in Table 3.11, while the final simulated scenario is shown in Fig. 3.17. Ray launching simulations have been carried out considering one single diffraction and a threshold for rays propagation equal to -135 dBm for both SAWAP configurations. This threshold is chosen since lower power values are not relevant for radio coverage studies or for assessing human exposure. Moreover, this threshold represents the typical sensitivity of the equipment used to carry out measurement campaigns.

Building	**Height** [m]
Building 1	5
Building 2	6
Building 3	6

Table 3.10: Building heights.

Parameter	Class E10	Class E2
Frequency	3.7 GHz	3.7 GHz
Antenna	5G AAS – envelope	5G AAS – envelope
BS Height	4 m	2 m
BS location	603371.2208, 4961750.8984	603371.2208, 4961750.8984
Beam pointing	0°	0°
EIRP	10 W	2 W
Downtilt	0°	0°
Simulation plane	Horizontal	Horizontal
Simulation plane height	1.5 m from the ground	1.5 m from the ground
Pixel dimension	1 m x 1 m	1 m x 1 m
Map dimensions	149 m x 139 m	149 m x 139 m

Table 3.11: Simulation parameters for E10 and E2 small cell class.

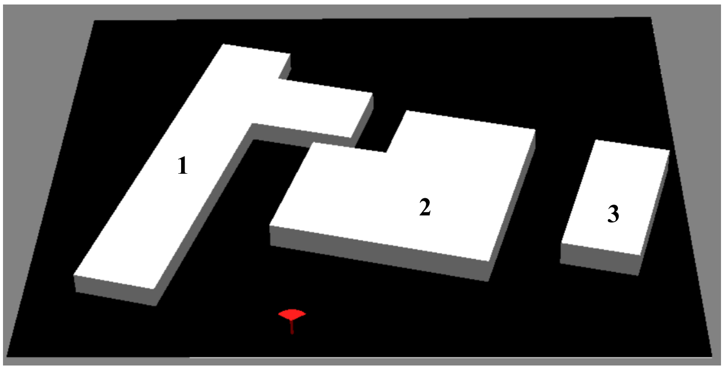

Figure 3.17: Simulated scenario for ray launching simulations in hospital environment; in red antenna position is marked.

E10 Class

Electric field levels obtained in the case of SAWAP E10 small cell class are shown in Fig. 3.18 in V/m (A) and dBmV/m (B). As in previous cases, the field is evaluated at 1.5 meters receiver height. Statistical analysis on electric field levels has been carried out (see Table 3.12), demonstrating that both 95p and max are below exposure limits for population, both considering ICNIRP and actual Italian regulations. In this case, compliance with the electromagnetic compatibility limits defined by IEC 60601-1-2 [179] for general electronic medical equipment is also considered, with both the

95th percentile and max values remaining below the specified thresholds (3 V/m for professional healthcare facility environment).

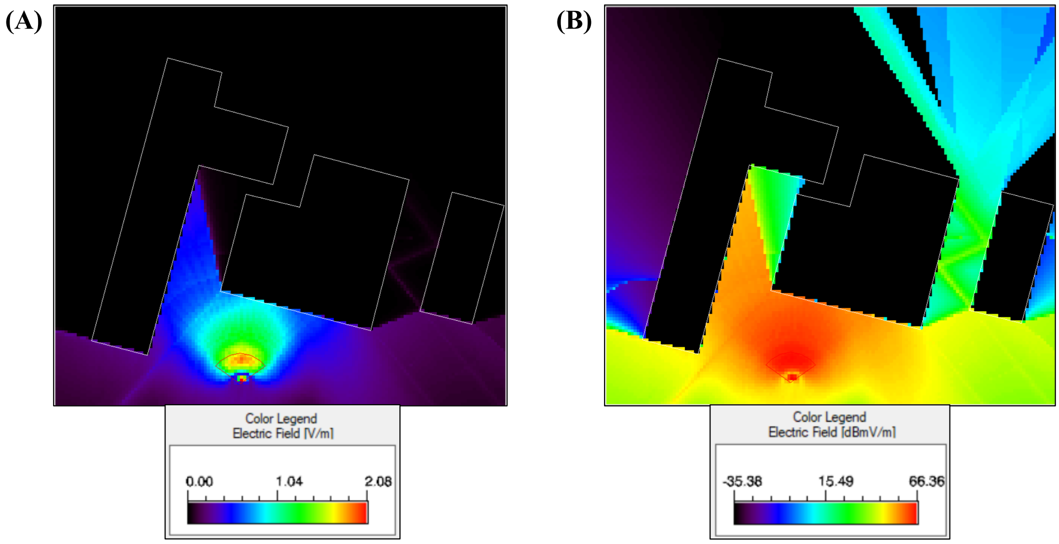

Figure 3.18: Electric field levels for E10 small cell class; (A) V/m and (B) dBmV/m.

50p	95p	max	Mean	STD
0	0.60	2.08	0.10	0.24

Table 3.12: Statistical analysis of numerical results E10 small cell class in the hospital scenario. All values are given in V/m.

E2 Class

On the other hand, electric field levels obtained in the case of SAWAP E2 small cell class are shown in Fig. 3.19 in V/m (A) and dBmV/m (B). As in previous cases, the field is evaluated at 1.5 meters receiver height. Statistical analysis on electric field levels has been carried out (see Table 3.13), demonstrating that both 95p and max are below exposure limits for population, both considering ICNIRP and actual Italian regulations. This is also true if the mean value and the STD are considered. Furthermore, as for the E10 configuration, the compliance for electromagnetic compatibility with medical devices is considered and the 95p is still below these limits (3 V/m for professional healthcare facility environment). The maximum value in this case is at the limit, but this value is obtained only in close proximity to the antenna, where medical devices should not be present, according to the chosen configuration. Nevertheless, this information should be carefully considered if the antenna position has to be changed. Overall, these results highlight the importance of robust ray-based algorithms that can accurately model electromagnetic field distributions, which is essential for the safe deployment of new 5G networks, particularly in critical environments, like hospitals.

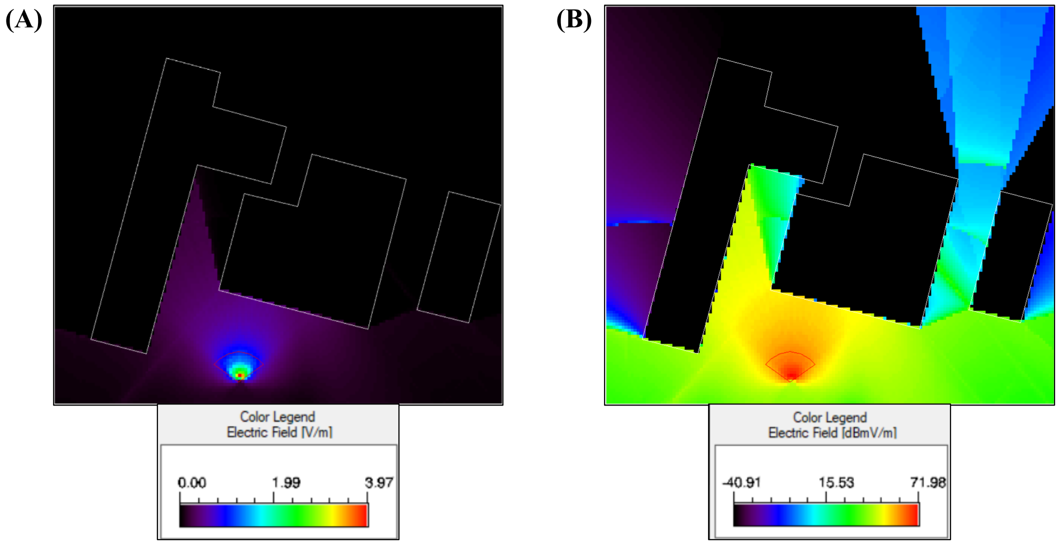

Figure 3.19: Electric field levels for E2 small cell class; (A) V/m and (B) dBmV/m.

50p	95p	max	Mean	STD
0	0.33	3.97	0.06	0.16

Table 3.13: Statistical analysis of numerical results E2 small cell class in the hospital scenario. All values are given in V/m.

3.3 Assessment in the FR2 band

Moving to higher frequencies, specifically from the FR1 band to the FR2 band, increases the complexity in 5G network design. Indeed, as discussed in previous chapters, higher frequencies lead to an increase in signal attenuation and, consequently, the necessity of accurate planning the installation of 5G BS in the environment becomes even more relevant. For this reason, in this section a ray-based study is proposed in the FR2 band, specifically at 27 GHz, in different real case scenarios. First, a real complex scenario is considered in which a 27 GHz massive MIMO BS is actually located. Then, in the previously presented hospital scenario, the installation of a 5G non-public network working in the FR2 band is studied and compared with the solution at 3.7 GHz in terms of human exposure assessment.

3.3.1 Complex Urban Scenario

The first location under study is an urban area in Turin (Italy) city, depicted in Fig. 3.20, where a 27 GHz massive MIMO BS is actually installed [180]. The antenna covers three different sectors, identified as PCI4, PCI5 and PCI6, where PCI stands for Physical Cell Identity. It can be seen that the selected scenario, although complex, is mainly composed of buildings, making it suitable for the following ray launching analysis. Moreover, the antenna is located near an hospital, and this aspect makes even more interesting to investigate the field levels in nearby areas. Hospital position is highlighted in yellow in Fig. 3.21 where the simulation scenario is presented. The cartographic data for simulations, together with the antenna radiation pattern and other characteristics of the scenario have been provided by Vodafone, that is the antenna operator. As done in previous analysis, the antenna envelope diagram is considered, since this represents the "worst-case" scenario for human exposure assessment, and also because this is the information that usually can be obtained about the 5G massive MIMO BS pattern. More in detail, horizontal and vertical radiation patterns are shown in Fig. 3.22.

Figure 3.20: Urban scenario situated in Turin (Italy); antenna position is marked in yellow.

The overall simulated scenario covers an area of about 500 m x 600 m and is shown in Fig. 3.21. The scene is composed by 230 buildings, characterized by different heights, which in this case will not be reported due to their large number. As in previous cases, for building materials the residential area characteristics are chosen. Detailed antenna characteristics (i.e. input power, height, tilt..) have been provided directly by the mobile operator (Vodafone) and are reported in Table 3.14, together with simulation parameters.

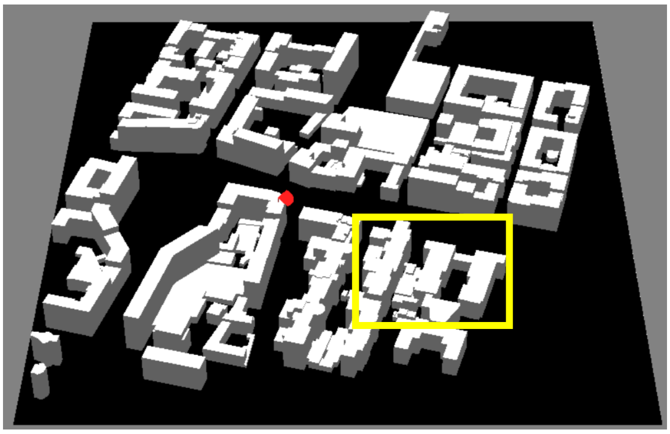

Figure 3.21: Simulated scenario of Turin (Italy); in red antenna position is indicated; hospital position is highlighted in yellow.

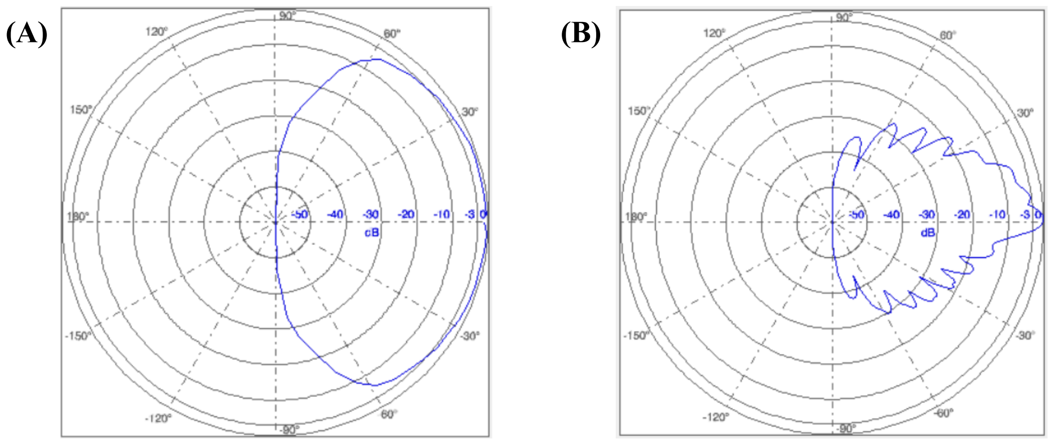

Figure 3.22: Massive MIMO antenna envelope diagram at 27 GHz; (A) horizontal radiation pattern; (B) vertical radiation pattern. *© 2026 IEEE*

Parameter	Value
Frequency	27 GHz
Antenna	massive MIMO antenna
BS Height	33.5 m
BS location	395517.19, 4988683.86
Beam pointing (PCI4, PCI5, PCI6)	85°, 150°, 310°
Power	0.002 W
Downtilt (PCI4, PCI5, PCI6)	5°, 5°, 3°
Maximum Gain	26.98 dBi
Simulation plane	Horizontal
Simulation plane height	1.5 m from the ground
Pixel dimension	1 m x 1 m
Map dimensions	500 m x 600 m

Table 3.14: Simulation parameters for Turin (Italy) scenario.

Ray launching analyses have been carried out considering one single diffraction phenomena and a threshold for rays propagation equal to -135 dBm.

PCI4 results

Results of ray launching simulations for PCI4 are shown in Fig. 3.23. In this case, together with the electric field levels in V/m, also the power levels in dBm are reported, as this information will be useful for future analysis. It is already clear from this figure that field levels are very low, and this point is confirmed by looking at the statistical analysis on electric field in Table 3.15. Indeed, the 95p and max value are far below exposure limits for population and for medical devices compatibility. However, it should be noted that this result is not representative of the real exposure scenario, since only the "always on" electric field levels due to broadcast beams, used to send control signals for UE access, are considered. Thus, the contribution of traffic beams electric field levels existing "in the air" only in the presence of a UE is not simulated. Nevertheless, this point is neither straightforward to simulate nor to measure, and obtaining repeatable results is also challenging. Therefore, in light of what is recommended by the IEC 62232 standard [56], measurements are usually performed by considering control signals, which allows the comparison with numerical simulations based on the antenna envelope diagram and also to carry out repeatable measurement campaigns.

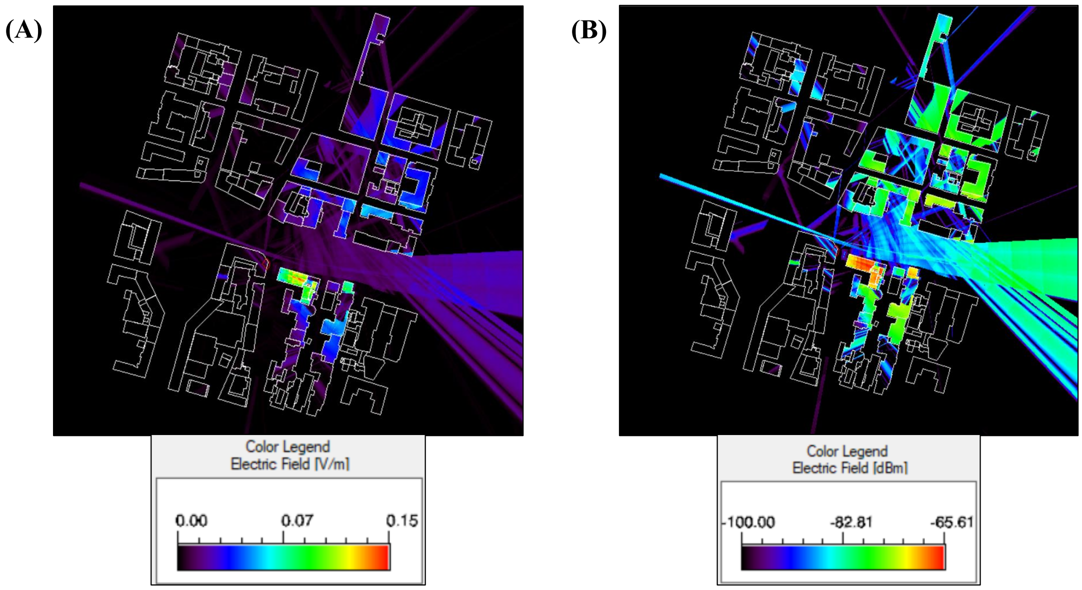

Figure 3.23: (A) Electric field levels [V/m] for PCI4 cell; (B) Power levels [dBm].

50p	95p	max	Mean	STD
0	0.024	0.15	0.004	0.01

Table 3.15: Statistical analysis of numerical results in PCI4 scenario. All values are given in V/m.

PCI5 results

Results of computational analyses for PCI5 are shown in Fig. 3.24 both in terms of electric field [V/m] (A) and power levels [dBm] (B). As in previous case, the electric field levels are far below exposure limits for population, and this outcome is confirmed by the statistical analysis reported in Table 3.16.

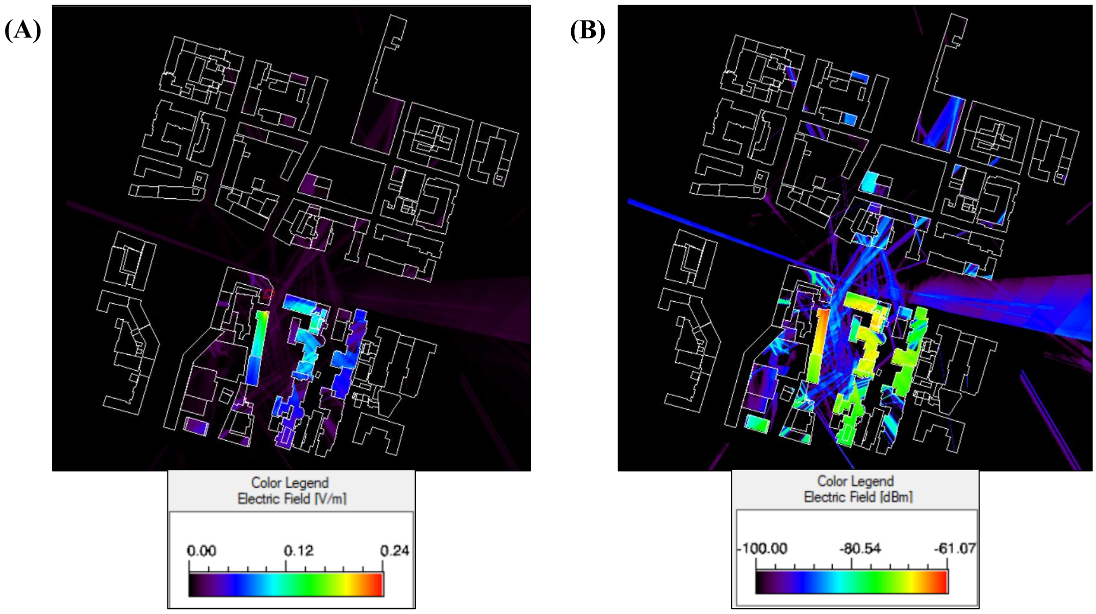

Figure 3.24: (A) Electric field levels [V/m] for PCI5 cell; (B) Power levels [dBm].

50p	95p	max	Mean	STD
0	0.011	0.25	0.003	0.012

Table 3.16: Statistical analysis of numerical results in PCI5 scenario. All values are given in V/m.

PCI6 results

Finally, results of simulations for PCI6 are shown in Fig. 3.25 both in terms of electric field [V/m] (A) and power levels [dBm] (B). As in previous cases, the electric field levels are far below exposure limits for population, and this outcome is again confirmed by the statistical analysis reported in Table 3.17.

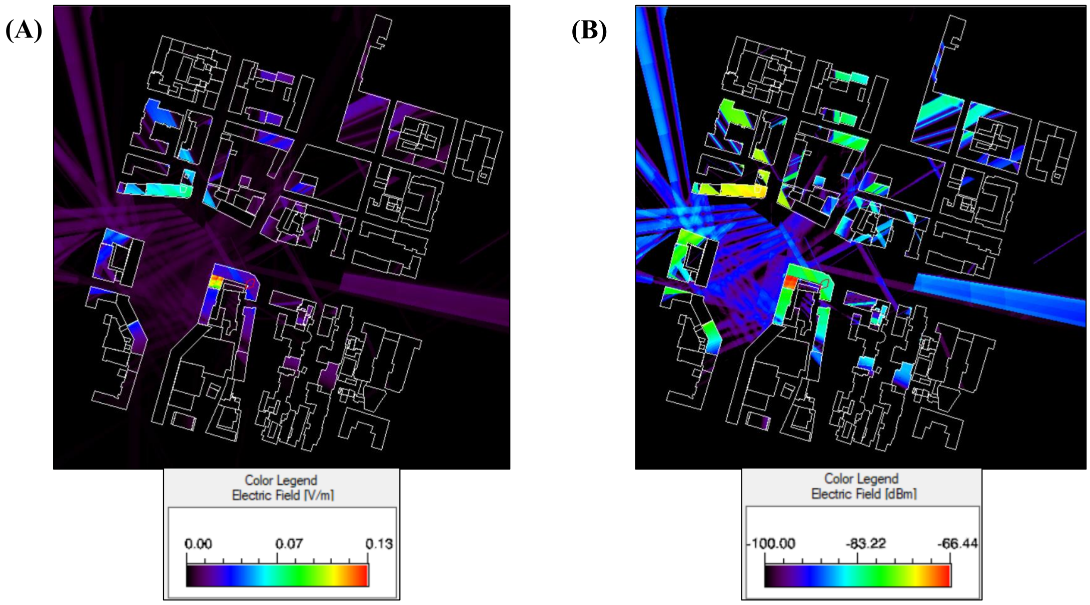

Figure 3.25: (A) Electric field levels [V/m] for PCI6 cell; (B) Power levels [dBm].

50p	95p	max	Mean	STD
0	0.01	0.13	0.0022	0.066

Table 3.17: Statistical analysis of numerical results in PCI6 scenario. All values are given in V/m.

3.3.2 Hospital Scenario

The same hospital scenario presented in section 3.2.3 and visualized in Fig. 3.16 is considered for the following analysis [181]. In this case, a 5G non-public network operating at 27 GHz is assumed to serve the area. Indeed, as previously discussed, moving to higher frequencies leads to an increase in the signal attenuation, but in the same time, the signal is present over a larger bandwidth, allowing the transmission of a greater amount of data with higher rate. In light of this, the FR2 band is particularly suitable for the installation of 5G non-public network in small areas, like hospitals, in which an optimal quality of network service is necessary. The two configurations E2 and E10 are considered for the small cell, with the antenna envelope diagram shown in Fig. 3.22. The same scenario parameters are set for simulations (see Table 3.14). Ray launching analyses are carried out considering diffraction phenomena and rays propagation with a threshold of -135 dBm.

E10 Class

Results of ray-based analysis for E10 Class configuration are shown in Fig. 3.26 in terms of electric field distribution in V/m (A) and dBmV/m (B). As can be seen, spatial distribution of the field is completely different from the 3.7 GHz case (Fig. 3.18), since with the envelope diagram of a 27 GHz antenna, the different lobes of the pattern contribute significantly to the rays propagation. Moreover, the electric field levels are much lower with respect to the FR1 band, due to the higher frequencies involved. More in detail, statistical analysis reported in Table 3.19, shows that 95p and max values are far below exposure limits for population and medical devices compatibility. Moreover, these values are much lower with respect to the 3.7 GHz scenario, as expected.

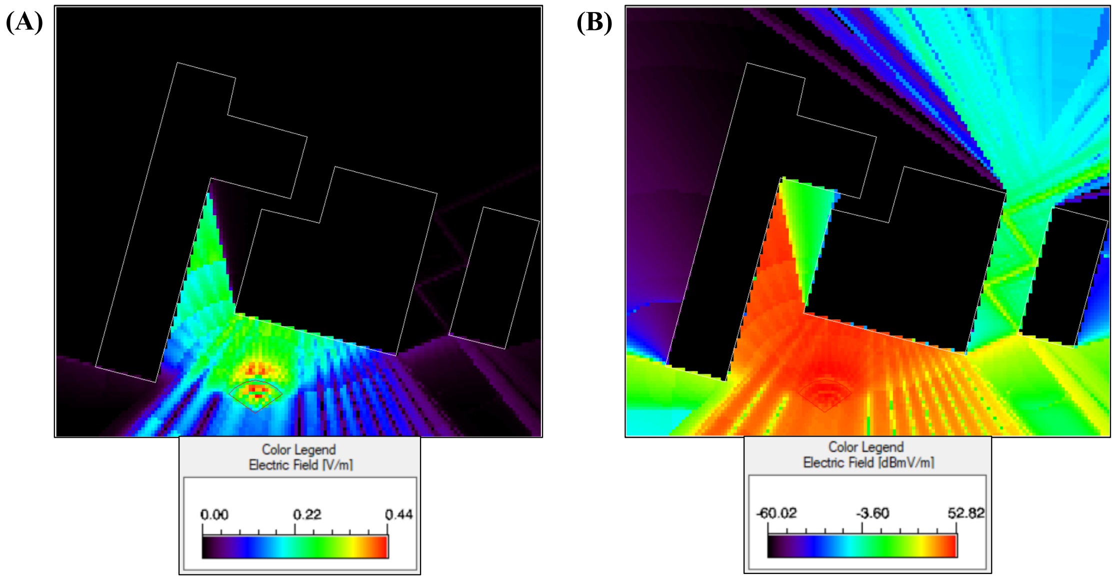

Figure 3.26: Electric field levels for E10 small cell class at 27 GHz; (A) V/m; (B) dBmV/m.

50p	95p	max	Mean	STD
0	0.21	0.44	0.03	0.07

Table 3.18: Statistical analysis of numerical results E10 small cell class at 27 GHz in the hospital scenario. All values are given in V/m.

E2 Cell

Results for E2 Cell configuration are reported in Fig. 3.27. As in previous case, the electric field levels are slightly higher than E10 scenario, but still under safe limits. This is again confirmed by the statistical analysis in Table 3.19.

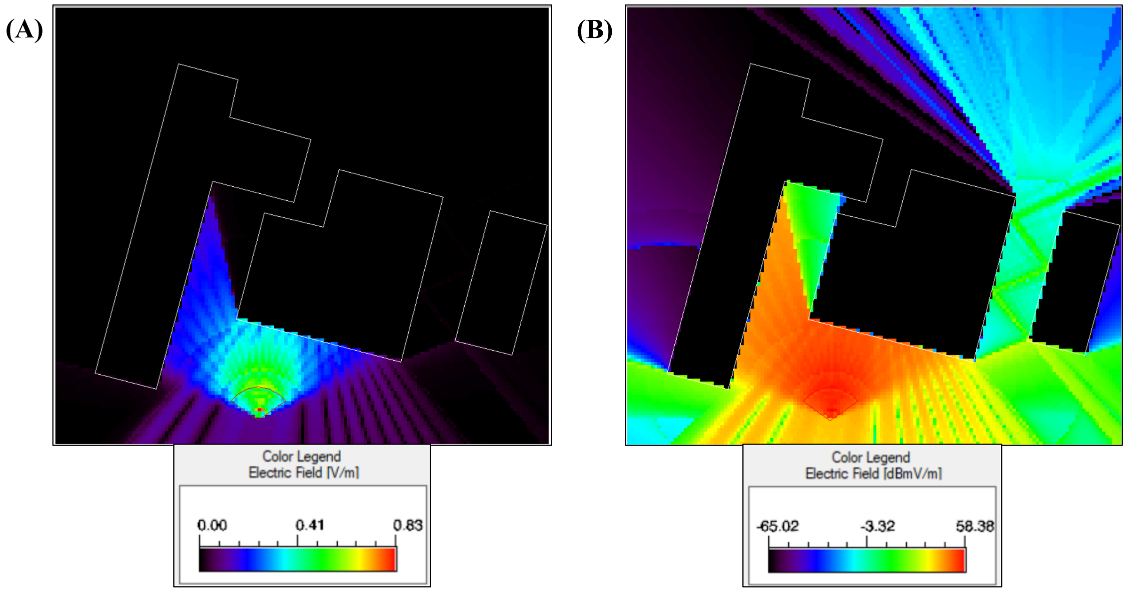

Figure 3.27: Electric field levels for E2 small cell class at 27 GHz; (A) V/m; (B) dBmV/m.

50p	95p	max	Mean	STD
0	0.22	0.83	0.03	0.09

Table 3.19: Statistical analysis of numerical results E2 small cell class at 27 GHz in the hospital scenario. All values are given in V/m.

3.4 Concluding Remarks

In this Chapter, assessment of the population exposure, as well as radio coverage, to 5G antennas has been carried out both in the FR1 and in the FR2 band. The study explored several scenarios, covering both standard urban areas and sensitive environments such as hospitals. The propagation of electromagnetic fields has been accurately modeled employing a ray-based algorithm, whose underlying principles are comprehensively described from both physical and numerical implementation perspectives. Results show that, for all the considered scenarios, the electric field levels remain below the exposure limits set by the ICNIRP guidelines and current Italian regulations. In the hospital scenario, compliance is also ensured when considering the electromagnetic compatibility limits for general medical electrical equipment according to IEC standards. This outcome holds for both FR1 and FR2 bands, with notably lower field levels observed for FR2 antennas, in line with all the theoretical observations previously discussed. Overall, analyses carried out in this Chapter demonstrate that ray-based algorithms can be a flexible method to assess compliance with exposure limits for 5G applications, allowing to compute the spatial distribution of the electromagnetic field in many types of environments. Indeed, simulations were performed considering different scenarios in terms of size, complexity and topology. Furthermore, electromagnetic predictions identified some potentially critical areas exhibiting electric field levels close to safety limits, while highlighting, at the same time, regions with limited radio coverage. Understanding this aspect is fundamental for the safe and efficient planning of 5G networks, particularly in the FR2 band, where telecom operators face the challenge of high signal attenuation.

Chapter 4

Experimental and Numerical Analysis of Ray-Based Algorithms for the Assessment of Human Exposure

In this Chapter numerical and experimental analyses of the presented results about ray launching simulations are carried out. Numerical investigation is performed with the collaboration of three independent laboratories, employing four different more ray-based tools. To compare their algorithms, a systematic workflow is proposed in this thesis that takes into consideration all the relevant metrics for a reliable assessment in 5G scenarios. The method is then applied to verify algorithm results in the different scenarios evaluated in the previous Chapter. In addition to this, an experimental assessment in the FR1 band is carried out, considering a measurement campaign presented in literature. On the other hand, an extensive measurement campaign is performed for the analysis in the FR2 band with the contribution of the antenna operator and is here introduced. Results will demonstrate that, despite some discrepancies, the ray launching algorithm is accurate enough for both exposure and coverage assessment in 5G scenarios.

4.1 Assessment Workflow

As discussed in previous chapters, when different ray-based algorithms are employed in the analysis of a particular scenario, a direct comparison of their results is not straightforward. Indeed, the computation rationale underlying each specific tool leads to several outcomes that may require a complex interpretation for their assessment. Since with the advent of new 5G technologies, carrying out a measurement campaign has grown increasingly complex due to the lack of definite standards and the challenges in these type of measurements due to the variability of 5G signals, assessment of ray algorithm results with the help of a numerical comparison is becoming a promising practice. Moreover, several ray-based tools have been introduced together with 5G systems, so these reasons reinforce the need to define a systematic framework for comparing their results. Thus, in this section, an assessment workflow for ray-based tool comparison is proposed. A schematic overview of the method is reported in Fig. 4.1 [182] and can be summarized as follows:

- First, a common scenario should be identified in terms of coordinates of the buildings and transmitting BS position. Simulate on a common scenario means map of the same dimensions and use of the same technical parameters for the transmittig BS (antenna diagram, BS height and position, transmitted power, pointing, downtilt) and for the receiver. Simulations should be carried out at 1.5 m from the ground following CEI 211-7 [183] indications; the map size may vary depending on the scenario considered. Particular care is needed in selecting its size since, as will be demonstrated in the following sections, it should be slightly larger than the area of actual interest to avoid the loss of reflections or diffraction contributions from objects placed at the edges. Indeed, differences between measurements and simulations can arise when contributions from buildings near boundaries are neglected.

- As a second step, the envelope diagram of the 5G BS should be considered, which in most cases for 5G systems is the only information available about the antenna and, as previously discussed, represents the worst case in terms of human exposure. Moreover, the envelope diagram is suitable for the comparison with *on-site* measurements performed on control signals, improving their repeatability as suggested by the standards [56].

- When possible, simulations should be performed choosing the same pixel dimensions. This will simplify comparisons among tool' results. Otherwise, for tools in which it is possible only to compute the field values at specific points in space, a direct comparison should be made in the same locations.

Finally, the following metrics are proposed for the comparison of the results:

- Electric field/Power Density distribution: fundamental both for coverage evaluation, for setting optimized antenna parameters and for the analysis of the impact of different environmental factors on radio signal propagation.
- Percentiles and cumulative distribution function (CDF) analysis: helpful to assess the compliance with exposure limits and the quality of the service in the area of interest. Moreover, these outcomes can be directly compared with ICNIRP reference levels, in accordance with standard recommendations [56].
- Electric field/Power Density levels in selected points: valuable support in defining the set of locations to perform real exposure measurements and to have a quantitative evaluation of signal attenuation due to possible environmental obstacles. Moreover, for the specificity of 5G systems, punctual evaluation can lead to assess also *on-site* measurement techniques and to calibrate 5G signal measurement equipments.

More in detail, regarding the points selected for direct comparison, the selection criterion is based on the following aspects:

- Outdoor scenarios;
- Position in Line Of Sight (LOS) with the BS;
- Critical areas (e.g. areas located at the corner of buildings) or areas which require particular attention due to their characteristics (e.g. points near metallic structures);
- Points where *on-site* electric field measurement activities were also carried out (if present).

The agreement between tools is considered satisfying if the differences are in the order of 15-20% [68], since this error can occur during measurements due to the presence of random environmental contributions. All these proposed metrics are suitable for the assessment in 5G scenarios, since the variables taken into consideration are directly comparable with exposure limits and *on-site* measurements. In the following sections, the presented workflow will be applied to the different scenarios simulated in Chapter 3, proving to be a valuable support for ray-based tools validation.

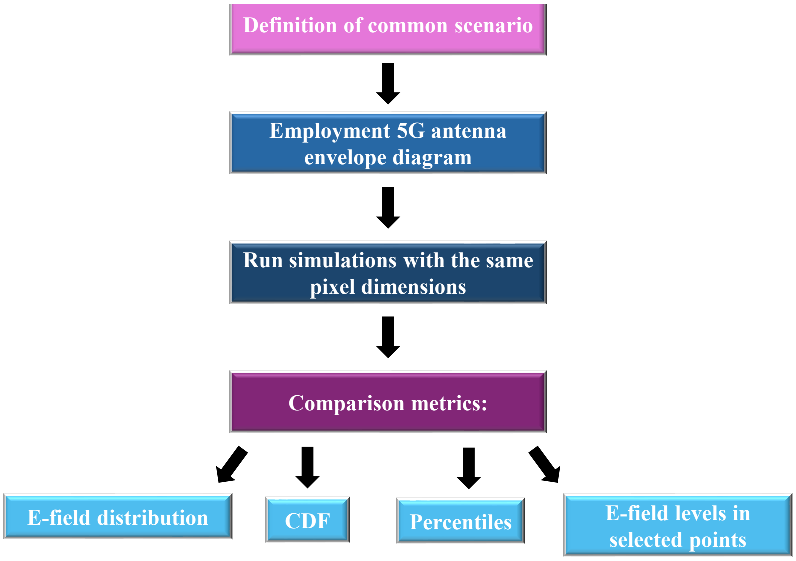

Figure 4.1: Proposed systematic workflow for ray tracing tools assessment.

4.2 Numerical Analysis in the FR1 band

Scenarios in the FR1 band presented in previous chapter are investigated in this section from the numerical point of view. More in detail, the proposed assessment workflow is applied to all oncoming analysis, involving one more ray-based tools independently used by another laboratory: *Armonica*. Some details about this tools are provided:

Armonica is a proprietary ray tracing tool of the Ugo Bordoni Foundation, an Italian institution highly specialized in telecommunication systems and reference organization on behalf of the Italian Parliament, for the assessment of electromagnetic field levels in the environment. The tool is developed in cooperation with the University of Bologna to support ARPA (Italian Regional Environment Protection Agency) activity in electromagnetic field monitoring. This tool comprises a graphic interface for data input/output and results visualization and electromagnetic computation modules. The graphic interface, developed in Windows, comprises various windows and menus that allow to input data to characterize the transmission site (position, antenna pattern, power, tilt, etc.) and to choose the computation to be performed (minimum volume of respect related to exposure levels or field levels). Results can be obtained either as data in a spreadsheet or in graphic form on the video interface. Electromagnetic computation may be carried out either with a simple free space formula or with a 3D ray-tracing algorithm, following as for *Exact* the rules of geometric optics, the theory of diffraction and scattering. The ray-tracing modules allow precise evaluations both in near field and in far field conditions. This ray-tracing algorithm was validated in the COST 231 Action [184], by comparing it both with other tools developed by various other participating institutions and measurements carried out in Munich, Germany. The performed analysis confirmed that the tool is accurate enough to perform reliable estimates of E-field levels up to the 28 GHz frequency band.

4.2.1 Suburban Scenario Analysis

Results obtained in the suburban scenario presented in Fig. 3.7, are here compared with simulations carried out by means of *Armonica* at FUB laboratory (Bologna subdivision). As already mentioned, the proposed workflow approach has been applied for the analysis. Thus, following the different steps presented in Fig. 4.1, the same scenario is set for simulations, considering coordinates of buildings, BS position, antenna diagram, height, power and all parameters reported in Table 3.3. Moreover, the same envelope diagram of 3.7 GHz NR antenna presented in Fig. 3.13 is used to perform computational analyses. The same pixel dimension is chosen for the comparison, equal to 1 m x 1 m and field values are evaluated at 1.5 meters from the ground, as previously discussed. The principle difference arisen between the two tools is in the management of indoor propagation. Indeed, *Armonica* is able to perform a ray tracing analysis considering the indoor propagation, while in *Exact* only an attenuation factor can be accounted from outdoor to indoor propagation, as discussed in the previous chapter, and the field can be computed at different heights inside the building without following the ray tracing rules. For this reason, some strategies are implemented to perform a fair comparison between tool results. In any case, the results of indoor propagation in *Armonica* are reported since they can provide important information on the overall field distribution in the scenario.

Macro Cell Scenario Analysis

Electric field distributions obtained with *Armonica* tool in the macro cell configuration are reported in Fig. 4.2. More in detail, in Fig. 4.2 (A) results computed with the indoor contributions are shown, while Fig. 4.2 (B) illustrates electric field values neglecting these contributions, assuming building materials as metallic to perform simulations in the almost same *Exact* operating conditions. The reported legend for the electric field levels [V/m] is the same for both situations and is fixed inside the tool. As can be seen, despite a different visualization, the same electric field trend is recognizable compared to that of *Exact*, presented in Fig. 3.11, mainly in terms of spatial distribution. However, this information is not sufficient for an accurate comparison, and for this reason, following the proposed systematic workflow, other metrics are considered.

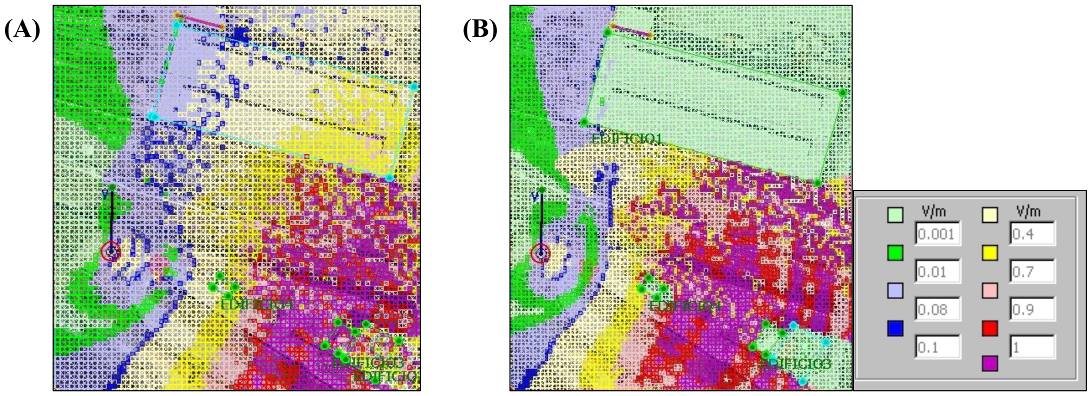

Figure 4.2: Ray tracing results of *Armonica* in terms of electric field levels for macro cell scenario; simulations are carried out (A) with indoor contributions and (B) without indoor contribution; the electric field [V/m] legend is the same for (A) and (B). *© 2026 IEEE*

Therefore, analysis in terms of percentiles is carried out. To solve the difference between tools in the indoor propagation management, percentiles are compared in these two configurations:

- *Exact*: neglecting the electric field values that fall within the building perimeter since as explained in previous chapter, those values are referred to the field computed at 1.5 meter height from the roof.
- *Armonica*: assuming building material as metallic, with the final configuration shown in Fig. 4.2 (B).

To prove the importance of these assumptions, the percentiles obtained with the default settings of the tools are also reported. These configurations will be referred as "buildings" and "no buildings" for sake of simplicity. Moreover, for a more accurate comparison, beyond the 50p and 95p percentiles, also 60p, 70p, 80p,

Percentile	**Armonica (buildings)**	**Exact (buildings)**	**Armonica (no buildings)**	**Exact (no buildings)**
50p	0.21	0.68	0.49	0.43
60p	0.35	1.00	0.80	0.93
70p	0.55	1.21	0.90	1.22
80p	0.81	1.34	0.99	1.34
90p	1.01	1.49	1.12	1.49
95p	1.11	1.56	1.35	1.55
99p	1.28	1.89	1.77	1.64
max	1.98	2.49	2.25	2.20

Table 4.1: Statistical analysis of the electric field levels for *Armonica* and *Exact* in macro cell scenario. All values are in V/m.

90p, 99p and max value of the electric field are considered. Results are shown in Table 4.1.

As can be seen, putting tools in the same operating condition is essential. Indeed, by looking at percentiles of *Armonica* and *Exact* with buildings, differences between results are much higher with respect to the configuration without considering indoor contributions. This final configuration, that is the optimal one to verify *Exact* results, leads to differences between the tool percentiles of about 0.06 V/m for the 50p, 0.2 V/m for the 95p and 0.05 V/m for the max value, demonstrating a very good agreement between the results. In addition to this, also the empirical CDFs (E-CDFs) trends are shown with and without buildings in Fig. 4.3 (A) and in Fig. 4.3 (B) respectively. By comparing the two configurations, a noticeable improvement in the E-CDFs trends is found neglecting indoor contributions. Moreover, the maximum values obtained with the two tools are much more in accordance and this is a fundamental aspect for the assessment of exposure levels.

Finally, a set of locations has been selected for the punctual comparison, considering 10 points distributed in different positions around the BS [185]. More in detail, each point is characterized by its angular position with respect to the north, considering the origin in the BS position, and by its distance from the BS. A representation of the point distribution in space is shown in Fig. 4.4, while corresponding coordinates are reported in Table 4.2.

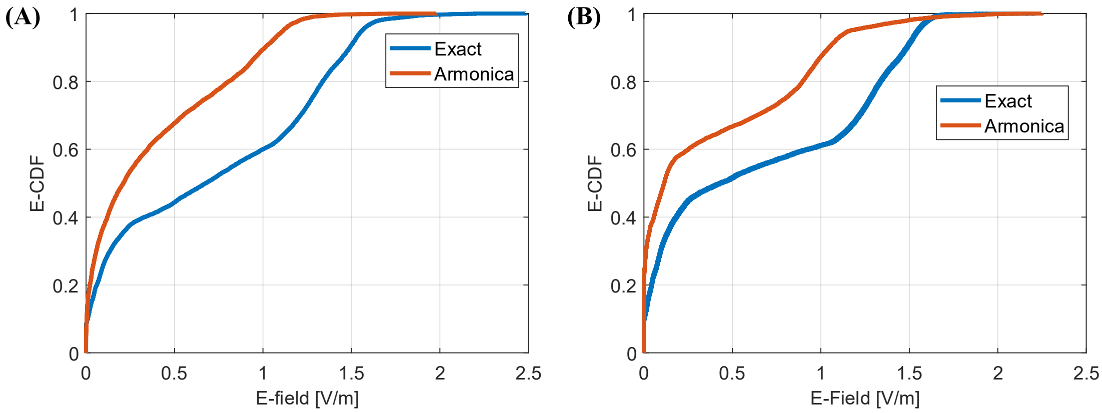

Figure 4.3: E-CDFs computed for the macro cell scenario (A) with buildings and (B) without buildings.

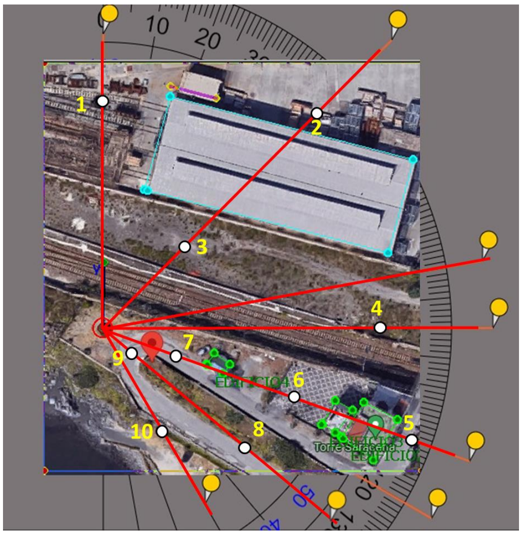

Figure 4.4: Spatial distribution of the selected points for punctual analysis with respect to the BS; the distances are not shown in scale. © *2026 IEEE*

Point N.	Radial Angle [°]	Distance [m]
1	0	60
2	45	80
3	45	30
4	90	70
5	110	83
6	110	50
7	110	20
8	130	47
9	130	10
10	150	30

Table 4.2: Coordinates of selected points in suburban scenario. *© 2026 IEEE*

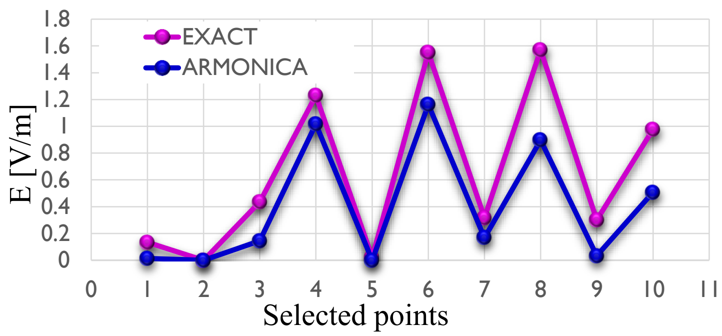

Figure 4.5: Comparison between the electric field levels [V/m] in the selected points for micro cellular scenario.

As can be seen, good agreement is found in the electric field trends and in the specific electric field values. Differences can be noted in some points; this aspect may be attributable to the fact that, for the purposes of this analysis (and for achievement of greater alignment between tools), simulations with *Armonica* have been carried out considering buildings made of metal to eliminate the indoor contribution, while *Exact* considers buildings with a relative permittivity typical of residential areas. Despite these differences, the results are comparable.

Small Cell Scenario Analysis

On the other hand, results obtained with *Armonica* in the case of small cell configuration are shown in Fig. 4.6 and, as in the previous case, electric field levels are reported both with indoor contributions 4.6 (A) and without indoor contributions (B), following the same rationale of macro cell scenario. In this case, the comparison of electric field distributions of *Armonica* and *Exact* is not straightforward considering only their default outputs. An easier comparison can be carried out by looking at Fig. 4.6 (B) and Fig. 3.11 (A), since due to the antenna altitude the electric field distribution at locations corresponding to buildings is not visible in *Exact*. However, as for macro cell configuration, this information is not sufficient to verify tool's results, and for this reason, the statistical analysis on electric field levels, considering both E-CDFs and percentiles is carried out.

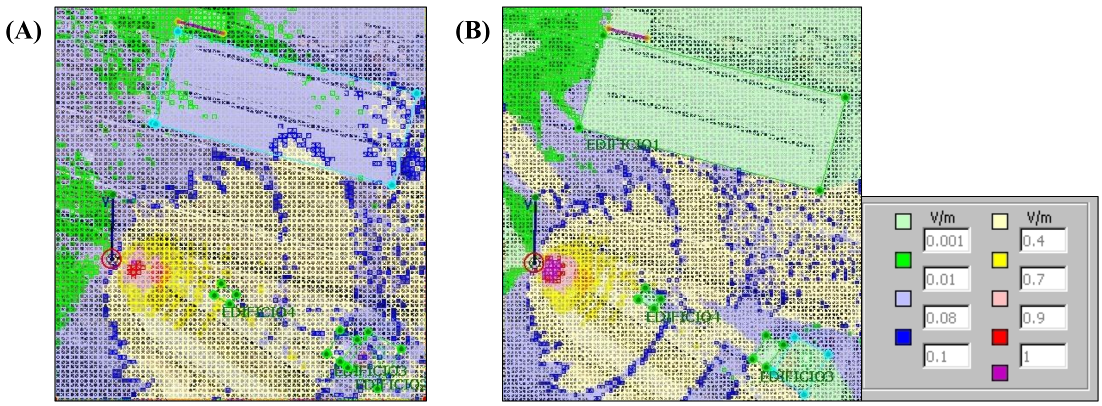

Figure 4.6: Ray tracing results of *Armonica* in terms of electric field levels for small cell scenario; simulations are carried out (A) with indoor contributions and (B) without indoor contribution. The electric field [V/m] legend is the same for (A) and (B). *© 2026 IEEE*

As can be seen from Table 4.3, again neglecting indoor contributions is a fundamental step for tools comparison. Indeed, differences became much lower in this configuration for higher percentiles, with discrepancies of 0.05 V/m for the 50p, 0.09 V/m for the 95p and 0.37 V/m for the max values. To confirm this, also empirical CDFs trends are shown in Fig. 4.7 for the case studies with buildings (A) and without buildings (B). As in the previous case, neglecting indoor contribution leads to a better agreement in the higher electric field levels, and this is a fundamental aspect for a reliable exposure assessment. Finally, the punctual comparison has been carried out in the same locations reported in Table 4.2. Results of the comparison

Percentile	**Armonica (buildings)**	**Exact (buildings)**	**Armonica (no buildings)**	**Exact (no buildings)**
50p	0.06	0.08	0.11	0.16
60p	0.09	0.17	0.14	0.19
70p	0.13	0.20	0.17	0.23
80p	0.20	0.26	0.21	0.28
90p	0.28	0.35	0.28	0.38
95p	0.37	0.45	0.39	0.48
99p	0.66	0.84	0.75	0.89
max	1.03	1.79	1.42	1.79

Table 4.3: Statistical analysis of the electric field levels for *Armonica* and *Exact* in small cell scenario. All values are in V/m.

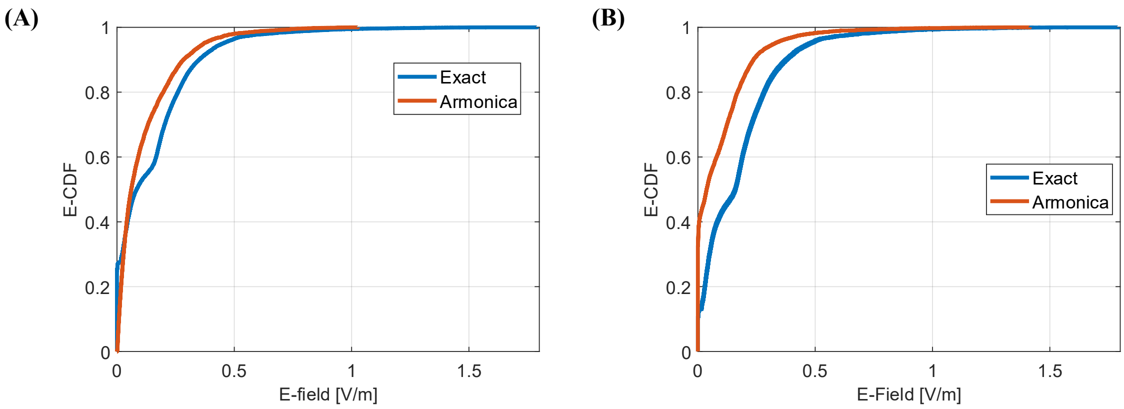

Figure 4.7: E-CDFs computed for the small cell scenario (A) with buildings and (B) without buildings.

are shown in Fig. 4.8.

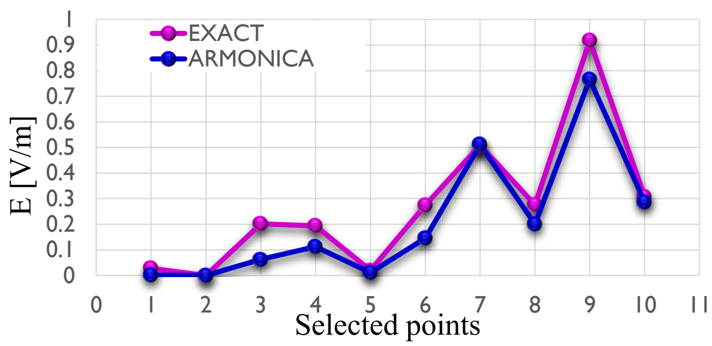

Figure 4.8: Comparison between the electric field levels [V/m] in the selected points for small cellular scenario.

In this case, with respect to the macro cell scenario, discrepancies are slightly lower and results are still in good agreement in terms of electric field trends and punctual values.

4.2.2 Hospital Scenario Analysis

In this section, results obtained in the hospital scenario "Ospedale Maggiore di Parma" (see Fig. 3.16) are analysed with respect to the outcomes of *Armonica* tool. More in detail, since *Armonica* is able to perform indoor simulations, additionally, an optimization analysis for the antenna position is carried out. Indeed, as already discussed, this aspect should be carefully considered, especially in critical environments such as hospitals, to provide optimal service quality and to ensure, at the same time, compliance with population exposure limits and medical device compatibility requirements. For this reason, results obtained by *Armonica* tool with the same antenna described in Fig. 3.8 and simulation parameters of Table 3.11, are reported considering indoor ray tracing contributions both for E2 (Fig. 4.9 (A)) and E10 (Fig. 4.9 (B)) configurations. After several analysis carried out at FUB laboratory, the optimal antenna position for E2 small cell configuration was identified with the BS located at the coordinates reported in Table 3.11. In this position, a coverage of 1 mV/m in the selected scenario is ensured, maintaining the electric field levels in both indoor and outdoor environments below the exposure limits for the public and below the limits for interferences with medical devices. As matter of fact, test simulations performed with a non-optimized base station position showed as result a sub-optimal coverage and two buildings not sufficiently served by the BS. An example of coverage in the case of a non-optimized antenna position compared to the optimized configuration is shown in Fig. 4.10 (A) and (B), respectively.

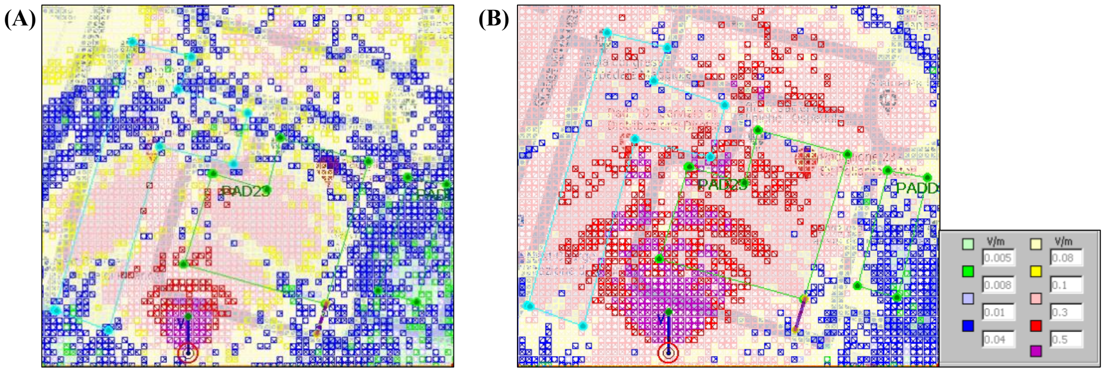

Figure 4.9: *Armonica* electric field levels [V/m] in hospital scenario for (A) E2 small cell configuration and (B) E10 small cell configuration.

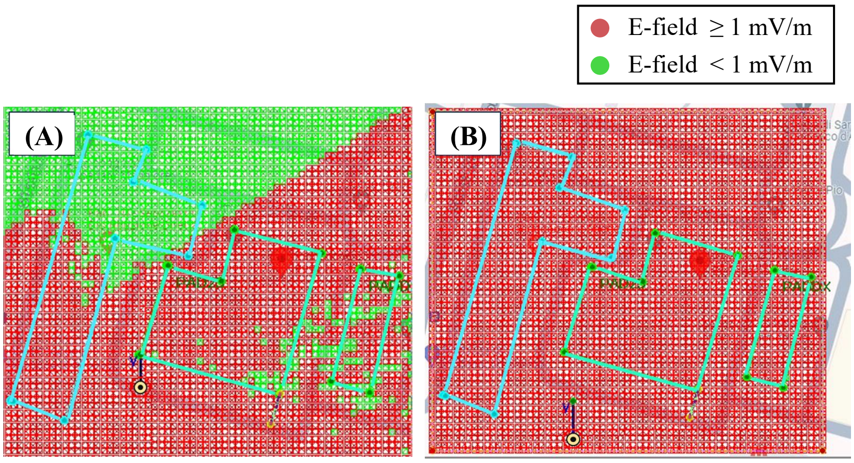

Figure 4.10: Coverage of 1 mV/m for non optimized (A) and optimized (B) antenna position; in green and red colors field values below and greater than 1mV/m are shown.

For this reason, *Exact* assessment is carried out considering the optimized configuration of E2 small cell. As previously discussed, for a better comparison between tool results, *Armonica* simulations are carried out assuming building materials as metallic and same simulation parameters reported in Table 3.11. Results are shown in Fig. 4.11, and it can be seen that a good agreement is found in terms of the electric field distribution with respect to *Exact* outcomes presented in Fig. 3.27 (A). Moreover, E-CDFs are reported in Fig. 4.12 and demonstrate an almost perfect agreement between tool results at all percentiles. That's why specific values of percentiles and punctual comparison are not reported.

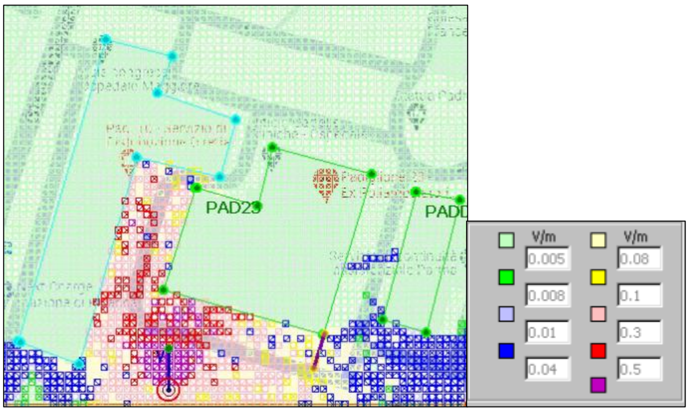

Figure 4.11: Electric field levels [V/m] computed by *Armonica* in hospital scenario for E2 small cell configuration without considering indoor contributions.

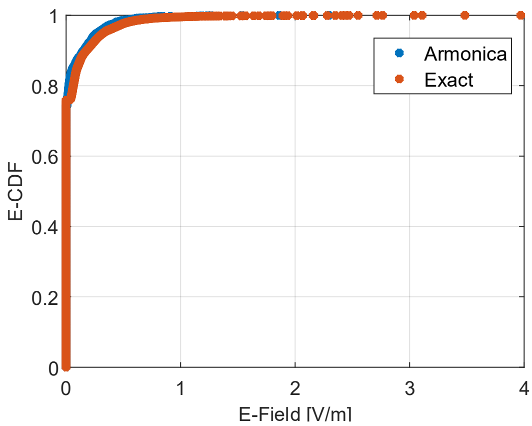

Figure 4.12: E-CDFs for *Armonica* and *Exact* in hospital scenario in FR1 band without building contributions.

4.3 Experimental Analysis in the FR1 band

As regarding the Rome scenario described in section 3.2.2 and visualized in Fig. 4.8, an experimental analysis is presented in this section [186]. More in detail, this scenario has been selected since a measurement campaign has been carried out in 2020

[68] near the BS antenna with the traffic diagram shown in Fig. 3.13. All detailed information about antenna characteristics and measurements have been provided by Vodafone, that is the antenna operator, and by the University of Cassino and Southern Lazio that collects the experimental results. In addition to this, a further ray tracing algorithm is considered for the assessment beyond *Exact* and *Armonica*, with simulations carried out independently by the FUB laboratory (Rome subdivision). More in detail, *Matlab 5G Toolbox* is employed, since it is a commercial ray tracing tool widely used for simulations in 5G scenarios [187], [188], [189]. Thus, a brief description of the tool is provided.

Matlab 5G Toolbox is a ray tracing tool to configure, simulate, measure and analyze end-to-end 5G NR communication links. In particular, this tool can import a real built-up map by an Open Street Map file and use these 3D environments to simulate a real scenario using a ray tracing propagation model, computing multiple propagation paths. Path loss and phase shift are calculated either by SBR method or the image method. In particular, for each ray, electromagnetic analysis is performed considering horizontal and vertical polarizations of the signal along the propagation path, including free-space loss, reflection losses, and diffraction losses (Fresnel equation, uniform theory of diffraction, geometric angle, and complex permittivity of materials). These capabilities support research and development in wireless communication, offering a detailed approach to studying interference, coverage and network performance in diverse deployment scenarios.

Since now three different ray tracing algorithms are involved, before proceeding with further analysis, their main features are summarized in Table. 4.4. As can be seen, due to the specific features of the tools, the indoor propagation management is different. Indeed, for *Exact* and *Armonica* this point has already been discussed in the previous section, while for *Matlab* the indoor propagation is not considered in the tool while outdoor simulations are performed. Moreover, the tools work with different stopping criteria: for *Exact*, this has been explained in Chapter 3, for *Matlab* it is based on the number of reflections and diffraction set by the user, while for *Armonica*, this information is not provided. Finally, *Exact* and *Armonica* are proprietary tools, mainly used for research purposes, while *Matlab* is a commercial tool.

	Exact	Armonica	Matlab
Ray tracing model	VPL	3D ray tracing	SBR
User-defined stopping criteria	Yes (electric field threshold)	No	Yes (number of reflections/diffractions)
Outdoor to indoor	Partial (near building perimeter)	Yes	No
Type	Academic	Academic	Commercial

Table 4.4: Comparison between ray-based tools main features. *© 2026 IEEE*

4.3.1 Description of the Measurement Campaign

The measurement campaign has been carried out considering different test conditions, but ray-based simulations are compared specifically with the electric field levels measured in the point marked in red and referred as point "A" in Fig. 4.13. In the same picture, antenna position is indicated in green color.

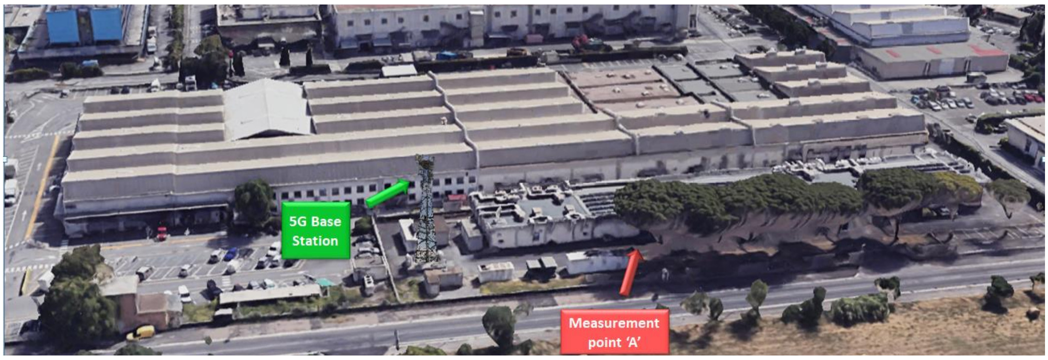

Figure 4.13: Measurement site. The 5G antenna and equipment positions are highlighted in green and red respectively. *© 2026 IEEE*

In this location a customized UE terminal is placed, to perform high-data download. In this way, the BS antenna is forced to transmit continuously at the maximum power. Two different devices have been used to perform selective channel power measurements: a Keysight signal analyzer (MXAN9020A) and a Rohde & Schwarz (FSP30) spectrum analyzer. In Table 4.5 results of the measurement activity are reported with uncertainties at 95p.

Equipment	**Electric Field [V/m]**
Keysight signal analyzer	1.72 ± 0.29
R&S spectrum analyzer	1.89 ± 0.45

Table 4.5: Electric field [V/m] measured in point "A".

4.3.2 Numerical Analysis

The location of the measurement point visualized in the simulation environment is marked in red in Fig. 4.14. As can be seen, it is located in LOS with respect to the BS position and it is approximately 50 meters away from the antenna. Therefore, the contributions of reflection/diffraction from other distant buildings should not be significant in that point. For this reason, it is considered sufficient to model the five buildings present in Fig. 4.14 that are closest to the measurement point. According to the proposed workflow, the same simulation environment is considered for the three tools involved with the same settings reported in Table 3.8. Moreover, for *Matlab* tool, 10 reflections and one single diffraction are considered.

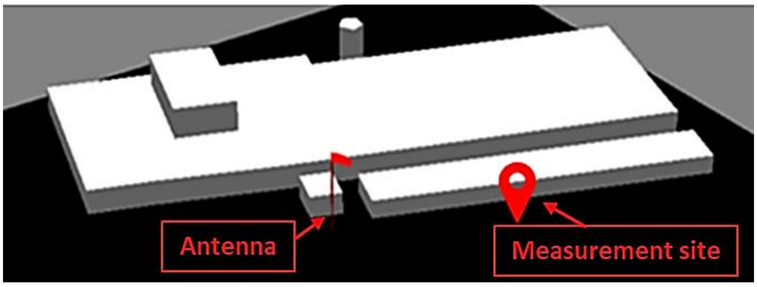

Figure 4.14: Simulated scenario; the 5G antenna and measurement point positions are highlighted. © *2026 IEEE*

Following the first step of the assessment workflow, electric field distribution is computed at 1.5 meter height from the ground for each tool. In addition to *Exact* results shown in Fig. 3.15, field distributions for *Armonica* and *Matlab* are reported in Fig. 4.15 (A) and Fig. 4.15 (B) respectively. As can be seen, in *Armonica* the output is only available in V/m, while in *Matlab* the electric field is shown in dBμV/m, making a direct comparison between these tools not straightforward. However, each of them can be compared with *Exact*. More in detail, *Armonica* electric field distribution can be compared to Fig. 3.15 (A) in which *Exact* output is shown in V/m. By looking at these two representations, it can be observed that a good agreement is found both in terms of field levels and distribution. On the other hand, with *Exact* it is also possible to display the field in dBmV/m, as shown in Fig. 3.15 (B), so comparing this outcome with *Matlab* results, a good agreement is found again in the electric field distribution, even if a direct comparison of field levels cannot be performed due to the different scales.

Therefore, to go deeper into the analysis, the other metrics are considered. First,

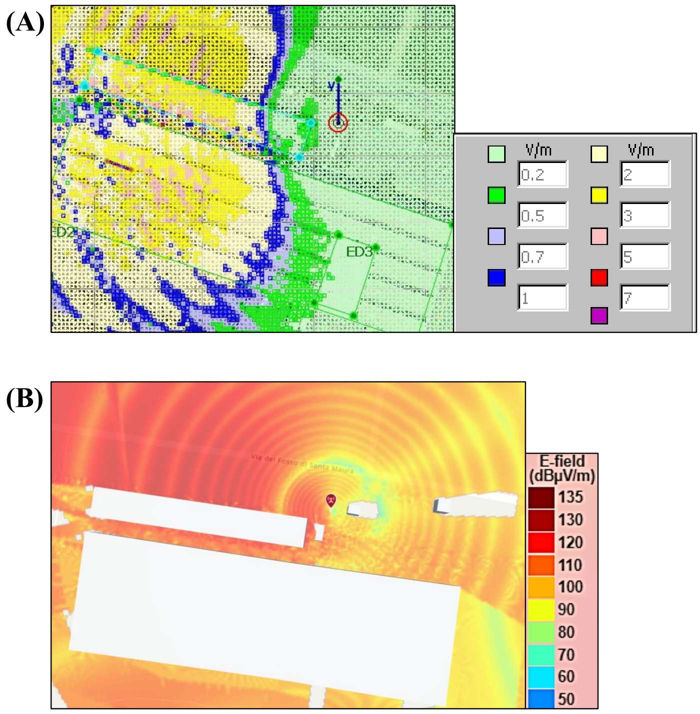

Figure 4.15: Electric field distribution at 1.5 meters height from the ground obtained with *Armonica* (A) and *Matlab* (B) tool. *© 2026 IEEE*

the percentiles are reported in Table 4.7. As can be seen, in this particular scenario tool comparison is not straightforward. The worst case is represented by the configuration of *Exact* results considering the building contributions, since greater discrepancies are found both for lower and higher percentiles. Indeed, neglecting the electric field levels in the location of buildings leads to a better agreement between tool results, since these values, as already discussed, are computed at 1.5 meters from the top of roofs. With this new configuration, *Exact* and *Armonica* results are in very good agreement for higher percentiles. Indeed, the difference is only 0.09 V/m at the 95th percentile and 0.3 V/m for the maximum value. On the other hand, a good agreement is also found for low percentiles (from 50p to 70p) between *Exact* and *Matlab*. This is even more clear by looking at Fig. 4.16, in which E-CDFs are shown for the three tools. As can be seen, from 0p up to 40p *Exact*, *Armonica* and *Matlab* trends are aligned, while from 50p up to 70p the best agreement is found between *Exact* and *Matlab*, and for higher percentiles *Armonica* and *Exact* tend towards the same maximum electric field values.

Finally, the comparison between simulated electric field values in the measurement point is reported in Table 4.7 for the three tools involved.

Percentile	**Exact (with buildings)**	**Exact (without buildings)**	**Armonica**	**Matlab**
50p	0.32	0.16	0.75	0.21
60p	0.98	0.23	1.21	0.31
70p	2.17	0.64	1.65	0.49
80p	2.91	1.91	2.07	0.85
90p	4.48	2.61	2.59	1.26
95p	4.92	2.96	2.87	1.52
99p	5.65	3.26	3.34	2.01
max	6.35	5.38	5.69	3.85

Table 4.6: Statistical analysis of the electric field levels for *Exact* with and without building contributions, *Armonica* and *Matlab* in Rome scenario. All values are in V/m.

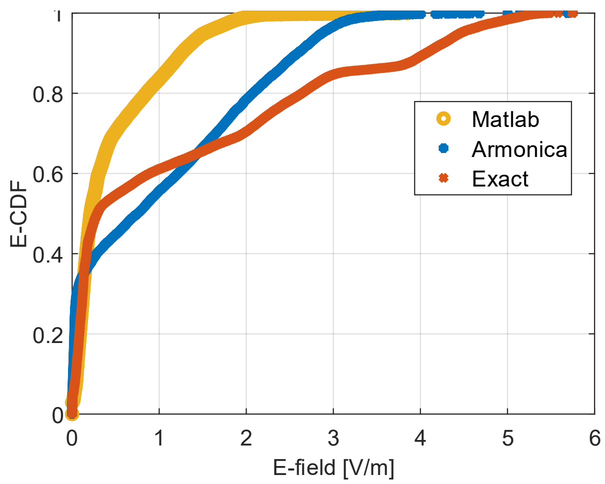

Figure 4.16: E-CDFs for *Armonica*, *Exact* without building contributions and *Matlab*. *© 2026 IEEE*

Ray tracing simulation	**Electric Field [V/m]**
Exact	1.80
Armonica	1.86
Matlab	1.92

Table 4.7: Electric field [V/m] simulated in the measured point "A".

From the data analysis, accordance between the three simulated values emerges, as well as a good agreement, within the limits of the experimental errors, with the measured data. Measurements carried out with the Keysight spectrum analyzer in point "A" provided electric field values ranging between 1.43 and 2.01 V/m, while those carried out with the R&S spectrum analyzer fall within the range 1.44 – 2.34 V/m; the values simulated in the same point "A" with the three selected tools are all included within the two aforementioned ranges. Indeed, the location of point A is suitable for an outdoor comparison, as its position is far from buildings, and so, differently from a comparison on the entire simulation area, unaffected by the differences in indoor scenarios management by the three involved tools.

4.4 Numerical Analysis in the FR2 band

Following the same rationale of the FR1 band, the assessment workflow is applied in the FR2 band to assess *Exact* results in the hospital scenario presented in previous chapter. More in detail, numerical analysis is carried out with the help of FUB laboratory that employs *Armonica* tool, together with an optimization study for the antenna position, essential in healthcare environments. Moreover, a comparison between coverage and exposure in FR1 and FR2 band is discussed.

4.4.1 Hospital Scenario Analysis

Armonica simulations are carried out following the same settings reported in Table 3.11 and used for *Exact* simulations, together with the antenna envelope diagram shown in Fig. 3.22. By exploiting the possibility to simulate indoor propagation in this tool, it was verified that the optimized position found for the FR1 band in E2 small cell configuration (see Table 3.11) is still the optimal one for the antenna at 27 GHz. For this reason, the numerical analysis is carried out considering this optimal configuration. Ray tracing simulations are performed with and without indoor contributions, and are shown in Fig. 4.17 (A) and (B), respectively. As can be seen, comparing this last case study with *Exact* outcomes in Fig. 3.27 a good agreement is found in terms of electric field distribution, but in addition to this, E-CDFs are computed and shown in Fig. 4.18. As in the case of FR1 band simulations, an almost perfect agreement is found for all percentiles.

4.4.2 Hospital Scenario Comparison between FR1 Band and FR2 Band

Since simulations in FR1 and FR2 bands are carried out in the same scenario, with the same antenna position, it is interesting to compare these results both for coverage and exposure assessment. Moreover, the final aim of these simulations is also to investigate the impact of 5G non-public networks in healthcare environments.

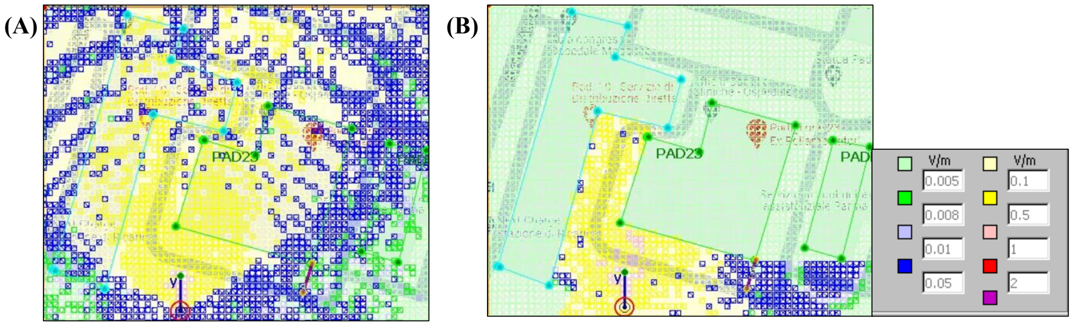

Figure 4.17: Armonica computed electric field levels [V/m] in hospital scenario in the FR2 band (A) with indoor propagation and (B) without indoor propagation.

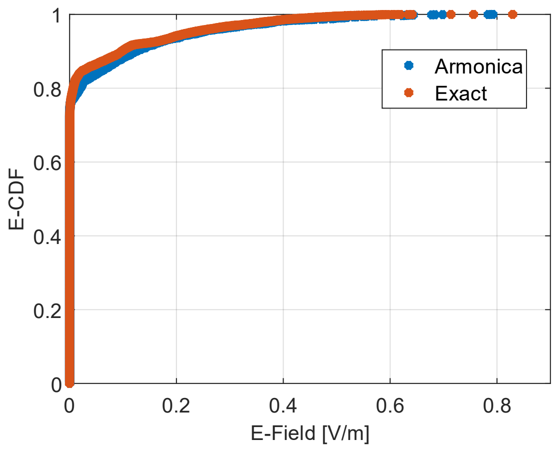

Figure 4.18: E-CDFs for *Armonica* and *Exact* in hospital scenario in FR2 band without building contributions.

Therefore, comparing their performances is useful to identify the most suitable solution for real-world applications. For these reasons, in Fig. 4.19 the obtained E-CDFs in the case of FR1 and FR2 BS are overlapped.

The comparison between these two case studies highlights several key insights:

- Optimized Antenna Position: the selected location for the base station still remains the optimized one also moving to higher frequency, as the selected scenario is relatively small and in line with the coverage area that can be obtained in the mmWave spectrum, typically with cell dimensions of about 100 m x 100 m [190];
- Compliance with Safety Standards: the electric field levels are still under the exposure limits for workers and public [45]. Compliance with the electromag-

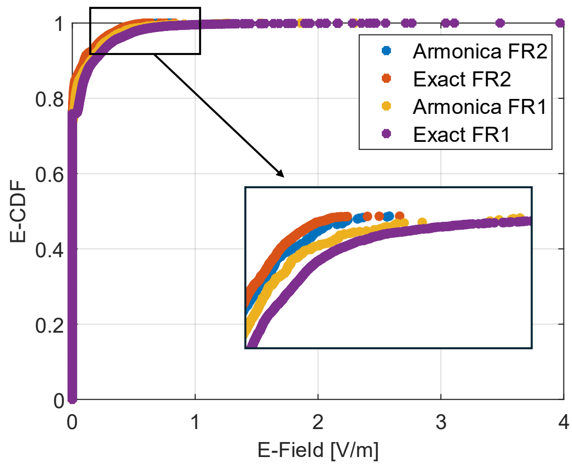

Figure 4.19: Comparison between E-CDFs obtained for FR1 and FR2 band scenario.

netic field marginal value for general electronic medical equipment specified in IEC 60601-1-2 [179] is guaranteed;

- Coverage Challenges at Higher Frequencies: a coverage of 1 mV/m is still guaranteed in the whole scenario, while the 10 mV/m coverage is lower in the FR2 band scenario, as can be expected due to the different propagation characteristics of the frequency bands involved.

Moreover, as can be seen from Fig. 4.19, electric field levels are much lower for the FR2 case with the respect of the FR1, although coverage is equally guaranteed for the 85% of the scenario. Indeed, in Table 4.8 coverage percentages obtained in the two scenarios considered for 1 mV/m and 10 mV/m thresholds are summarized and it is clear that coverage of 1 mV/m is guaranteed both for FR1 and FR2, while considering 10 mV/m coverage, the efficiency of the FR2 system is slightly lower. This is also shown in the FR2 band coverage maps, for 1 mV/m and 10 mV/m, in Fig. 4.20 (A) and (B) respectively. This result was not easily predictable and highlights the need for accurate tools, able to design and optimize 5G non public networks before their deployment.

Frequency band	**10 mV/m coverage**	**1 mV/m coverage**
FR1	93.7%	99.9%
FR2	85.1%	99.5%

Table 4.8: Comparison of coverage percentage in FR1 and FR2 scenarios.

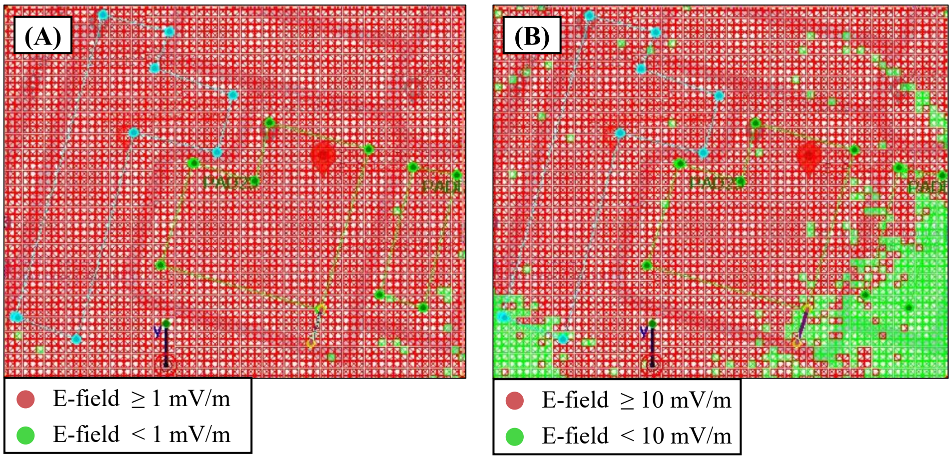

Figure 4.20: FR2 band coverage map in hospital scenario for (A) 1 mV/m coverage and (B) 10 mV/m coverage.

4.5 Experimental Analysis in the FR2 Band

In this section, an experimental analysis in Turin scenario described in chapter 3 is carried out. More in detail, to verify tool results an extensive measurement campaign has been carried out with Vodafone, that is the antenna operator, near a 27 GHz BS. In this case, computational results are compared with a large number of measurement points, together with two more different ray tracing tools to provide a thorough and comprehensive assessment of algorithms results.

4.5.1 Measurement Campaign

A measurement campaign has been conducted in Turin (Italy) in collaboration with Vodafone near a BS in which three 27 GHz massive MIMO antennas are employed, each covering a section of 120° around the site. As previously described, the considered area is subdivided into three cells, identified as PCI4, PCI5 and PCI6 and highlighted with different colored arrows in Fig. 4.21.

Measurements have been performed in walk-testing mode using a Mobile Network Scanner. This approach allowed for the collection of detailed signal data while moving through the environment, providing a realistic insight into network coverage. The measurement set-up is illustrated in Fig. 4.22 and consists of the following components:

Figure 4.21: Measurement campaign scenario in Turin (Italy). BS position and served sectors are shown with colored arrows; PCI4 (yellow), PCI5 (green) and PCI6 (cyan).

- Rohde&Schwarz TSMA6B Mobile Network Scanner [191];
- Rohde&Schwarz TSME30DC ultracompact downconverter for the 24 GHz - 30 GHz input band;
- Omni-directional antenna, 26 GHz - 40 GHz band, with a maximum external diameter of 46 mm;
- Laptop running Rohde&Schwarz Romes software.

For the walking test, the instrument, equipped with a GPS antenna to record geographical information and a battery backup, was placed in a backpack, as shown in Fig. 4.23.

4.5.2 Computational Analysis

Besides *Exact*, three more algorithms are considered for the numerical analysis: *Matlab*, *Aster* and *Sionna*. For *Matlab* a brief description has been provided in previous sections, while *Aster* and *Sionna* are described further below:

Aster is a propagation model developed by Forsk [192]; it is mainly designed for dense urban environments with high resolution geo raster/vector data, but it can

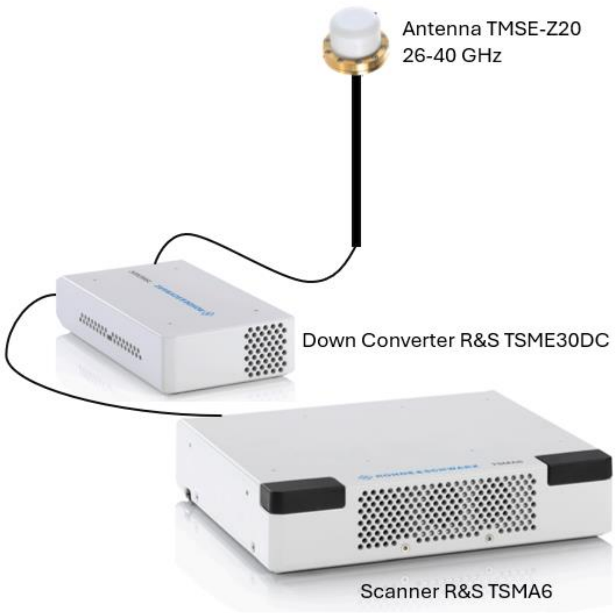

Figure 4.22: Measurement set-up.

Figure 4.23: Measurement set-up for walk-testing. BS and measurement equipments are circled in red.

also be used for urban, suburban and rural areas with various/different geo data. The propagation modeling features are based on two major components:

- vertical diffraction over rooftops based on Walfisch Ikegami model [193] and multiple knife-edge Deygout method [194];
- horizontal diffractions and reflection below rooftops based on ray launching.

The tool is able to simulate 5G network in mmWave scenario within the range 5 GHz to 60 GHz, considering also the vegetation diffraction and through loss, the atmospheric absorption and the rain attenuation. Additionally, the model incorporates automatic calibration features to adjust its parameters based on measurement data collected on site, optimizing its accuracy.

Sionna is an open-source library for link- and system-level simulation that includes a GPU-accelerated ray tracing engine [85]. The ray tracing module is based on path tracing with multiple interactions between the rays and the surrounding 3D environment, allowing for multiple reflections and transmissions at dielectric interfaces. High-resolution 3D scenes, built for example from OpenStreetMap data and modeled in Blender, can be imported and combined with realistic antenna radiation patterns and polarization. *Sionna* operates in the mmWave band and supports directional antenna arrays, enabling the analysis of site-specific propagation effects, coverage, and exposure in complex urban scenarios. Similar to *Matlab*, the *Sionna* functionality is implemented via the SBR method, modeling each propagation path as a cascade of scattering processes occurring along the 3D scene, including specular reflections, refractions, diffractions, and diffuse scattering.

Main characteristics of algorithms involved in the following analysis are summarized in Table 4.9.

Tool	**Type**	**Ray Tracing Model**
Exact	Academic	VPL
Matlab	Commercial-under license	SBR
Aster	Commercial-under license	Walfisch-Ikegami + Knife Edge (Deygout) + horizontal ray launching
Sionna	Open Source	SBR

Table 4.9: Tools main characteristics.

Simulations have been performed considering all the settings reported in Table 3.14. The simulated scenario for *Exact* is the one reported in Fig. 3.21, while for all the other tools it is retrieved directly from OpenStreetMap. This means that some buildings located at the edges of the measurement area are not considered in

Exact scenario, while are modeled in the other tools. This point will be subject of further considerations in computational results. With regard to the input antenna radiation diagram, the radiation pattern envelope reported in Fig. 3.22 was used for each of the three massive MIMO antennas of the BS. Simulations are performed considering diffraction phenomenon for each ray-based tool, while for the number of reflections: 10 are set for *Matlab* and *Sionna*, and 8 for *Aster*. For *Exact* it is not necessary to set this parameter, since, as explained, the number of reflections are automatically generated according to the chosen threshold that in this case is set as -135 dBm, considering the same sensitivity of the measurement equipments. All these settings are summarized in Table 4.10. Moreover, differently from other tools, *Aster* requires a calibration procedure before performing propagation analyses and for this reason a portion of measured data are used as input for the calibration.

Tool	**N. of Interactions**
Exact	1 diffraction; for reflections no limits and procedure stops when for each ray the field level goes below -135 dBm
Matlab	1 diffraction; 10 reflections
Aster	1 diffraction; 8 reflections
Sionna	10 (diffraction + reflections)

Table 4.10: Parameters for ray-based simulations.

4.5.3 Experimental Results

Measurements have been performed following different routes for each cell, as shown in Fig. 4.24) in which the discrete measurement points along the routes are denoted by colored circles according to the specific PCI. The number of measurement points for each cell site were: 4673 for PCI4, 4371 for PCI5 and 5681 for PCI6 respectively, for a total of 14725 points. During measurements, the receiving antenna was kept at a proper distance from the operator's body to mitigate any body induced signal perturbation (see Fig. 4.23). The mobile network scanner recorded the average power of the Resource Elements (REs) of the Secondary Synchronisation Signal (SSS). Due to the lower walking speed compared to the sampling rate of the scanner, some consecutive samples shared identical geographical coordinates. To remove duplicates, SSS-Reference Signal Received Power (SSS-RSRP) values corresponding to the same location were averaged. Moreover, as reported in [191], the measurement uncertainty level of the scanner is lower than 1.5 dB. In addition to this, some studies with a similar setup quantifies the overall error source as 2.39 dB [195]. However, these uncertainties are too small to be visualized into the following figures and for this reason will not be reported.

Received power (P_{RX}) in dBm recorded during the walk are shown in Fig. 4.25 for cells PCI4, PCI5 and PCI6, respectively. For a better understanding of results, a moving average filter with a window size of 20 samples has been applied to raw data. It should be noted that the lower measured power is never below -140 dBm, since this value is close to the sensitivity of the equipments (-135 dBm). Raw measurement data are also shown in terms of E-CDF for a direct comparison with exposure limits in Fig 4.26 (A) [dBm] and (B) [V/m]. For completeness, also percentiles from 50p to max are reported in Table 4.11 [dBm] and Table 4.12 [mV/m]. From data analysis, it emerges that all values for the different PCI considered are far below limits for human exposure and compliance with medical devices, since the maximum level of electric field is measured for PCI4 and is around 0.03 V/m. This is true also if all the PCI are considered together, a situation that can reflect the worst case in which a measurement point falls in the same coordinate of different PCIs. In this case, the maximum reachable value is around 0.8 V/m, still far from all limits taken into consideration.

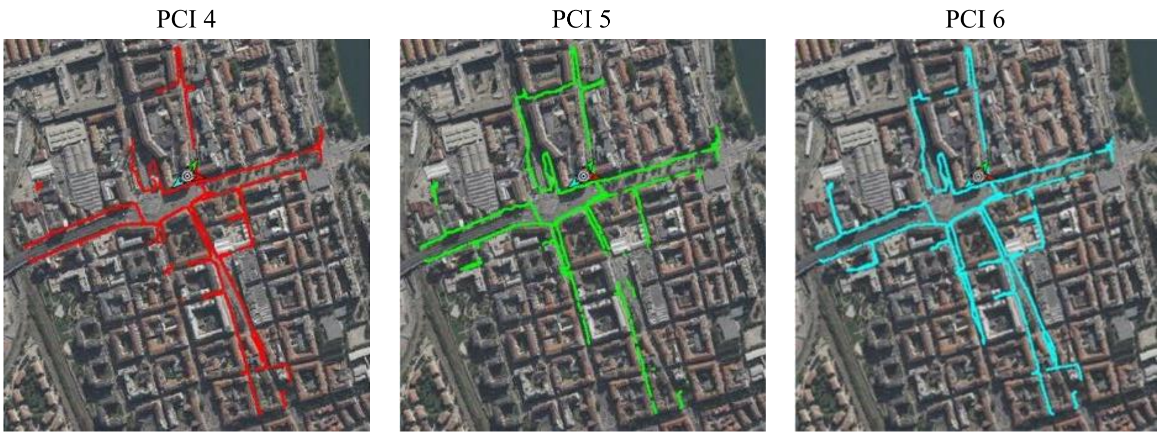

Figure 4.24: Measurement routes for PCI4 (yellow), PCI5 (green) and PCI6 (cyan).

4.5.4 Numerical Results Analysis

For each cell, only measurement points falling within $-65°$ and $+65°$ from the antenna pointing direction are considered for the numerical analysis, since, following suggestions of the antenna operator, this is in practice the area of interest in which coverage is intended for each sector. Moreover, compare numerical and experimental

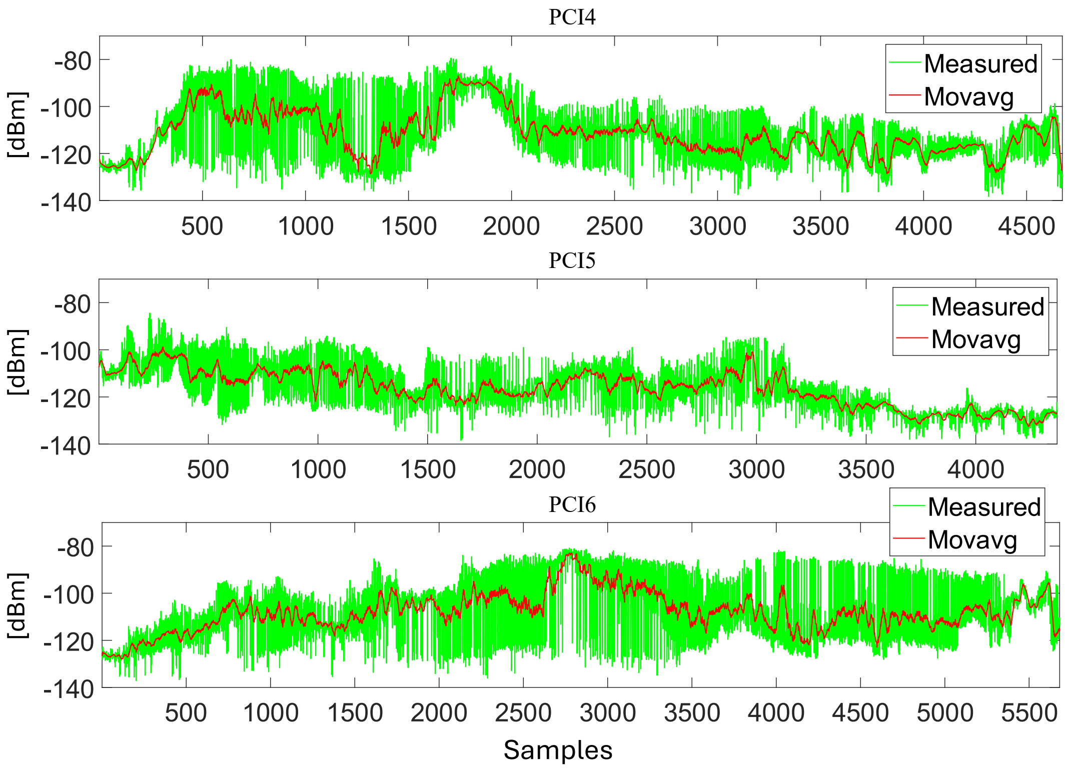

Figure 4.25: Received power [dBm] measured along different routes for PCI4, PCI5 and PCI6. In green raw data are shown, while in red moving average filtered measurements (Movavg) are reported.

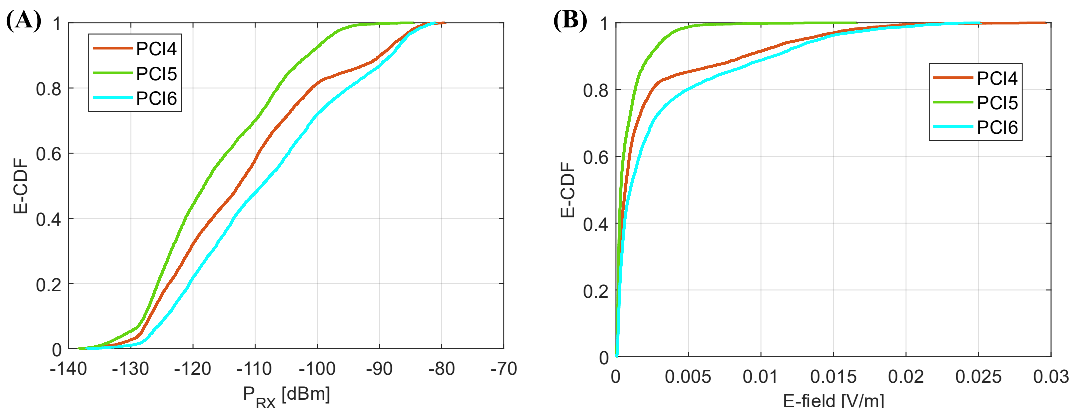

Figure 4.26: E-CDFs of raw measurement data for PCI4, PCI5 and PCI6 in (A) power [dBm] and (B) electric field [V/m].

results on the back side of the antenna envelope diagram may lead to some discrepancies due to minor differences that may exist between the real antenna diagram and the simulated one. On the other hand, considering measurement points in prox-

Percentile	PCI 4	PCI 5	PCI 6
50p	-112.69	-118.23	-108.95
60p	-109.45	-114.64	-104.62
70p	-105.59	-110.01	-100.87
80p	-100.88	-106.42	-95.02
90p	-89.85	-101.48	-88.17
95p	-86.67	-98.56	-85.94
99p	-83.45	-94.53	-82.60
max	-79.41	-84.43	-80.83

Table 4.11: Statistical analysis of raw measured received power data in Turin scenario for PCI4, PCI5 and PCI6. All values are in dBm.

Percentile	PCI 4	PCI 5	PCI 6
50p	0.6	0.3	1.0
60p	0.9	0.5	1.6
70p	1.5	0.9	2.5
80p	2.5	1.3	4.9
90p	8.9	2.3	10.8
95p	12,9	3.3	14.0
99p	18.6	5.2	20.5
max	29.6	16.6	25.2

Table 4.12: Statistical analysis of raw measured electric field data in Turin scenario for PCI4, PCI5 and PCI6. All values are in mV/m.

imity to the direction of the main lobe increases the robustness of the comparison. Therefore, in Fig. 4.27 the effective measurement routes considered for the computational analysis are shown for the different cells. Results are analysed through the computation of CDFs, percentiles and punctual comparison in measurement coordinates. More in detail, as regards this last metric, the intensity spatial maps at the measurement points are also compared.

The CDFs visualization is reported in Fig. 4.28 for PCI4, PCI5 and PCI6. As can be seen, from this first comparison, the overall best agreement between measurements and simulations is obtained with *Aster* tool, but this was expected due to the calibration procedure. Concerning the maximum values, for PCI4 and PCI5 the best fit is obtained with *Exact* tool, while for PCI6 a little overestimation in power levels is found with this algorithm. On the other hand, an underestimation can be seen in lower power levels, and this will be the subject of further analysis below. A similar behavior is detected with *Sionna*, especially for PCI4 and PCI6, while *Matlab* trends are overall close to measured values, except for the PCI4 case.

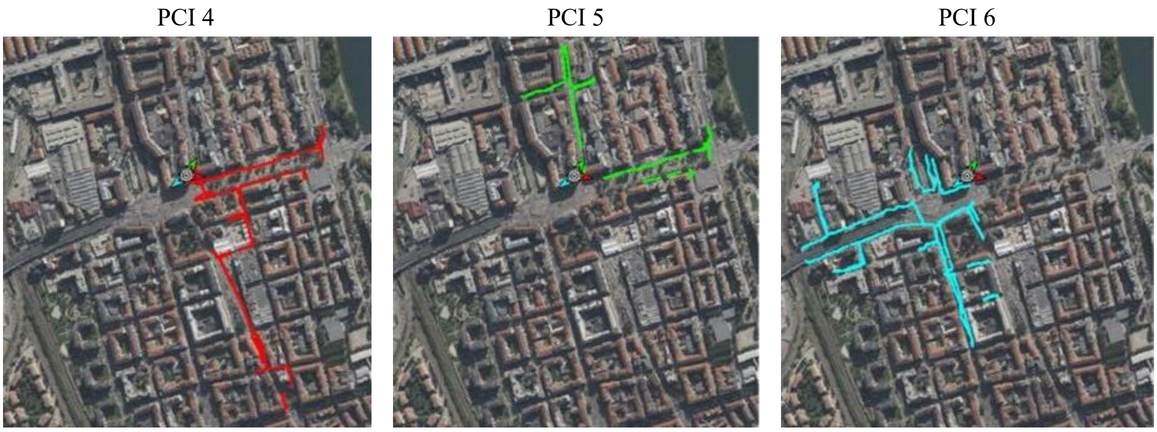

Figure 4.27: Selected routes for ray tracing assessment considering measurement points falling within – 65° , 65° from the antenna pointing direction in the case of PCI4 (red), PCI5 (green) and PCI6 (cyan).

A more detailed analysis can be carried out considering percentiles for PCI4 (see Table 4.13), for PCI5 (see Table 4.14) and for PCI6 (see Table 4.15) and looking at differences between simulated and measured values reported in Table 4.16. Specifically, this last table reports the difference between measurements and numerical simulations percentiles at 50p, 95p and max, together with the difference between the mean of overall measurement and simulated percentiles and the STD of this difference. As can be seen from this last analysis, except for PCI6 case and specifically for the max value, differences between *Exact* and measurements are always below 7 dB, that is an acceptable difference considering the complex environment in which measurements are carried out. Moreover, the overall mean differences between the *Exact* and the other tools (see Table 4.17) are usually below 10 dB, while the specific comparison shows some more pronounced discrepancies with *Matlab* and *Sionna*.
These observations are confirmed by looking at Fig. 4.29. All algorithms are in good agreement with measurements in some areas, but in other zones differences are evident.
To understand where do these differences come from, both experimental and simulated values are shown in the measurement paths for each cell, with a color visualization proportional to the measured or simulated power intensity. More in detail, in Fig. 4.30 measured received power is shown for PCI4, PCI5 and PCI6, while from Fig. 4.31 to Fig. 4.33, computational results are visualized from PCI4 to PCI6, respectively. Starting from PCI4, as can be seen, simulated points in the central street, that is almost in LOS with respect to the BS, have the same trend also com-

pared to measurements, with a slight overestimation for *Exact*. Main differences are obtained in narrow streets, especially for *Sionna*, in which it seems that some ray contributions are missing. This can be related to minor differences in scenario reconstruction, or to some errors in the reconstruction of the antenna diagram. Additionally, some works reported a cell-dependent mismatch of *Sionna* [196]. Moving to PCI5, the agreement between tool results and experimental data is good, except for some data placed at the edges of scenario for *Exact*. Finally, for PCI6, measurement points located in the center of the square are always comparable with measurements, except for *Sionna* in which an overestimation is found. Moreover, as in the previous case, *Exact* underestimates power levels at the edges, together with *Sionna*. Concerning *Exact*, since the scenario is reconstructed inside the tool, some buildings are not considered due to scenario clipping. This condition leads to a loss of reflections and diffractions at the edges.
To confirm this, in Fig. 4.33 the difference between extended and reduced scenario in *Exact* is considered. Simulations are carried out in these two configurations. It is evident from results that by increasing the number of buildings at the scene borders, the simulated power levels are much higher and closer to both measurements and predicted values by other tools.

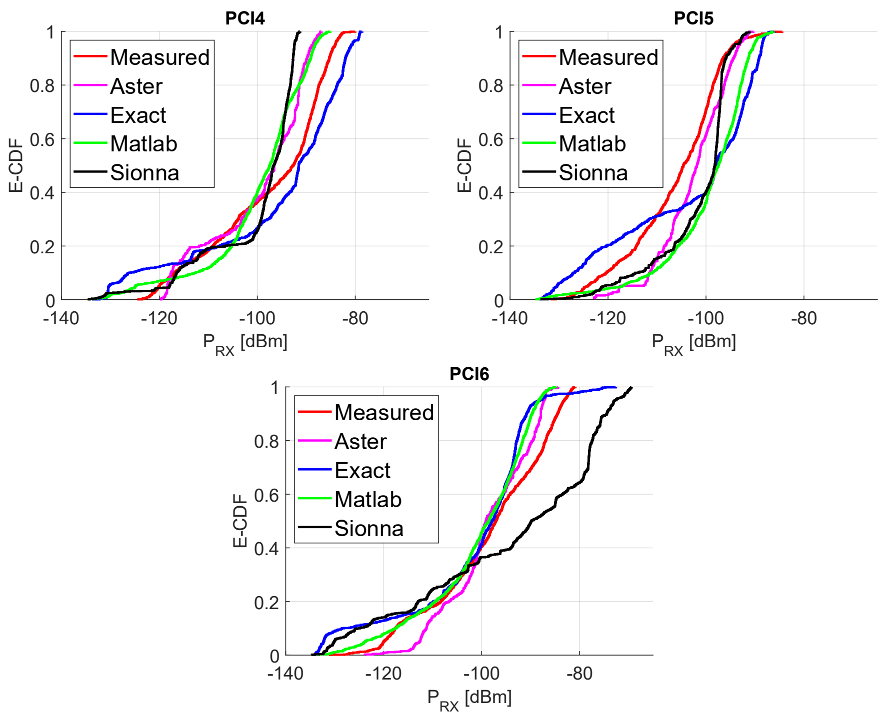

Figure 4.28: E-CDFs obtained with *Exact*, *Matlab*, *Sionna* and *Aster* simulations compared to measurements for PCI4, PCI5 and PCI6.

Percentile	Exact	Matlab	Sionna	Aster	Measured
50p	-93.04	-99.53	-97.82	-98.67	-97.47
60p	-90.94	-96.76	-96.15	-96.11	-92.06
70p	-87.43	-95.02	-94.68	-93.30	-89.70
80p	-84.57	-92.50	-93.67	-91.55	-87.90
90p	-82.23	-89.49	-92.76	-90.3	-85.68
95p	-80.99	-88.44	-92.48	-89.05	-84.45
99p	-79.15	-86.58	-91.85	-87.40	-82.87
max	-78.58	-85.05	-91.23	-86.86	-79.98

Table 4.13: Statistical analysis of simulated and measured electric field data for PCI4. All values are in dBm.

Percentile	Exact	Matlab	Sionna	Aster	Measured
50p	-98.33	-98.10	-98.49	-102.30	-105.01
60p	-95.32	-96.06	-97.83	-100.92	-102.18
70p	-92.96	-94.26	-97.34	-98.66	-100.24
80p	-91.14	-93.06	-96.89	-96.36	-98.66
90p	-89.23	-91.45	-96.10	-94.55	-96.62
95p	-88.56	-90.28	-94.17	-93.36	-94.47
99p	-87.42	-87.80	-91.99	-91.42	-88.61
max	-86.03	-86.19	-91.03	-90.30	-84.43

Table 4.14: Statistical analysis of simulated and measured electric field data for PCI5. All values are in dBm.

Percentile	Exact	Matlab	Sionna	Aster	Measured
50p	-102.69	-102.32	-102.73	-101.65	-101.02
60p	-98.44	-99.18	-90.98	-97.61	-99.48
70p	-95.50	-95.69	-83.66	-93.50	-95.26
80p	-93.42	-92.88	-78.14	-88.44	-91.83
90p	-91.77	-90.31	-75.74	-85.37	-88.30
95p	-89.74	-88.89	-73.33	-83.69	-87.55
99p	-77.79	-86.55	-70.03	-81.74	-86.76
max	-72.57	-84.70	-69.38	-80.83	-84.36

Table 4.15: Statistical analysis of simulated and measured electric field data for PCI6. All values are in dBm.

PCI4				
Percentile	**Exact**	**Matlab**	**Sionna**	**Aster**
50p	-4.44	2.06	0.35	1.20
95p	-3.47	3.99	8.03	4.60
max	-1.40	5.07	11.25	6.88
mean	-2.9	4.16	6.31	4.14
STD	1.17	1.03	3.33	1.57
PCI5				
Percentile	**Exact**	**Matlab**	**Sionna**	**Aster**
50p	-6.68	-6.91	-6.52	-2.71
95p	-5.91	-4.19	-0.30	-1.11
max	1.60	1.75	6.59	5.86
mean	-5.15	-4.13	-0.80	-0.29
STD	3.43	3.02	4.2	3.02
PCI6				
Percentile	**Exact**	**Matlab**	**Sionna**	**Aster**
50p	1.67	1.3	1.71	0.63
95p	2.19	1.34	14.21	3.86
max	11.79	0.34	14.97	3.53
mean	-1.58	0.75	-11.31	-2.72
STD	5.64	0.81	5.81	1.71

Table 4.16: Differences in dB between measured and simulated percentiles of PCI4, PCI5, and PCI6.

PCI4			
Percentile	**Matlab**	**Sionna**	**Aster**
50p	6.49	4.78	5.63
95p	7.45	11.49	8.06
max	6.47	12.65	8.28
mean	2.33	-9.74	-1.13
STD	0.72	3.17	1.31
PCI5			
Percentile	**Matlab**	**Sionna**	**Aster**
50p	-0.22	0.16	3.97
95p	1.72	5.61	4.80
max	0.16	5.00	4.27
mean	1.03	4.36	4.86
STD	0.89	2.11	0.70
PCI6			
Percentile	**Matlab**	**Sionna**	**Aster**
50p	-0.37	0.04	-1.04
95p	-0.85	-16.41	-6.05
max	12.14	-3.19	8.27
mean	2.33	-9.74	-1.13
STD	5.13	6.17	5.09

Table 4.17: Differences in dB between *Exact* tool and simulated percentiles with *Matlab*, *Sionna* and *Aster* for PCI4, PCI5, and PCI6.

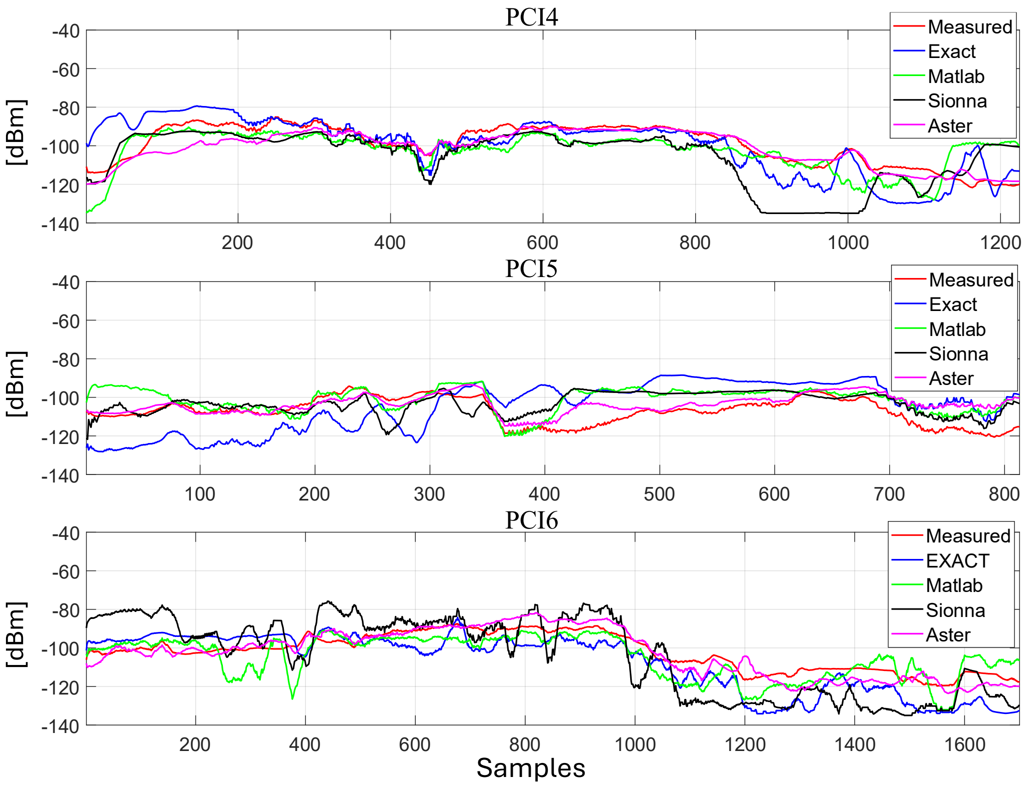

Figure 4.29: Simulated power levels in dBm compared to measured ones in the different antenna sectors (PCI4, PCI5, PCI6). Measurement error of around 2.39 dB is not visible.

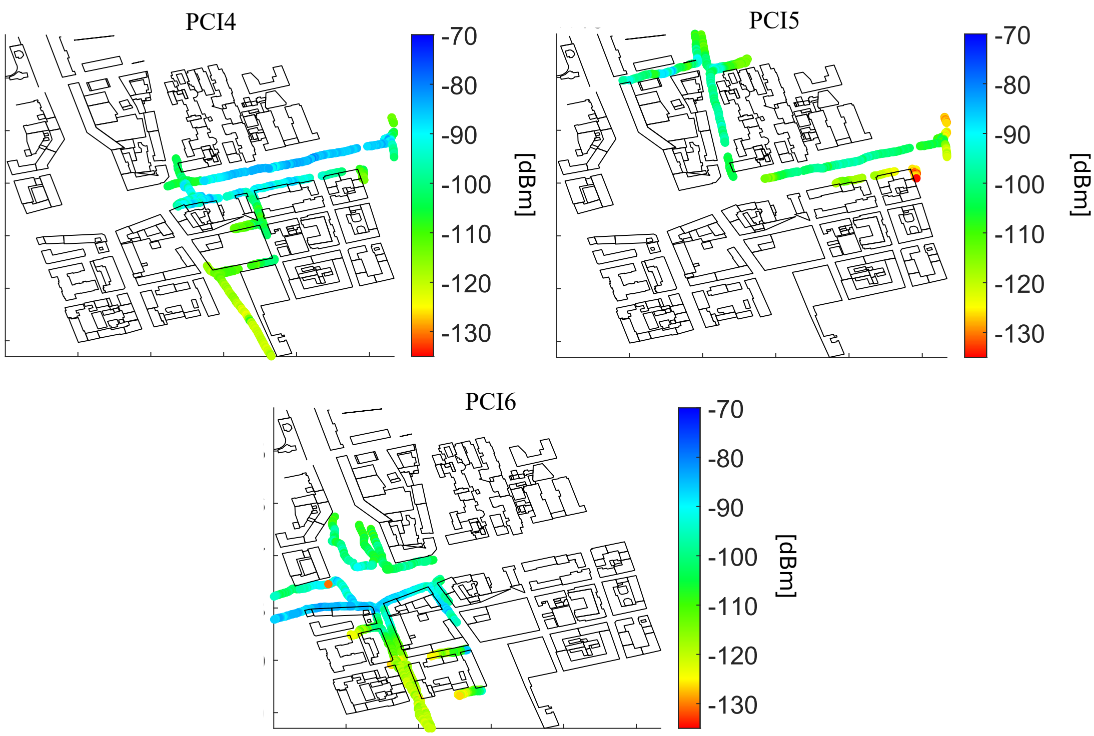

Figure 4.30: Measured power levels [dBm] in measurement points for PCI4, PCI5 and PCI6.

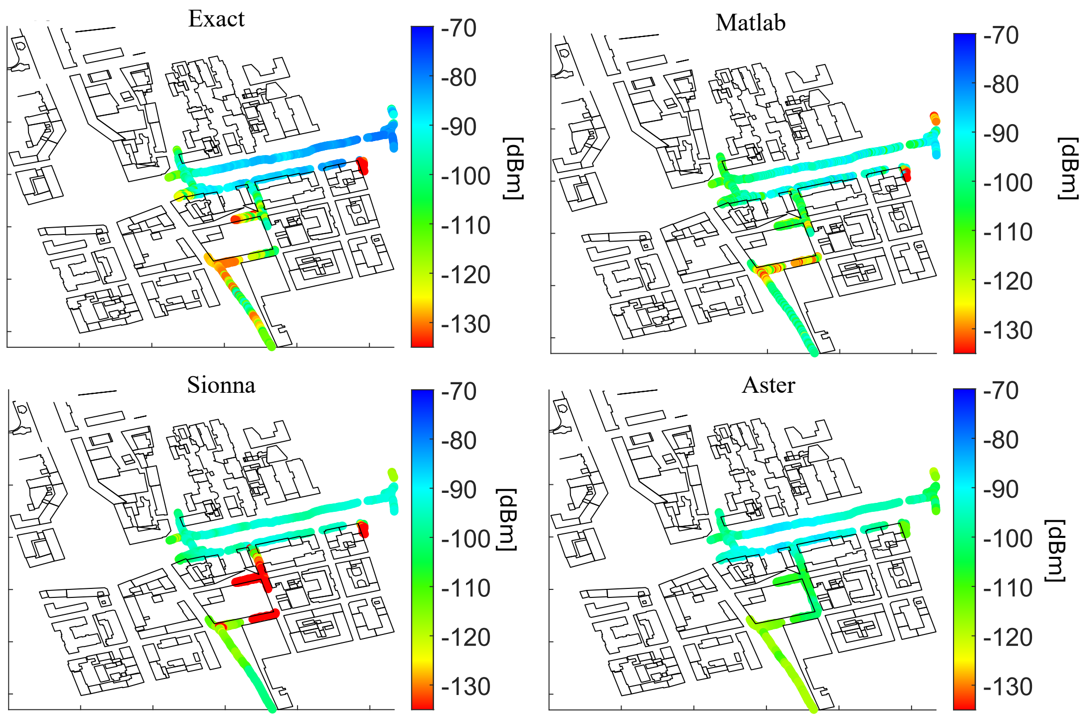

Figure 4.31: Simulated power levels [dBm] for PCI4 in measurement points.

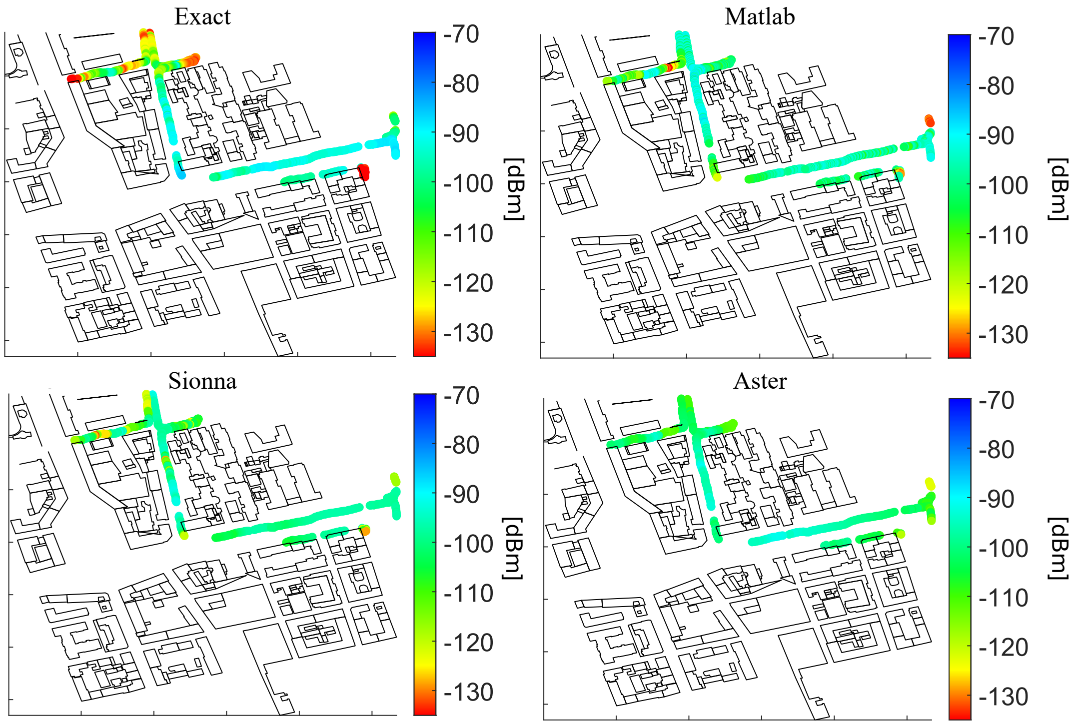

Figure 4.32: Simulated power levels [dBm] for PCI5 in measurement points.

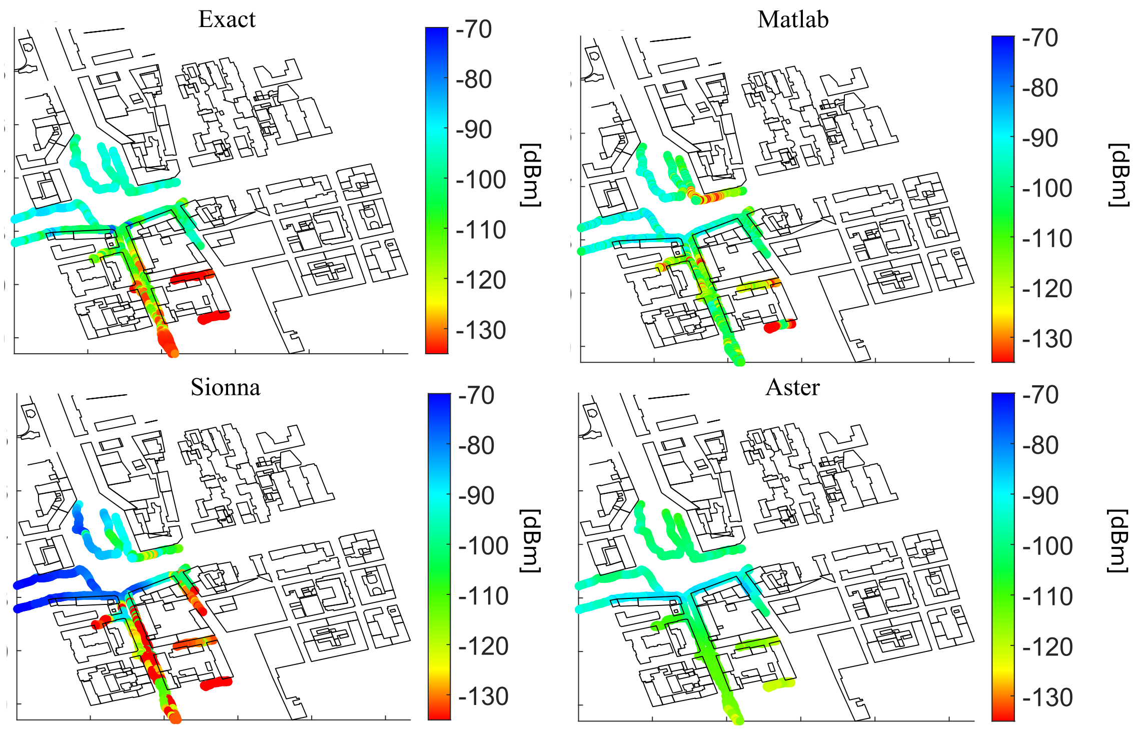

Figure 4.33: Simulated power levels [dBm] for PCI6 in measurement points.

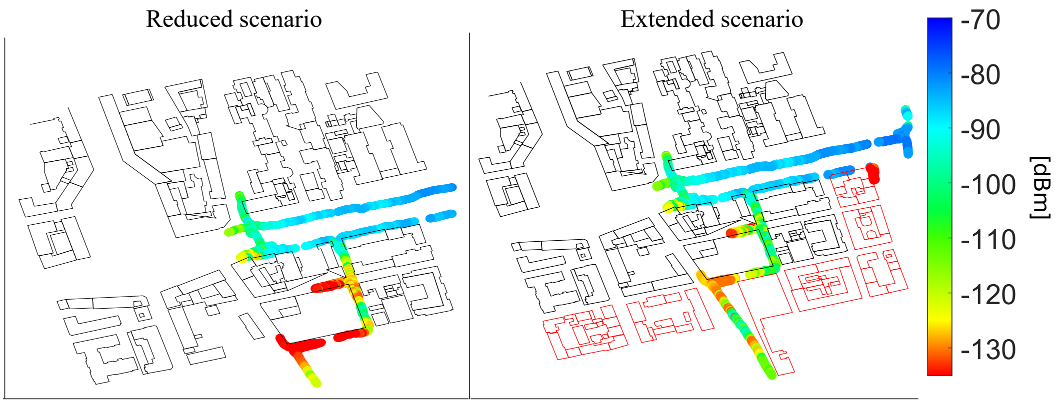

Figure 4.34: Comparison between reduced and extended scenario in *Exact*. The added buildings are shown in red.

4.6 Concluding Remarks

In this Chapter, an in-depth experimental and numerical investigation has been carried out on the presented ray-based algorithm with the aim to evaluate the accuracy of electromagnetic field predictions in 5G scenarios. Indeed, this represents a fundamental step to perform reliable analysis on human exposure and, at the same time, radio coverage assessment. Moreover, the comparison of the algorithm performances with respect to different existing ray-based tools has been addressed to highlight its possible limitations and most suitable use cases. The study also involved three independent institutions, both from innovation centers and companies, bridging the gap between academic research and industrial applications on 5G systems. The extensive collaboration has led to the definition of a generic systematic workflow that enables a simple verification of algorithms' predictions, which can be applied regardless of the employed ray-based method. Results demonstrated that the implementation of the proposed approach provides an easy and suitable procedure for the assessment of propagation models in 5G scenarios, allowing, at the same time, the evaluation of both human exposure and radio coverage metrics. Moreover, outcomes highlighted that, according to the specific ray-based model considered, computational analyses may obviously provide different predictions with acceptable discrepancies for the 5G network design. Indeed, main differences were found for N-LOS areas, therefore more investigations could allow a better accuracy in the results. These considerations were extended and supported by undertaking an extensive measurement campaign in the FR2 band near a massive MIMO antenna located in a complex urban scenario. Comparing measurement results with different propagation models yielded an extended framework, integrating existing computational models, and expanding current knowledge on their performance in a real scenario at mmWaves. Finally, experimental and numerical analyses verified algorithm predictions presented in Chapter 3, proving that for all the considered scenarios electromagnetic field levels are below exposure limits for population according to ICNIRP and Italian regulations, and are also in compliance with safety standards defined by IEC for medical equipment interferences.

Conclusions

In this thesis a thorough and comprehensive analysis on human exposure at 5G frequencies has been presented. The problem of exposure assessment has been addressed both for population and for dosimetry experiments at the human skin level. To these purposes, analytical, computational, and experimental approaches have been adopted, providing a complete overview of the topic. More in detail, ray-based algorithms have been employed for the evaluation of electromagnetic field levels generated by 5G systems working in FR1 and FR2 bands, considering a significant variety of real propagation scenarios. Computational analyses have been supported by experimental data, and to this end an extensive measurement campaign has been carried out near a massiveMIMO BS antenna working in the FR2 band and actually serving a portion of an urban area situated in Italy. Results confirmed robust predictions by ray-based algorithms and led to the definition of a systematic framework for tool assessment, specifically targeted for human exposure evaluation in the context of 5G networks. On the other hand, analytical models to support dosimetry experiments at mmWaves have been developed and validated both numerically and experimentally. Specifically, an electromagnetic model to design solid reflectivity-based phantoms has been implemented, showing an almost perfect agreement with respect to numerical and experimental results. In addition to this, a new solution of the heat transfer equation for very thin phantoms has been proposed and the numerical validation has demonstrated high accuracy in temperature rise predictions, compared to other existing models. Both models have been employed to define a multi-physics optimization approach that is essential for phantom design aimed at assessing the APD by means of thermographic techniques. The efficacy of the proposed method has been demonstrated by designing a broadband carbon+PDMS based phantom that reproduces skin reflection properties in the range 10 - 60 GHz. Indeed, the phantom has been optimized both from the electromagnetic and thermal point of view, resulting in an important advancement with respect to the state of the art in the APD assessment. Finally, all the presented models led to the design, realization and characterization of an OTA testing phantom, providing at the same time important information about electromagnetic properties of the carbon that is widely employed in dosimetry experiments. Therefore, the main contributions of this thesis can be summarized as follows:

- definition of a standardized framework for ray-based tool assessment, targeted to 5G electromagnetic human exposure analysis;
- dissemination and in-depth analysis of an extensive measurement campaign in the FR2 band performed near a massiveMIMO BS actually operative;
- numerical and experimental validation of an electromagnetic model for solid reflectivity-based phantoms design;
- development and numerical validation of a new solution of the heat transfer equation to accurately model the temperature rise inside a thin phantom at mmWaves;
- introduction of a multi-physics optimization approach for the design of solid reflectivity-based phantoms employed in dosimetry experiments based on thermographic techniques;
- design of an optimized broadband skin phantom in the range 10-60 GHz for APD assessment through IR methods;
- analysis and estimation of carbon electromagnetic properties for dosimetry experiments;
- design, development and characterization of an OTA testing phantom by means of advanced techniques.

Overall, these results provide significant advancements in the assessment of human exposure at 5G frequencies both for industry and scientific applications. Indeed, the proposed assessment workflow defines a standardized procedure to evaluate ray-based analysis, without the need of time consuming and challenging measurement campaigns, and this can be extremely helpful for telecom operators to design 5G networks with the final aim to promote their safe large-scale diffusion. Moreover, the presented measurement campaign supports the assessment of electromagnetic field levels in the FR2 band, in which less data are available in the scientific literature compared to the FR1 band. On the other hand, analytical models introduced, together with the multi-physics optimization approach, constitute an important step forward to the design of solid reflectivity-based phantoms employed for APD assessment at mmWaves. As a matter of fact, their implementation led to the design of a broadband phantom emulating scattering properties of the human skin, that can be experimentally reproduced at each frequency in the range 10 - 60 GHz. In addition to this, experiments carried out on carbon+PDMS phantom allowed to derive a preliminary rough estimation of carbon electromagnetic properties and this information can be very helpful to design dosimetry experiments, since this material is actually widely employed for phantom realization both for research and sale purposes. Finally, a phantom that can be adopted in OTA testing to assess performances of wireless devices at mmWaves is realized and characterized by means of innovative techniques, paving the way for new methodologies intended to support human phantoms realization.

References

[1] R. Gai et al. "A review of 5G applications and key technoligies". In: *2021 IEEE 2nd International Conference on Big Data, Artificial Intelligence and Internet of Things Engineering (ICBAIE)*. 2021, pp. 570–574. DOI: 10.1109/ICBAIE52039.2021.9389982.

[2] R. Dangi et al. "Study and Investigation on 5G Technology: A Systematic Review". In: *Sensors* 22.1 (2022). ISSN: 1424-8220. DOI: 10.3390/s22010026. URL: https://www.mdpi.com/1424-8220/22/1/26.

[3] M. M. Elsayed et al. "Vehicles communications handover in 5G: A survey". In: *ICT Express* 9.3 (2023), pp. 366–378. ISSN: 2405-9595. DOI: https://doi.org/10.1016/j.icte.2022.01.005. URL: https://www.sciencedirect.com/science/article/pii/S2405959522000054.

[4] A. M. Peralta-Ochoa et al. "Smart Healthcare Applications over 5G Networks: A Systematic Review". In: *Applied Sciences* 13.3 (2023). ISSN: 2076-3417. DOI: 10.3390/app13031469. URL: https://www.mdpi.com/2076-3417/13/3/1469.

[5] M. Pons et al. "Utilization of 5G Technologies in IoT Applications: Current Limitations by Interference and Network Optimization Difficulties—A Review". In: *Sensors* 23.8 (2023). ISSN: 1424-8220. DOI: 10.3390/s23083876. URL: https://www.mdpi.com/1424-8220/23/8/3876.

[6] T. S. Rappaport et al. "Millimeter Wave Mobile Communications for 5G Cellular: It Will Work!" In: *IEEE Access* 1 (2013), pp. 335–349. DOI: 10.1109/ACCESS.2013.2260813.

[7] T. S. Rappaport et al. "Overview of Millimeter Wave Communications for Fifth-Generation (5G) Wireless Networks—With a Focus on Propagation Models". In: *IEEE Transactions on Antennas and Propagation* 65.12 (2017), pp. 6213–6230. DOI: 10.1109/TAP.2017.2734243.

[8] T. S. Rappaport, J. N. Murdock, and F. Gutierrez. "State of the Art in 60-GHz Integrated Circuits and Systems for Wireless Communications". In: *Proceedings of the IEEE* 99.8 (2011), pp. 1390–1436. DOI: 10.1109/JPROC.2011.2143650.

[9] F. Khan and Z. Pi. "Millimeter wave mobile broadband (MMB): Unleashing the 3–300 GHz spectrum". In: *Proceedings of the 34th IEEE Sarnoff Symposium*. Mar. 2011. DOI: 10.1109/SARNOF.2011.5876482.

[10] Z. Pi and F. Khan. "An introduction to millimeter-wave mobile broadband systems". In: *IEEE Communications Magazine* 49.6 (2011), pp. 101–107. DOI: 10.1109/MCOM.2011.5783993.

[11] S. Rangan, T. S. Rappaport, and E. Erkip. "Millimeter-Wave Cellular Wireless Networks: Potentials and Challenges". In: *Proceedings of the IEEE* 102.3 (2014), pp. 366–385. DOI: 10.1109/JPROC.2014.2299397.

[12] S. Pawar et al. "Prediction of Path-loss Model for Millimeter Wave Communication using Deep Learning". In: *2024 IEEE 3rd World Conference on Applied Intelligence and Computing (AIC)*. 2024, pp. 642–648. DOI: 10.1109/AIC61668.2024.10730843.

[13] M. M. Ahamed and S. Faruque. "5G Network Coverage Planning and Analysis of the Deployment Challenges". In: *Sensors* 21.19 (2021). ISSN: 1424-8220. DOI: 10.3390/s21196608. URL: https://www.mdpi.com/1424-8220/21/19/6608.

[14] B. Praveen Kumar and U. K. Kommuri. "Review on 5G Small Cell Base Station Antennas: Design Challenges and Technologies". In: *IEEE Access* 12 (2024), pp. 85899–85928. DOI: 10.1109/ACCESS.2024.3415640.

[15] E. Yaacoub, M. Husseini, and H. Ghaziri. "An overview of research topics and challenges for 5G massive MIMO antennas". In: *2016 IEEE Middle East Conference on Antennas and Propagation (MECAP)*. 2016, pp. 1–4. DOI: 10.1109/MECAP.2016.7790121.

[16] Manivasagam, Garima, and M. Shukla. "Massive MIMO in 5G Networks: Trends and Challenges". In: *2023 International Conference on Power Energy, Environment Intelligent Control (PEEIC)*. 2023, pp. 1456–1460. DOI: 10.1109/PEEIC59336.2023.10450543.

[17] N. Srinivas, Y. Vellisetty, and P. C. Jain. "Beam Steering and Tracking for 5G Mobile Communication Network in mm Wave Frequency Band". In: *2021 7th International Conference on Signal Processing and Communication (ICSC)*. 2021, pp. 21–25. DOI: 10.1109/ICSC53193.2021.9673419.

[18] T. Wu, T. S. Rappaport, and C. M. Collins. "Safe for Generations to Come". In: *IEEEMicrowave Magazine* 16.2 (Mar. 2015), pp. 65–84. DOI: 10.1109/MMM.2014.2377587.

[19] R. Dilli. "Analysis of 5G Wireless Systems in FR1 and FR2 Frequency Bands". In: *2020 2nd International Conference on Innovative Mechanisms for Industry Applications (ICIMIA)*. 2020, pp. 767–772. DOI: 10.1109/ICIMIA48430.2020.9074973.

[20] S. Kang et al. "Cellular Wireless Networks in the Upper Mid-Band". In: *IEEE Open Journal of the Communications Society* 5 (2024), pp. 2058–2075. DOI: 10.1109/OJCOMS.2024.3373368.

[21] "IEEE Standard Letter Designations for Radar-Frequency Bands". In: *IEEE Std 521-2002 (Revision of IEEE Std 521-1984)* (2003), pp. 1–10. DOI: 10.1109/IEEESTD.2003.94224.

[22] *NR; User Equipment (UE) Radio Transmission and Reception; Part 1: Range 1 Standalone*. Tech. rep. TS 38.101-1. Version 18.5.0. Release 18. 3rd Generation Partnership Project (3GPP), Mar. 2024.

[23] D. Shakya et al. "Propagation measurements and channel models in Indoor Environment at 6.75 GHz FR1(C) and 16.95 GHz FR3 Upper-mid band Spectrum for 5G and 6G". In: *GLOBECOM 2024 - 2024 IEEE Global Communications Conference*. 2024, pp. 998–1003. DOI: 10.1109/GLOBECOM52923.2024.10901735.

[24] *Commission Implementing Decision (EU) 2016/687 of 28 April 2016 on the harmonisation of the 694–790 MHz frequency band for terrestrial systems capable of providing wireless broadband electronic communications services and for flexible national use in the Union. Official Journal of the European Union.* Notified under document C(2016) 2268. Text with EEA relevance. 2016. URL: https://eur-lex.europa.eu/eli/dec_impl/2016/687/oj.

[25] *Commission Decision 2008/411/EC of 21 May 2008 on the harmonisation of the 3400–3800 MHz frequency band for terrestrial systems capable of providing electronic communications services in the Community. Official Journal of the European Union.* Notified under document number C(2008) 1873. Text with EEA relevance. 2008. URL: https://eur-lex.europa.eu/eli/dec/2008/411/oj.

[26] *Commission Implementing Decision (EU) 2019/784 of 14 May 2019 on harmonisation of the 24,25–27,5 GHz frequency band for terrestrial systems capable of providing wireless broadband electronic communications services in the Union. Official Journal of the European Union.* Notified under document C(2019) 3450. Text with EEA relevance. 2019. URL: https://eur-lex.europa.eu/eli/dec_impl/2019/784/oj.

[27] D. Shakya et al. "Comprehensive FR1(C) and FR3 Lower and Upper Mid-Band Propagation and Material Penetration Loss Measurements and Channel Models in Indoor Environment for 5G and 6G". In: *IEEE Open Journal of the Communications Society* 5 (2024), pp. 5192–5218. DOI: 10.1109/OJCOMS.2024.3431686.

[28] B. Fan et al. "The Molecular Mechanism of Retina Light Injury Focusing on Damage from Short Wavelength Light". In: *Oxidative Medicine and Cellular Longevity* 2022 (Apr. 2022), pp. 1–14. DOI: 10.1155/2022/8482149.

[29] W. Hergert and T. Wriedt. *The Mie Theory: Basics and Applications.* Springer Series in Optical Sciences. Springer Berlin Heidelberg, 2012. ISBN: 9783642287381. URL: https://books.google.nl/books?id=wya7BQAAQBAJ.

[30] C. A. Balanis. *Antenna Theory: Analysis and Design.* 4th, illustrated, reprint. John Wiley & Sons, 2016, p. 1104. ISBN: 1118642066, 9781118642061.

[31] A. Facciorusso, M. Di Maso, and N. Muscatiello. "Microwave ablation versus radiofrequency ablation for the treatment of hepatocellular carcinoma: A systematic review and meta-analysis". In: *International Journal of Hyperthermia* 32.3 (2016), pp. 339–344.

[32] F. Lodato et al. "Numerical Modeling of Monopolar Radio Frequency Ablation and Experimental Validation Through Fiber Bragg Gratings Sensors". In: *2024 IEEE Sensors Applications Symposium (SAS)*. 2024, pp. 1–6. DOI: 10.1109/SAS60918.2024.10636481.

[33] F. Lodato et al. "Thermal Analysis of Ex-Vivo Liver RF Ablation through Numerical Modeling and Fiber Bragg Gratings Validation". In: Jan. 2024. DOI: 10.46620/URSIATRASC24/HHWG7383.

[34] F. Lodato et al. "Radio Frequency Ablation of Liver Tissue Assisted by Saline Infusion: Computational Modeling and Experimental Assessment". In: *IEEE Transactions on Instrumentation and Measurement* 74 (2025), pp. 1–11. DOI: 10.1109/TIM.2025.3563053.

[35] P. P. Falciglia et al. "A review on the microwave heating as a sustainable technique for environmental remediation/detoxification applications". In: *Renewable and Sustainable Energy Reviews* 95 (2018), pp. 147–170. ISSN: 1364-0321. DOI: https://doi.org/10.1016/j.rser.2018.07.031. URL: https://www.sciencedirect.com/science/article/pii/S1364032118305392.

[36] N. D'Ambrosio et al. "Microwave-Induced Inhibition of Germination in Portulaca oleracea L. Seeds". In: *Agronomy* 15.10 (2025). ISSN: 2073-4395. DOI: 10.3390/agronomy15102418. URL: https://www.mdpi.com/2073-4395/15/10/2418.

[37] R. Massa et al. "Preliminary Results on Fungicidal Efficacy of Microwave Treatment on Fusarium oxysporum". In: *2024 4th URSI Atlantic Radio Science Meeting (AT-RASC)*. 2024, pp. 1–4. DOI: 10.46620/URSIATRASC24/DCKD7279.

[38] M. Ziane, A. Boriskin, and M. Zhadobov. "Fast In-Phantom Absorbed Power Density Evaluation at mmWaves Based on Infrared Measurements". In: *IEEE Journal of Microwaves* 5.2 (2025), pp. 269–280. DOI: 10.1109/JMW.2025.3539871.

[39] S.-R. Tsai and M. R. Hamblin. "Biological effects and medical applications of infrared radiation". In: *Journal of Photochemistry and Photobiology B: Biology* 170 (2017), pp. 197–207. ISSN: 1011-1344. DOI: https://doi.org/10.1016/j.jphotobiol.2017.04.014. URL: https://www.sciencedirect.com/science/article/pii/S1011134416311691.

[40] L. M. Ng and R. Simmons. "Infrared spectroscopy". In: *Analytical chemistry* 71.12 (1999), pp. 343–350.

[41] J. Chen, S. Loeb, and J.-H. Kim. "LED revolution: fundamentals and prospects for UV disinfection applications". In: *Environmental Science: Water Research & Technology* 3.2 (2017), pp. 188–202.

[42] A. Gupta et al. “Ultraviolet radiation in wound care: sterilization and stimulation”. In: *Advances in wound care* 2.8 (2013), pp. 422–437.

[43] A. F. M. Shahen Shah. “A Survey From 1G to 5G Including the Advent of 6G: Architectures, Multiple Access Techniques, and Emerging Technologies”. In: *2022 IEEE 12th Annual Computing and Communication Workshop and Conference (CCWC)*. 2022, pp. 1117–1123. DOI: 10.1109/CCWC54503.2022.9720781.

[44] V. Pawar et al. “Evolution of 6G - an In-depth Study on History of Spectrum Allocation”. In: *2023 International Conference on Integrated Intelligence and Communication Systems (ICIICS)*. 2023, pp. 1–6. DOI: 10.1109/ICIICS59993.2023.10421327.

[45] International Commission on Non-Ionizing Radiation Protection (ICNIRP). “Guidelines for Limiting Exposure to Electromagnetic Fields (100 kHz to 300 GHz)”. In: *Health Physics* 118.5 (2020), pp. 483–524. DOI: 10.1097/HP.0000000000001210.

[46] R. Pethig and D. Kell. “The passive electrical properties of biological systems: Their significance in physiology, biophysics and biotechnology”. In: *Physics in medicine and biology* 32 (Sept. 1987), pp. 933–70. DOI: 10.1088/0031-9155/32/8/001.

[47] ICNIRP. *International Commission on Non-Ionizing Radiation Protection.* https://www.icnirp.org. [Online; accessed 20-Nov-2025].

[48] ICNIRP. “ICNIRP Guidelines for Limiting Exposure to Time-Varying Electric, Magnetic and Electromagnetic Fields (up to 300 GHz)”. In: *Health Physics* 74.4 (1998), pp. 494–522.

[49] L. Vallozzi, C. Hertleer, and H. Rogier. “26 - Latest developments in the field of textile antennas”. In: *Smart Textiles and their Applications*. Ed. by V. Koncar. Woodhead Publishing Series in Textiles. Oxford: Woodhead Publishing, 2016, pp. 599–626. ISBN: 978-0-08-100574-3. DOI: https://doi.org/10.1016/B978-0-08-100574-3.00026-6. URL: https://www.sciencedirect.com/science/article/pii/B9780081005743000266.

[50] IEEE. *IEEE Standard for Safety Levels with Respect to Human Exposure to the Radio Frequency Electromagnetic Fields, 3 kHz to 300 GHz.* IEEE Standard C95.1. 2005.

[51] ICNIRP. "Review of Concepts, Quantities, Units and Terminology for Non-Ionizing Radiation Protection". In: *Health Physics* 105.6 (2013), pp. 550–568.

[52] D. Poljak et al. "On the use of the boundary element analysis in bioelectromagnetics". In: *Engineering Analysis with Boundary Elements* 49 (2014). Special issue on Bioelectromagnetics, pp. 2–14. ISSN: 0955-7997. DOI: https://doi.org/10.1016/j.enganabound.2014.02.008. URL: https://www.sciencedirect.com/science/article/pii/S0955799714000538.

[53] B. Greenebaum. *Bioengineering and Biophysical Aspects of Electromagnetic Fields*. Nov. 2018. ISBN: 9781315186580. DOI: 10.1201/9781315186580.

[54] T. Samaras, A. Christ, and N. Kuster. "Compliance Assessment of the Epithelial or Absorbed Power Density Below 10GHz Using SAR Measurement Systems". In: *Bioelectromagnetics* 42.6 (2021), pp. 484–490. DOI: https://doi.org/10.1002/bem.22355.

[55] L. Filosa and V. Lopresto. "Assessment and Management of Risks from Occupational Exposure to Electromagnetic Fields (0 Hz to 300 GHz): A Compass to Keep the Right Course Through European and Italian Regulations". In: *Safety* 10.4 (2024). ISSN: 2313-576X. DOI: 10.3390/safety10040104. URL: https://www.mdpi.com/2313-576X/10/4/104.

[56] *EN 62232:2022, Edition 3.0 — Determination of RF field strength, power density and SAR in the vicinity of base stations for the purpose of evaluating human exposure*. European Standard, identical to IEC 62232:2022 (Edition 3.0). 2022. URL: https://standards.cencenelec.eu/dyn/www/f?p=204:110:0::::FSP_PROJECT,FSP_ORG_ID:75117,1258303.

[57] *Determination of RF field strength, power density and SAR in the vicinity of base stations for the purpose of evaluating human exposure*. Fourth edition. Cancels and replaces IEC 62232:2022. Same technical content with corrections and improved clarity. Geneva, Switzerland, 2025.

[58] G. S. Bhatia, Y. Corre, and M. Di Renzo. "Tuning of Ray-Based Channel Model for 5G Indoor Industrial Scenarios". In: *2023 IEEE International Mediterranean Conference on Communications and Networking (MeditCom)*. 2023, pp. 311–316. DOI: 10.1109/MeditCom58224.2023.10266601.

[59] A.-Y. Hsiao et al. “Ray tracing simulations for millimeter wave propagation in 5G wireless communications”. In: *2017 IEEE International Symposium on Antennas and Propagation USNC/URSI National Radio Science Meeting.* 2017, pp. 1901–1902. DOI: 10.1109/APUSNCURSINRSM.2017.8072993.

[60] M. Migliore. “5G Field level measurement for human exposure assessment: A lesson for 6G”. In: *IOP Conference Series: Materials Science and Engineering* 1254 (Sept. 2022), p. 012001. DOI: 10.1088/1757-899X/1254/1/012001.

[61] M. Zhu et al. “Toward Real-Time Digital Twins of EM Environments: Computational Benchmark for Ray Launching Software”. In: *IEEE Open Journal of the Communications Society* 5 (2024), pp. 6291–6302. DOI: 10.1109/OJCOMS.2024.3463963.

[62] K. Guido et al. “Tissue-Emulating Phantoms for In Vitro Experimentation at Radio Frequencies: Exploring Characteristics, Fabrication, and Testing Methods”. In: *IEEE Antennas and Propagation Magazine* PP (Aug. 2020). DOI: 10.1109/MAP.2020.3003208.

[63] “IEEE Recommended Practice for Determining the Peak Spatial-Average Specific Absorption Rate (SAR) in the Human Head from Wireless Communications Devices: Measurement Techniques”. In: *IEEE Std 1528-2003* (2003), pp. 1–120. DOI: 10.1109/IEEESTD.2003.94414.

[64] “IEC/IEEE International Standard - Measurement procedure for the assessment of specific absorption rate of human exposure to radio frequency fields from hand-held and body-mounted wireless communication devices – Part 1528: Human models, instrumentation, and procedures (Frequency range of 4 MHz to 10 GHz)”. In: *IEC/IEEE 62209-1528:2020* (2020), pp. 1–284. DOI: 10.1109/IEEESTD.2020.9231298.

[65] International Electrotechnical Commission (IEC). *Conversion method of specific absorption rate to absorbed power density for the assessment of human exposure to radio frequency electromagnetic fields from wireless devices in close proximity to the head and body – Frequency range of 6 GHz to 10 GHz.* Publicly Available Specification PAS 63446. IEC, 2022, p. 22. URL: https://webstore.iec.ch/en/publication/75849.

[66] K. Ito et al. “Development and characteristics of a biological tissue-equivalent phantom for microwaves”. In: *Electronics and Communications in Japan (Part*

I: Communications) 84.4 (2001), pp. 67–77. DOI: `https://doi.org/10.1002/1520-6424(200104)84:4<67::AID-ECJA8>3.0.CO;2-D`.

[67] T. Onishi et al. "Biological Tissue-Equivalent Agar-Based Solid Phantoms and SAR Estimation Using the Thermographic Method in the Range of 3–6 GHz". In: *IEICE Transactions on Communications* E88-B.9 (Sept. 2005), pp. 3733–3741. DOI: `10.1093/ietcom/e88-b.9.3733`.

[68] S. Adda et al. "A Theoretical and Experimental Investigation on the Measurement of the Electromagnetic Field Level Radiated by 5G Base Stations". In: *IEEE Access* 8 (2020), pp. 101448–101463. DOI: `10.1109/ACCESS.2020.2998448`.

[69] S. Hur et al. "Proposal on Millimeter-Wave Channel Modeling for 5G Cellular System". In: *IEEE Journal of Selected Topics in Signal Processing* 10.3 (2016), pp. 454–469. DOI: `10.1109/JSTSP.2016.2527364`.

[70] M. Peter et al. "Channel Measurement and Modeling for 5G Urban Microcellular Scenarios". In: *Sensors* 16.8 (2016). ISSN: 1424-8220. DOI: `10.3390/s16081330`. URL: `https://www.mdpi.com/1424-8220/16/8/1330`.

[71] Z. Zhang et al. "Ray-tracing Simulation and Analysis of 5G Channel Characteristics in Dense Urban Areas". In: *2022 IEEE International Symposium on Antennas and Propagation and USNC-URSI Radio Science Meeting (AP-S/URSI)*. 2022, pp. 1690–1691. DOI: `10.1109/AP-S/USNC-URSI47032.2022.9886969`.

[72] S. Shikhantsov et al. "Ray-Tracing-Based Numerical Assessment of the Spatiotemporal Duty Cycle of 5G Massive MIMO in an Outdoor Urban Environment". In: *Applied Sciences* 10.21 (2020). ISSN: 2076-3417. DOI: `10.3390/app10217631`. URL: `https://www.mdpi.com/2076-3417/10/21/7631`.

[73] V. Ravuri et al. "Performance Analysis of 5G Micro-Cell Coverage with 3D Ray Tracing". In: *Communication, Software and Networks*. Ed. by V. Bhateja et al. Singapore: Springer Nature Singapore, 2023, pp. 393–401. ISBN: 978-981-19-4990-6.

[74] A. de Oliveira et al. "Ray-Tracing 5G Channels from Scenarios with Mobility Control of Vehicles and Pedestrians". In: *Anais de XXXVII Simpósio Brasileiro de Telecomunicações e Processamento de Sinais* (2020). URL: `https://api.semanticscholar.org/CorpusID:210919939`.

[75] G. Koutitas and T. Samaras. "Exposure Minimization in Indoor Wireless Networks". In: *IEEE Antennas and Wireless Propagation Letters* 9 (2010), pp. 199–202. DOI: 10.1109/LAWP.2010.2045870.

[76] P. Gajšek et al. "EMF Exposure of Workers Due to 5G Private Networks in Smart Industries". In: *Electronics* 14.13 (2025). ISSN: 2079-9292. DOI: 10.3390/electronics14132662. URL: https://www.mdpi.com/2079-9292/14/13/2662.

[77] Z. Yun, S. Lim, and M. Iskander. "An Integrated Method of Ray Tracing and Genetic Algorithm for Optimizing Coverage in Indoor Wireless Networks". In: *Antennas and Wireless Propagation Letters, IEEE* 7 (Feb. 2008), pp. 145–148. DOI: 10.1109/LAWP.2008.919358.

[78] D. He et al. "The Design and Applications of High-Performance Ray-Tracing Simulation Platform for 5G and Beyond Wireless Communications: A Tutorial". In: *IEEE Communications Surveys Tutorials* 21.1 (2019), pp. 10–27. DOI: 10.1109/COMST.2018.2865724.

[79] T. Sharma, A. Chehri, and P. Fortier. "Reconfigurable Intelligent Surfaces for 5G and beyond Wireless Communications: A Comprehensive Survey". In: *Energies* 14.24 (2021). ISSN: 1996-1073. DOI: 10.3390/en14248219. URL: https://www.mdpi.com/1996-1073/14/24/8219.

[80] I. Mahmud and A. Abdelhadi. "Neural Network Based Ray Tracing on a Digital Twin for Performance Approximation Using Parameter Analysis". In: *2024 International Conference on Computer and Applications (ICCA)*. 2024, pp. 1–6. DOI: 10.1109/ICCA62237.2024.10927985.

[81] O. Yildiz. "Digital Twin-Based Ray Tracing Analysis for Antenna Orientation Optimization in Wireless Networks". In: *Electronics* 14.15 (2025). ISSN: 2079-9292. DOI: 10.3390/electronics14153023. URL: https://www.mdpi.com/2079-9292/14/15/3023.

[82] M. Zhu et al. "On the Digitization of the EM Environment: A Comparison of Ray Launching Solutions". In: *2024 IEEE International Mediterranean Conference on Communications and Networking (MeditCom)*. 2024, pp. 85–90. DOI: 10.1109/MeditCom61057.2024.10621310.

[83] M. Iskander and Z. Yun. "Propagation prediction models for wireless communication systems". In: *IEEE Transactions on Microwave Theory and Techniques* 50.3 (2002), pp. 662–673. DOI: 10.1109/22.989951.

[84] Z. Yun and M. F. Iskander. "Ray Tracing for Radio Propagation Modeling: Principles and Applications". In: *IEEE Access* 3 (2015), pp. 1089–1100. DOI: 10.1109/ACCESS.2015.2453991.

[85] J. Hoydis et al. "Sionna RT: Differentiable Ray Tracing for Radio Propagation Modeling". In: *2023 IEEE Globecom Workshops (GC Wkshps)*. 2023, pp. 317–321. DOI: 10.1109/GCWkshps58843.2023.10465179.

[86] J. Eertmans, L. Jacques, and C. Oestges. "Fully Differentiable Ray Tracing via Discontinuity Smoothing for Radio Network Optimization". In: Mar. 2024, pp. 1–5. DOI: 10.23919/EuCAP60739.2024.10501570.

[87] R. Kouyoumjian and P. Pathak. "A uniform geometrical theory of diffraction for an edge in a perfectly conducting surface". In: *Proceedings of the IEEE* 62.11 (1974), pp. 1448–1461. DOI: 10.1109/PROC.1974.9651.

[88] Y. A. Alqudah. "On the performance of Cost 231 Walfisch Ikegami model in deployed 3.5 GHz network". In: *2013 The International Conference on Technological Advances in Electrical, Electronics and Computer Engineering (TAEECE)*. 2013, pp. 524–527. DOI: 10.1109/TAEECE.2013.6557329.

[89] J. Deygout. "Multiple knife-edge diffraction of microwaves". In: *IEEE Transactions on Antennas and Propagation* 14.4 (1966), pp. 480–489. DOI: 10.1109/TAP.1966.1138719.

[90] A. W. Mbugua et al. "Review on Ray Tracing Channel Simulation Accuracy in Sub-6 GHz Outdoor Deployment Scenarios". In: *IEEE Open Journal of Antennas and Propagation* 2 (2021), pp. 22–37. DOI: 10.1109/OJAP.2020.3041953.

[91] A. Saleem et al. "A Critical Review on Channel Modeling: Implementations, Challenges and Applications". In: *Electronics* 12.9 (2023). ISSN: 2079-9292. DOI: 10.3390/electronics12092014. URL: https://www.mdpi.com/2079-9292/12/9/2014.

[92] *EMF-Portal*. https://www.emf-portal.org/en. Accessed: 2025-11-25. EMF-Portal, 2025.

[93] X. Lin. "3GPP Evolution from 5G to 6G: A 10-Year Retrospective". In: *Telecom* 6.2 (2025). ISSN: 2673-4001. DOI: 10.3390/telecom6020032. URL: https://www.mdpi.com/2673-4001/6/2/32.

[94] L.-M. Schilling et al. "Assessment of Mobile Radio Exposure With Digital Twins". In: *2025 19th European Conference on Antennas and Propagation (EuCAP)*. 2025, pp. 1–5. DOI: 10.23919/EuCAP63536.2025.10999607.

[95] M. Leeman et al. "City-Scale Spatio-Temporal Modeling of 5G Downlink Exposure of Users and Non-Users by Ray-Tracing in a Real Urban Environment". In: *IEEE Access* 13 (2025), pp. 30894–30906. DOI: 10.1109/ACCESS.2025.3541352.

[96] S. S. Zhekov and B. Xu. "Evaluation of EMF Exposure From Distributed MIMO Antennas for 6G in an Industrial Indoor Environment". In: *IEEE Transactions on Electromagnetic Compatibility* 67.2 (2025), pp. 403–417. DOI: 10.1109/TEMC.2024.3474038.

[97] Y. H. Santana et al. "5G mmWave Network Planning Using Machine Learning for Path Loss Estimation". In: *IEEE Open Journal of the Communications Society* 5 (2024), pp. 3451–3467. DOI: 10.1109/OJCOMS.2024.3405742.

[98] Z. Yang et al. "Analysis of Electromagnetic Radiation of Mobile Base Stations Co-located with High-Voltage Transmission Towers". In: *Symmetry* 15.6 (2023). ISSN: 2073-8994. DOI: 10.3390/sym15061252. URL: https://www.mdpi.com/2073-8994/15/6/1252.

[99] L.-M. Schilling et al. "Optimized Assessment Procedure for Maximal RF Exposure to 5G Massive MIMO Base Stations in Non-Line-of-Sight Scenarios – Part 1: Theoretical and Numerical Investigations". In: *2023 17th European Conference on Antennas and Propagation (EuCAP)*. 2023, pp. 1–5. DOI: 10.23919/EuCAP57121.2023.10133658.

[100] Y.-Y. Wang et al. "Dual-Loop Antenna for 4G LTE MIMO Smart Glasses Applications". In: *IEEE Antennas and Wireless Propagation Letters* 18.9 (2019), pp. 1818–1822. DOI: 10.1109/LAWP.2019.2930726.

[101] M. A. Salem et al. "Investigation of EMF exposure level for uplink and downlink of 5G network using ray tracing approach". In: *International Journal of Technology* 13.6 (2022), pp. 1298–1307.

[102] N. Noé and F. Gaudaire. "Numerical Modeling of the Effect of the Built Environment and Usages on Downlink EMF Exposure Induced by MU-MIMO 5G Antennas". In: *2021 XXXIVth General Assembly and Scientific Symposium of the International Union of Radio Science (URSI GASS)*. 2021, pp. 1–4. DOI: 10.23919/URSIGASS51995.2021.9560503.

[103] Y. S. Lee et al. "Study on the Appropriate Measurement Spacing for EMF Installation Compliance Assessments of a 3.5 GHz 5G Base Station". In: *IEEE Access* 9 (2021), pp. 88167–88176. DOI: 10.1109/ACCESS.2021.3078764.

[104] M. Matalatala Tamasala et al. "Combined Ray-Tracing/FDTD and Network Planner Methods for the Design of Massive MIMO Networks". In: *IEEE Access* 8 (2020), pp. 206371–206387. DOI: 10.1109/ACCESS.2020.3035317.

[105] S. Shikhantsov et al. "Massive MIMO Propagation Modeling With User-Induced Coupling Effects Using Ray-Tracing and FDTD". In: *IEEE Journal on Selected Areas in Communications* 38.9 (2020), pp. 1955–1963. DOI: 10.1109/JSAC.2020.3000874.

[106] S. Shikhantsov et al. "Hybrid Ray-Tracing/FDTD Method for Human Exposure Evaluation of a Massive MIMO Technology in an Industrial Indoor Environment". In: *IEEE Access* 7 (2019), pp. 21020–21031. DOI: 10.1109/ACCESS.2019.2897921.

[107] M. Celaya-Echarri et al. "5G Spatial Modeling of Personal RF-EMF Assessment Within Aircrafts Cabin Environments". In: *IEEE Access* 10 (2022), pp. 78860–78874. DOI: 10.1109/ACCESS.2022.3193681.

[108] M. Celaya-Echarri et al. "Towards Environmental RF-EMF Assessment of mmWave High-Node Density Complex Heterogeneous Environments". In: *Sensors* 21.24 (2021). ISSN: 1424-8220. DOI: 10.3390/s21248419. URL: https://www.mdpi.com/1424-8220/21/24/8419.

[109] M. Celaya-Echarri et al. "Empirical and Modeling Approach for Environmental Indoor RF-EMF Assessment in Complex High-Node Density Scenarios: Public Shopping Malls Case Study". In: *IEEE Access* 9 (2021), pp. 46755–46775. DOI: 10.1109/ACCESS.2021.3067852.

[110] D. Pinchera, M. Migliore, and F. Schettino. "Compliance Boundaries of 5G Massive MIMO Radio Base Stations: A Statistical Approach". In: *IEEE Access* 8 (2020), pp. 182787–182800. DOI: 10.1109/ACCESS.2020.3028471.

[111] M. Celaya-Echarri et al. "From 2G to 5G Spatial Modeling of Personal RF-EMF Exposure Within Urban Public Trams". In: *IEEE Access* 8 (2020), pp. 100930–100947. DOI: 10.1109/ACCESS.2020.2997254.

[112] L. Chiaraviglio et al. "Measuring 5G Exposure From Multiple Terminals and Base Station in Standalone FWA Networks". In: *IEEE Access* 13 (2025), pp. 87438–87461. DOI: 10.1109/ACCESS.2025.3568246.

[113] S. Valbonesi et al. "Evaluation of Coverage and Radio-Frequency Electromagnetic Field Exposure in Complex Scenarios: Critical Issues and Possible Solutions". In: *2024 IEEE International Symposium on Measurements Networking (MN)*. 2024, pp. 1–6. DOI: 10.1109/MN60932.2024.10615546.

[114] L. Chiaraviglio et al. "Measuring EMF and Throughput Before and After 5G Service Activation in a Residential Area". In: *IEEE Open Journal of the Communications Society* 4 (2023), pp. 1179–1195. DOI: 10.1109/OJCOMS.2023.3277782.

[115] K. Ali et al. "Measurement Campaign on 5G Indoor Millimeter Wave and Visible Light Communications Multi Component Carrier System". In: *IEEE Transactions on Broadcasting* 68.1 (2022), pp. 156–170. DOI: 10.1109/TBC.2021.3120918.

[116] N. Noé and F. Gaudaire. "Simulation of 5G MU-MIMO radiation patterns in the 3.5 GHz band in urban environments for future EMF exposure assessment". In: *2022 3rd URSI Atlantic and Asia Pacific Radio Science Meeting (AT-AP-RASC)*. 2022, pp. 1–4. DOI: 10.23919/AT-AP-RASC54737.2022.9814272.

[117] M. Benini et al. "Evaluation of Road User Radio-Frequency Exposure Levels in an Urban Environment From Vehicular Antennas and the Infrastructure in ITS-G5 5.9 GHz Communication". In: *IEEE Access* 12 (2024), pp. 51419–51430. DOI: 10.1109/ACCESS.2024.3385664.

[118] M. Benini et al. "Human Exposure to RF-EMF From Active RIS in Outdoor Environments: a Vehicular Communication Case Study". In: *IEEE Open Journal of Antennas and Propagation* (2025), pp. 1–1. DOI: 10.1109/OJAP.2025.3625767.

[119] S. Gallucci et al. "6G RIS in Indoor Environments: Assessment of Exposure Variability in Human Users and Non-Users". In: *IEEE Open Journal of Antennas and Propagation* 6.2 (2025), pp. 487–496. DOI: 10.1109/OJAP.2025.3529980.

[120] D. Sharma, S. K. Dubey, and V. N. Ojha. "Wearable Antenna for millimeter wave 5G Communications". In: *2018 IEEE Indian Conference on Antennas and Propogation (InCAP)*. 2018, pp. 1–4. DOI: 10.1109/INCAP.2018.8770921.

[121] H. A. Rahim et al. "5G Millimeter Wave Wearable Antenna: State-Of-the-Art and Current Challenges". In: *2021 IEEE Asia-Pacific Conference on Applied Electromagnetics (APACE)*. 2021, pp. 1–4. DOI: 10.1109/APACE53143.2021.9760662.

[122] N. Chahat, M. Zhadobov, and R. Sauleau. "Broadband Tissue-Equivalent Phantom for BAN Applications at Millimeter Waves". In: *IEEE Transactions on Microwave Theory and Techniques* 60.7 (2012), pp. 2259–2266. DOI: 10.1109/TMTT.2012.2195196.

[123] V. Turgul and I. Kale. "Characterization of the complex permittivity of glucose/water solutions for noninvasive RF/Microwave blood glucose sensing". In: *2016 IEEE International Instrumentation and Measurement Technology Conference Proceedings*. 2016, pp. 1–5. DOI: 10.1109/I2MTC.2016.7520546.

[124] K. Fuchs and U. Kaatze. "Molecular Dynamics Of Carbohydrate Aqueous Solutions. Dielectric Relaxation as a Function of Glucose and Fructose Concentration". In: *Journal of Physical Chemistry B - J PHYS CHEM B* 105 (Feb. 2001). DOI: 10.1021/jp0030084.

[125] A. Peyman, C. Gabriel, and E. Grant. "Complex permittivity of sodium chloride solutions at microwave frequencies". In: *Bioelectromagnetics* 28.4 (2007), pp. 264–274. DOI: https://doi.org/10.1002/bem.20271. eprint: https://onlinelibrary.wiley.com/doi/pdf/10.1002/bem.20271. URL: https://onlinelibrary.wiley.com/doi/abs/10.1002/bem.20271.

[126] K. Fukunaga, S. Watanabe, and Y. Yamanaka. "Dielectric properties of tissue-equivalent liquids and their effects on specific absorption rate". In: *IEEE Transactions on Electromagnetic Compatibility* 46.1 (2004), pp. 126–129. DOI: 10.1109/TEMC.2004.823624.

[127] S. Romeo et al. "Dielectric characterization study of liquid based materials for mimicking breast tissues". In: *Microwave and Optical Technology Letters* 53 (June 2011), pp. 1276–1280. DOI: 10.1002/mop.26001.

[128] S. A. Lopez-Haro et al. "An agarose based phantom embedded in an in vitro liver tissue to simulate tumors: First experience". In: *2011 Pan American Health Care Exchanges*. 2011, pp. 233–236. DOI: 10.1109/PAHCE.2011.5871892.

[129] H. Kato, M. Hiraoka, and T. Ishida. “An agar phantom for hyperthermia”. In: *Medical Physics* 13.3 (1986), pp. 396–398. DOI: https://doi.org/10.1118/1.595882. eprint: https://aapm.onlinelibrary.wiley.com/doi/pdf/10.1118/1.595882. URL: https://aapm.onlinelibrary.wiley.com/doi/abs/10.1118/1.595882.

[130] K. Tomura et al. “The usefulness of mobile insulator sheets for the optimization of deep heating area for regional hyperthermia using a capacitively-coupled heating method: Phantom, simulation and clinical prospective studies”. In: *International Journal of Hyperthermia* 34 (Nov. 2017), pp. 1–48. DOI: 10.1080/02656736.2017.1402130.

[131] S. Oh et al. “Measurement of SAR-induced temperature increase in a phantom and in vivo with comparison to numerical simulation”. In: *Magnetic resonance in medicine : official journal of the Society of Magnetic Resonance in Medicine / Society of Magnetic Resonance in Medicine* 71 (May 2014). DOI: 10.1002/mrm.24820.

[132] J. Vorlíček, B. Vrbova, and J. Vrba. “Prospective Applications of Microwaves in Medicine”. In: *Advances in Cancer Therapy*. Ed. by H. Gali-Muhtasib. London: IntechOpen, 2011. Chap. 23. DOI: 10.5772/22939. URL: https://doi.org/10.5772/22939.

[133] J. C. Wang et al. “Two Methods of SAR Measurement for Wearable Electronic Devices”. In: URL: https://api.semanticscholar.org/CorpusID:32225036.

[134] J. Croteau et al. “Phantoms for testing radar-based microwave breast imaging”. In: *2009 13th International Symposium on Antenna Technology and Applied Electromagnetics and the Canadian Radio Science Meeting*. 2009, pp. 1–4. DOI: 10.1109/ANTEMURSI.2009.4805059.

[135] A. T. Mobashsher and A. M. Abbosh. “Artificial Human Phantoms: Human Proxy in Testing Microwave Apparatuses That Have Electromagnetic Interaction with the Human Body”. In: *IEEE Microwave Magazine* 16.6 (2015), pp. 42–62. DOI: 10.1109/MMM.2015.2419772.

[136] F. Karimi et al. “Method and Implementations to Measure the Absorbed Power Density”. In: *2022 IEEE MTT-S International Microwave Biomedical Conference (IMBioC)*. 2022, pp. 129–131. DOI: 10.1109/IMBioC52515.2022.9790128.

[137] N. Chitnis et al. “Traceable Assessment of the Absorbed Power Density of Body Mounted Devices at Frequencies Above 10 GHz”. In: *Bioelectromagnetics* 46.6 (2025), e70018. DOI: `https://doi.org/10.1002/bem.70018`. eprint: `https://onlinelibrary.wiley.com/doi/pdf/10.1002/bem.70018`. URL: `https://onlinelibrary.wiley.com/doi/abs/10.1002/bem.70018`.

[138] S. F. Jafari et al. “Absorbed/Epithelial Power Density Assessment Using Plane-Wave Spectrum Method From Inside the Skin Tissue Above 6 GHz”. In: *IEEE Transactions on Instrumentation and Measurement* 71 (2022), pp. 1–8. DOI: `10.1109/TIM.2022.3167770`.

[139] L. Vähä-Savo et al. “Empirical Evaluation of a 28 GHz Antenna Array on a 5G Mobile Phone Using a Body Phantom”. In: *IEEE Transactions on Antennas and Propagation* 69.11 (2021), pp. 7476–7485. DOI: `10.1109/TAP.2021.3076535`.

[140] T. Kobayashi et al. “Dry phantom composed of ceramics and its application to SAR estimation”. In: *IEEE Transactions on Microwave Theory and Techniques* 41.1 (1993), pp. 136–140. DOI: `10.1109/22.210240`.

[141] T. Nojima et al. “Ceramic dry-phantom and its application to SAR estimation”. In: *1991 IEEE MTT-S International Microwave Symposium Digest*. 1991, 189–192 vol.1. DOI: `10.1109/MWSYM.1991.146959`.

[142] H. Tamura et al. “A dry phantom material composed of ceramic and graphite powder”. In: *IEEE Transactions on Electromagnetic Compatibility* 39.2 (1997), pp. 132–137. DOI: `10.1109/15.584935`.

[143] T. Iyama et al. “Novel Specific Absorption Rate (SAR) Measurement Method Using a Flat Solid Phantom”. In: *IEEE Transactions on Electromagnetic Compatibility* 50.1 (2008), pp. 43–51. DOI: `10.1109/TEMC.2007.913216`.

[144] J. Chang et al. “A conductive plastic for simulating biological tissue at microwave frequencies”. In: *IEEE Transactions on Electromagnetic Compatibility* 42.1 (2000), pp. 76–81. DOI: `10.1109/15.831707`.

[145] I. Youngs et al. “Design of solid broadband human tissue simulant materials”. In: *Science, Measurement and Technology, IEE Proceedings* - 149 (Dec. 2002), pp. 323–328. DOI: `10.1049/ip-smt:20020647`.

[146] Y. Nikawa, M. Chino, and K. Kikuchi. "Soft and dry phantom modeling material using silicone rubber with carbon fiber". In: *IEEE Transactions on Microwave Theory and Techniques* 44.10 (1996), pp. 1949–1953. DOI: 10.1109/22.539954.

[147] T. Hikage et al. "Development of Lightweight Solid Phantom Composed of Silicone Rubber and Carbon Nanotubes". In: *2007 IEEE International Symposium on Electromagnetic Compatibility*. 2007, pp. 1–4. DOI: 10.1109/ISEMC.2007.213.

[148] C. Gabriel. "Tissue equivalent material for hand phantoms". In: *Physics in medicine and biology* 52 (Aug. 2007), pp. 4205–10. DOI: 10.1088/0031-9155/52/14/012.

[149] *SPEAG — Phantom Components Overview*. https://speag.swiss/components/phantoms/overview-2/. Accessed: 2025-11-23.

[150] T. Hikage et al. "Novel 60 GHz Band Spatial Synthetic Exposure Setup to Investigate Biological Effects of 5G and Beyond Wireless Systems on Human Body". In: *Frontiers in Public Health* Volume 9 - 2021 (2021). ISSN: 2296-2565. DOI: 10.3389/fpubh.2021.777712. URL: https://www.frontiersin.org/journals/public-health/articles/10.3389/fpubh.2021.777712.

[151] J. Garrett and E. Fear. "A New Breast Phantom With a Durable Skin Layer for Microwave Breast Imaging". In: *IEEE Transactions on Antennas and Propagation* 63.4 (2015), pp. 1693–1700. DOI: 10.1109/TAP.2015.2393854.

[152] D. Nishihara et al. "Development of Measurement Phantom for Absorbed Power Density Assessment by Human Exposure at 28 GHz Band". In: *IEEE Journal of Electromagnetics, RF and Microwaves in Medicine and Biology* 9.2 (2025), pp. 191–197. DOI: 10.1109/JERM.2024.3419026.

[153] A. R. Guraliuc et al. "Solid Phantom for Body-Centric Propagation Measurements at 60 GHz". In: *IEEE Transactions on Microwave Theory and Techniques* 62.6 (2014), pp. 1373–1380. DOI: 10.1109/TMTT.2014.2320691.

[154] M. Ziane et al. "Novel Technique for In-Body Absorbed Power Density Assessment Based on Free-Space E-Field Measurement". In: *IEEE Transactions on Microwave Theory and Techniques* 72.7 (2024), pp. 4127–4138. DOI: 10.1109/TMTT.2023.3336798.

[155] R. Rizzo et al. "Electrotextile-Based Flexible Electromagnetic Skin for Wearables and Remote Monitoring". In: *IEEE Journal of Microwaves* 5.1 (2025), pp. 23–33. DOI: 10.1109/JMW.2024.3504846.

[156] A. R. Guraliuc, M. Zhadobov, and R. Sauleau. "PDMS-based skin-equivalent phantom for propagation studies in the 58–63 GHz range". In: *2014 4th International Conference on Wireless Mobile Communication and Healthcare - Transforming Healthcare Through Innovations in Mobile and Wireless Technologies (MOBIHEALTH)*. 2014, pp. 196–198. DOI: 10.4108/Mobihealth33544.2014.7015944.

[157] M. Ziane, M. Zhadobov, and R. Sauleau. "High-Resolution Technique for Near-Field Power Density Measurement Accounting for Antenna/Body Coupling at Millimeter Waves". In: *IEEE Antennas and Wireless Propagation Letters* 20.11 (2021), pp. 2151–2155. DOI: 10.1109/LAWP.2021.3087019.

[158] M. Ziane, A. Boriskin, and M. Zhadobov. "Near-Field Power Density Mapping of Close-to-Body Low-Power mmWave Devices". In: *IEEE Antennas and Wireless Propagation Letters* 22.10 (2023), pp. 2347–2351. DOI: 10.1109/LAWP.2023.3286944.

[159] M. Ziane, M. Zhadobov, and R. Sauleau. "High-resolution near-field measurements accounting for antenna/body coupling around 60 GHz". In: *2021 XXXIVth General Assembly and Scientific Symposium of the International Union of Radio Science (URSI GASS)*. 2021, pp. 01–03. DOI: 10.23919/URSIGASS51995.2021.9560582.

[160] Schmid & Partner Engineering AG (SPEAG). *DASY8 Module APD (10–45 GHz)*. https://speag.swiss/products/dasy8/m-apd/. Accessed 2 January 2026. 2025.

[161] C. Lee et al. "A Reduction Method of Phantom Shell Effects for APD Extraction Using Negative Permittivity Material". In: *IEEE Access* 12 (2024), pp. 134862–134873. DOI: 10.1109/ACCESS.2024.3460754.

[162] M. Zhadobov, M. Ziane, and A. Boriskin. "Novel Method for APD Evaluation Based on Artificial Electromagnetic Skin". In: Jan. 2024. DOI: 10.46620/URSIATRASC24/STVS5473.

[163] M. Ziane, A. Boriskin, and M. Zhadobov. “Conceptually New IR-Based Approach for Fast User Exposure Compliance Testing Above 6 GHz”. In: *2025 19th European Conference on Antennas and Propagation (EuCAP).* 2025, pp. 1–4. DOI: 10.23919/EuCAP63536.2025.10999726.

[164] M. Ziane, M. Zhadobov, and R. Sauleau. “Increase of exposure levels due to antenna/body coupling in the 60-GHz band”. In: *2021 XXXIVth General Assembly and Scientific Symposium of the International Union of Radio Science (URSI GASS).* 2021, pp. 1–4. DOI: 10.23919/URSIGASS51995.2021.9560521.

[165] G. Franceschetti et al. “A tool for planning electromagnetic field levels in urban areas”. In: *IEEE Antennas and Propagation Society Symposium, 2004.* Vol. 3. 2004, 2211–2214 Vol.3. DOI: 10.1109/APS.2004.1331808.

[166] G. Franceschetti et al. *VERIFICA DI UN SOFTWARE PER LA PREVISIONE DELLA RADIOCOPERTURA.* URL: https://www.researchgate.net/publication/265916911_VERIFICA_DI_UN_SOFTWARE_PER_LA_PREVISIONE_DELLA_RADIOCOPERTURA.

[167] G. Liang and H. Bertoni. “A new approach to 3-D ray tracing for propagation prediction in cities”. In: *IEEE Transactions on Antennas and Propagation* 46.6 (1998), pp. 853–863. DOI: 10.1109/8.686774.

[168] G. Franceschetti, A. lodice, and D. Riccio. “Chapter 1.6.5 - Fractal Models for Scattering from Natural Surfaces”. In: *Scattering.* Ed. by R. Pike and P. Sabatier. London: Academic Press, 2002, pp. 467–485. ISBN: 978-0-12-613760-6. DOI: https://doi.org/10.1016/B978-012613760-6/50024-3. URL: https://www.sciencedirect.com/science/article/pii/B9780126137606500243.

[169] G. Franceschetti and D. Riccio. *Scattering, Natural Surfaces, and Fractals.* Academic Press, 2006. ISBN: 9780080469010. URL: https://books.google.it/books?id=v7pxQiUv9BgC.

[170] R. Luebbers. “Finite conductivity uniform GTD versus knife edge diffraction in prediction of propagation path loss”. In: *IEEE Transactions on Antennas and Propagation* 32.1 (1984), pp. 70–76. DOI: 10.1109/TAP.1984.1143189.

[171] G. Franceschetti. *Electromagnetics: Theory, Techniques, and Engineering Paradigms.* Language of science. Springer US, 2013. ISBN: 9781489902573. URL: https://books.google.it/books?id=jW4ECAAAQBAJ.

[172] G. Franceschetti et al. "Scattering From Layered Structures With One Rough Interface: A Unified Formulation of Perturbative Solutions". In: *IEEE Transactions on Geoscience and Remote Sensing* 46.6 (2008), pp. 1634–1643. DOI: 10.1109/TGRS.2008.916222.

[173] A. Garzia et al. "Human exposure to electromagnetic fields for new wireless technologies and frequencies: software characterization study". In: *2023 AEIT International Annual Conference (AEIT)*. 2023, pp. 1–6. DOI: 10.23919/AEIT60520.2023.10330410.

[174] I. Onwuegbuzie. "5G: Next Generation Mobile Wireless Technology for A Fast Pacing World". In: *Journal for Pure and Applied Sciences (JPAS)* 1 (June 2022), pp. 1–9.

[175] OpenStreetMap contributors. *OpenStreetMap database*. https://www.openstreetmap.org. Data available under the Open Database License (ODbL). Accessed: 28 November 2025. 2025.

[176] Google Earth. *Google Earth imagery / map*. https://earth.google.com/web/. Image / data from Google Earth. Accessed: 28 November 2025. 2025.

[177] F. Lodato et al. "Planning 5G Non-public Network In A Real Hospital-case Scenario: A Ray Tracing Simulation Study". In: *BIOEM2024 Proceedings*. 2024.

[178] *Commission Implementing Regulation (EU) 2020/1070 of 20 July 2020 amending Implementing Regulation (EU) 2015/1998 as regards the clarification, harmonisation and simplification of certain specific aviation security measures*. Official Journal of the European Union, L 234, 21 July 2020, pp. 6–9. OJ L 234, 21.7.2020, p. 6. 2020. URL: https://eur-lex.europa.eu/legal-content/EN/TXT/?uri=CELEX%3A32020R1070.

[179] International Electrotechnical Commission. *IEC 60601-1-2:2014+AMD1:2020 CSV — Medical electrical equipment — Part 1-2: General requirements for basic safety and essential performance — Collateral standard: Electromagnetic disturbances — Requirements and tests*. IEC, 2020. URL: https://webstore.iec.ch/en/publication/2590.

[180] F. Lodato et al. "Ray Tracing Simulation Study on a Real 27 GHz Case Scenario". In: *2024 IEEE International Symposium on Antennas and Propagation and INC/USNC-URSI Radio Science Meeting (AP-S/INC-USNC-*

URSI). 2024, pp. 1635–1636. DOI: 10.1109/AP-S/INC-USNC-URSI52054.2024.10687093.

[181] F. Lodato et al. “Ray Tracing Modeling of 5G Non-Public Networks Operating at 26 GHz in Healthcare Environments”. In: *BIOEM2025 Proceedings*. 2025.

[182] F. Lodato et al. “Ray Tracing Tools Assessment for the Evaluation of EMF Levels Generated by 5G NR Systems: An Overview”. In: *2024 IEEE International Symposium on Measurements Networking (MN)*. 2024, pp. 1–6. DOI: 10.1109/MN60932.2024.10615802.

[183] CEI. *Guideline for the measurement and assessment of electromagnetic fields in the frequency range 10 kHz - 300 GHz, with reference to human exposure*. CEI Classification: 211-7, Issue n. 5909, p. 92. Jan. 2001.

[184] E. Damosso and L. M. Correia, eds. *Digital Mobile Radio Towards Future Generation Systems*. COST Action 231 Final Report. Luxembourg: Office for Official Publications of the European Communities, 1999.

[185] F. Lodato et al. “Ray Tracing Tools Intercomparison for the Study of 5G Signal Propagation in Urban Scenarios”. In: *2024 4th URSI Atlantic Radio Science Meeting (AT-RASC)*. 2024, pp. 1–4. DOI: 10.46620/URSIATRASC24/CBEO9331.

[186] F. Lodato et al. “A Comparative Study for Ray Tracing Tools Assessment in 5G Scenarios: From Numerical to Experimental Analysis”. In: *2025 AEIT International Annual Conference (AEIT)*. 2025, pp. 1–6. DOI: 10.23919/AEIT67669.2025.11218129.

[187] A. V. Militaru et al. “Validation of Real-world Measurements Through Ray Tracing Simulation for 5G Urban Scenarios”. In: *2024 International Symposium on Electronics and Telecommunications (ISETC)*. 2024, pp. 1–4. DOI: 10.1109/ISETC63109.2024.10797276.

[188] G. Fokin, V. Starikov, and V. Sevidov. “Radio Coverage Estimation and Ray Tracing with Digital Terrain Models in the Matlab Environment”. In: *2025 Wave Electronics and its Application in Information and Telecommunication Systems (WECONF)*. 2025, pp. 1–6. DOI: 10.1109/WECONF65186.2025.11017262.

[189] M. G. Aram et al. "Site-Specific Outdoor Propagation Assessment and Ray-Tracing Analysis for Wireless Digital Twins". In: *2025 19th European Conference on Antennas and Propagation (EuCAP)*. 2025, pp. 1–5. DOI: 10.23919/EuCAP63536.2025.10999688.

[190] M. M. Ahamed and S. Faruque. "5G Network Coverage Planning and Analysis of the Deployment Challenges". In: *Sensors* 21.19 (2021). ISSN: 1424-8220. DOI: 10.3390/s21196608. URL: https://www.mdpi.com/1424-8220/21/19/6608.

[191] Rohde & Schwarz GmbH & Co. KG. *R&S® TSMA6B Autonomous Mobile Network Scanner*. Rohde & Schwarz. 2024. URL: https://www.rohde-schwarz.com/.

[192] Forsk S.A. *ASTER Propagation Model*. https://www.forsk.com/aster-propagation-model. Accessed: 2025-11-09. 2025.

[193] COST Action 231. *Urban Transmission Loss Models for Mobile Radio in the 900 and 1800 MHz Bands*. Technical Report. European Communities, Sept. 1991.

[194] J. Deygout. "Multiple knife-edge diffraction of microwaves". In: *IEEE Transactions on Antennas and Propagation* 14.4 (1966), pp. 480–489. DOI: 10.1109/TAP.1966.1138719.

[195] J. Gonzalez, A. Nájera López, and C. Garcia-Pardo. "Dual Evaluation and Spatial Analysis of RF-EMF Exposure in 5G: Theoretical Extrapolations and Direct Measurements". In: *Bioelectromagnetics* 46 (Aug. 2025). DOI: 10.1002/bem.70020.

[196] A. Manukyan et al. "On the Limitations of Ray-Tracing for Learning-Based RF Tasks in Urban Environments". In: (July 2025). DOI: 10.48550/arXiv.2507.19653.

[197] M. Born, E. Wolf, and A. Bhatia. *Principles of Optics: Electromagnetic Theory of Propagation, Interference and Diffraction of Light*. Cambridge University Press, 2000. ISBN: 9780521784498. URL: https://books.google.it/books?id=oV80AAAAIAAJ.

[198] F. Abelès. "Recherches sur la propagation des ondes électromagnétiques sinusoıdales dans les milieux stratifiés-Application aux couches minces". In: *Annales de physique*. Vol. 12. 5. EDP Sciences. 1950, pp. 596–640.

[199] H. H. Pennes. "Analysis of Tissue and Arterial Blood Temperatures in the Resting Human Forearm". In: *Journal of Applied Physiology* 85.1 (1998), pp. 5–34. DOI: 10.1152/jappl.1998.85.1.5.

[200] C. Leduc, M. Zhadobov, and R. Sauleau. "Thermal model of skin-equivalent phantoms at 60 GHz". In: *2015 European Microwave Conference (EuMC)*. 2015, pp. 698–701. DOI: 10.1109/EuMC.2015.7345859.

[201] C. Leduc and M. Zhadobov. "Thermal Model of Electromagnetic Skin-Equivalent Phantom at Millimeter Waves". In: *IEEE Transactions on Microwave Theory and Techniques* 65.3 (2017), pp. 1036–1045. DOI: 10.1109/TMTT.2016.2638816.

[202] K. R. Foster, H. N. Kritikos, and H. P. Schwan. "Effect of Surface Cooling and Blood Flow on the Microwave Heating of Tissue". In: *IEEE Transactions on Biomedical Engineering* BME-25.3 (1978), pp. 313–316. DOI: 10.1109/TBME.1978.326313.

[203] F. Incropera et al. *Principles of Heat and Mass Transfer*. John Wiley & Sons Singapore Pte. Limited, 2013. ISBN: 9788126542734. URL: https://books.google.it/books?id=UTJ0CgAAQBAJ.

[204] G. V. Morozov, R. G. Maev, and G. W. F. Drake. "Multiple reflection method for electromagnetic waves in layered dielectric structures". In: *Quantum Electronics* 31.9 (Sept. 2001), p. 767. DOI: 10.1070/QE2001v031n09ABEH002042. URL: https://doi.org/10.1070/QE2001v031n09ABEH002042.

[205] M. Ziane, R. Sauleau, and M. Zhadobov. "Antenna/Body Coupling in the Near-Field at 60 GHz: Impact on the Absorbed Power Density". In: *Applied Sciences* 10.21 (2020). ISSN: 2076-3417. DOI: 10.3390/app10217392. URL: https://www.mdpi.com/2076-3417/10/21/7392.

[206] D. Pozar. *Microwave Engineering*. Wiley, 2012. ISBN: 9781118213636. URL: https://books.google.nl/books?id=JegbAAAAQBAJ.

[207] "Integral Transform Technique". In: *Heat Conduction*. John Wiley Sons, Ltd, 2012. Chap. 14, pp. 547–613. ISBN: 9781118411285. DOI: https://doi.org/10.1002/9781118411285.ch14. eprint: https://onlinelibrary.wiley.com/doi/pdf/10.1002/9781118411285.ch14. URL: https://onlinelibrary.wiley.com/doi/abs/10.1002/9781118411285.ch14.

[208] C. Gabriel. “Compilation of the Dielectric Properties of Body Tissues at RF and Microwave Frequencies.” In: 1996. URL: https://api.semanticscholar.org/CorpusID:108808148.

[209] C. Baumgartner et al. *IT’IS Database for thermal and electromagnetic parameters of biological tissues*. Version 5.0. Aug. 2025. DOI: 10.13099/VIP21000-05-0. URL: https://itis.swiss/database.

[210] R. Rizzo et al. “Electrotextile-Based Flexible Electromagnetic Skin for Wearables and Remote Monitoring”. In: *IEEE Journal of Microwaves* 5 (2025), pp. 23–33. URL: https://api.semanticscholar.org/CorpusID:274931883.

[211] Schmid & Partner Engineering AG. *OTA Phantoms – Overview*. 2025. URL: https://speag.swiss/products/em-phantoms/overview-2/ (visited on 11/13/2025).

[212] M. Hotta et al. “Complex Permittivity of Graphite, Carbon Black and Coal Powders in the Ranges of X-band Frequencies (8.2 to 12.4 GHz) and between 1 and 10 GHz”. In: *ISIJ International* 51.11 (2011), pp. 1766–1772. DOI: 10.2355/isijinternational.51.1766.

[213] E. Gümüş, M. Yağımlı, and E. Arca. “Investigation of the Dielectric Properties of Graphite and Carbon Black-Filled Composites as Electromagnetic Interference Shielding Coatings”. In: *Applied Sciences* 13.15 (2023). ISSN: 2076-3417. DOI: 10.3390/app13158893. URL: https://www.mdpi.com/2076-3417/13/15/8893.

[214] F. Shkal et al. “Microwave Characterization of Activated Carbons”. In: *Journal of Computer and Communications* 06 (Jan. 2018), pp. 112–123. DOI: 10.4236/jcc.2018.61012.

[215] J. Atwater and R. Wheeler. “Complex Permittivities and Dielectric Relaxation of Granular Activated Carbons at Microwave Frequencies Between 0.2 and 26 GHz”. In: *Carbon* 41 (Dec. 2003), pp. 1801–1807. DOI: 10.1016/S0008-6223(03)00150-7.

[216] A. Sihvola and I. of Electrical Engineers. *Electromagnetic Mixing Formulas and Applications*. IEE electromagnetic waves series. Institution of Electrical Engineers, 1999. ISBN: 9780852967720. URL: https://books.google.nl/books?id=uIHSNwxBxjgC.

[217] K. T. Chung, A. Sabo, and A. P. Pica. "Electrical permittivity and conductivity of carbon black-polyvinyl chloride composites". In: *Journal of Applied Physics* 53.10 (Oct. 1982), pp. 6867–6879. ISSN: 0021-8979. DOI: 10.1063/1.330027. eprint: https://pubs.aip.org/aip/jap/article-pdf/53/10/6867/18398747/6867_1_online.pdf. URL: https://doi.org/10.1063/1.330027.

[218] H. Shivashankar et al. "Study on low-frequency dielectric behavior of the carbon black/polymer nanocomposite". In: *Journal of Materials Science: Materials in Electronics* 32 (2021), pp. 28674–28686. URL: https://api.semanticscholar.org/CorpusID:240231230.

[219] D. C. Dube. "Study of Landau-Lifshitz-Looyenga's formula for dielectric correlation between powder and bulk". In: *Journal of Physics D: Applied Physics* 3.11 (Nov. 1970), p. 1648. DOI: 10.1088/0022-3727/3/11/313. URL: https://doi.org/10.1088/0022-3727/3/11/313.

[220] H. Looyenga. "Dielectric constants of heterogeneous mixtures". In: *Physica* 31.3 (1965), pp. 401–406. ISSN: 0031-8914. DOI: https://doi.org/10.1016/0031-8914(65)90045-5. URL: https://www.sciencedirect.com/science/article/pii/0031891465900455.

[221] E. Tuncer and G. A. Niklasson. "Properties of bruggeman dielectric mixture expression". In: *2014 IEEE Conference on Electrical Insulation and Dielectric Phenomena (CEIDP)*. 2014, pp. 875–878. DOI: 10.1109/CEIDP.2014.6995867.

[222] D. Dube and R. Parshad. "Study of Böttcher's formula for dielectric correlation between powder and bulk". In: *Journal of Physics D: Applied Physics* 3 (May 2002), p. 677. DOI: 10.1088/0022-3727/3/5/306.

[223] C. Böttcher et al. *Theory of Electric Polarization: Dielectrics in Static Fields*. Dielectrics in Static Fields. Elsevier Science, 1973. ISBN: 9780444410191. URL: https://books.google.nl/books?id=7OcntQEACAAJ.

[224] A. Kumar, S. Sharma, and G. Singh. "Measurement of dielectric constant and loss factor of the dielectric material at microwave frequencies". In: *Progress in Electromagnetic Research* 69 (Jan. 2007), pp. 47–54. DOI: 10.2528/PIER06111204.

[225] S. Khanal et al. “Measurement of Dielectric Properties at 75 -325 GHz using a Vector Network Analyzer and Full Wave Simulator”. In: *Radioengineering* 21 (June 2012).

Copyright Statements

Curriculum Vitae

Short Bio

Francesca Lodato received the M.Sc. degree in biomedical engineering from the University of Naples "Federico II," Naples, Italy, in 2022, where she is currently pursuing the Ph.D. degree in applied physics. Current work involves the evaluation of human exposure in 5G scenarios by means of analytical, numerical, and experimental approaches. Her main research interests deal with the study of interaction between electromagnetic fields and biological systems in the range of nonionizing frequencies for different fields of application: electroporation-based treatments, ablation techniques, 5G systems, microwave heating, design and development of MRI phantoms, and numerical and experimental dosimetry. She is the winner of the "France Excellence Eiffel scholarship program 2024" and in 2024 she received the "Best Student Paper Award" at 2024 IEEE Sensors Applications Symposium with the work entitled "Numerical Modeling of Monopolar Radio Frequency Ablation and Experimental Validation through Fiber Bragg Gratings Sensors".

Education

2023 – Present

Ph.D. in Physics, University of Naples Federico II

2021 – 2022

M.Sc. in Biomedical Engineering (Medical Devices) *cum laude*, University of Naples Federico II

2017 – 2022

B.Sc. in Biomedical Engineering, University of Naples Federico II

Work Experience

06/2022 – 10/2022

Biomedical research internship, National Research Council of Italy (CNR), Naples, Italy

List of Publications (Peer-Reviewed)

[1] A. Garzia et al. "Human exposure to electromagnetic fields for new wireless technologies and frequencies: software characterization study". In: *2023 AEIT International Annual Conference (AEIT)*. 2023, pp. 1–6. DOI: 10.23919/AEIT60520.2023.10330410.

[2] F. Lodato et al. "Ray Tracing Tools Intercomparison for the Study of 5G Signal Propagation in Urban Scenarios". In: *2024 4th URSI Atlantic Radio Science Meeting (AT-RASC)*. 2024, pp. 1–4. DOI: 10.46620/URSIATRASC24/CBEO9331.

[3] F. Lodato et al. "Thermal Analysis of Ex-Vivo Liver RF Ablation through Numerical Modeling and Fiber Bragg Gratings Validation". In: *2024 4th URSI Atlantic Radio Science Meeting (AT-RASC)*. 2024, pp. 1–4. DOI: 10.46620/URSIATRASC24/HHWG7383.

[4] R. Massa et al. "Preliminary Results on Fungicidal Efficacy of Microwave Treatment on Fusarium oxysporum". In: *2024 4th URSI Atlantic Radio Science Meeting (AT-RASC)*. 2024, pp. 1–4. DOI: 10.46620/URSIATRASC24/DCKD7279.

[5] F. Lodato et al. "Planning 5G Non-public Network In A Real Hospital-case Scenario: A Ray Tracing Simulation Study". In: *BIOEM2024 Proceedings*. 2024.

[6] F. Lodato et al. "Ray Tracing Tools Assessment for the Evaluation of EMF Levels Generated by 5G NR Systems: An Overview". In: *2024 IEEE International Symposium on Measurements Networking (MN)*. 2024, pp. 1–6. DOI: 10.1109/MN60932.2024.10615802.

[7] F. Lodato et al. "Ray Tracing Simulation Study on a Real 27 GHz Case Scenario". In: *2024 IEEE International Symposium on Antennas and Propagation and INC/USNC-URSI Radio Science Meeting (AP-S/INC-USNC-URSI)*. 2024, pp. 1635–1636. DOI: 10.1109/AP-S/INC-USNC-URSI52054.2024.10687093.

[8] F. Lodato et al. "Numerical Modeling of Monopolar Radio Frequency Ablation and Experimental Validation Through Fiber Bragg Gratings Sensors". In: *2024 IEEE Sensors Applications Symposium (SAS)*. 2024, pp. 1–6. DOI: 10.1109/SAS60918.2024.10636481.

[9] F. Lodato et al. "Radio Frequency Ablation of Liver Tissue Assisted by Saline Infusion: Computational Modeling and Experimental Assessment". In: *IEEE Transactions on Instrumentation and Measurement* 74 (2025), pp. 1–11. DOI: 10.1109/TIM.2025.3563053.

[10] F. Lodato et al. "Ray Tracing Modeling of 5G Non-Public Networks Operating at 26 GHz in Healthcare Environments". In: *BIOEM2025 Proceedings*. 2025.

[11] F. Lodato et al. "Advanced Phantoms For IR-Based APD Measurement At mmWaves: SNR Enhancement Through Multi-Physics Phantom Optimisation". In: *BIOEM2025 Proceedings*. 2025.

[12] F. Lodato et al. "A Comparative Study for Ray Tracing Tools Assessment in 5G Scenarios: From Numerical to Experimental Analysis". In: *2025 AEIT International Annual Conference (AEIT)*. 2025, pp. 1–6. DOI: 10.23919/AEIT67669.2025.11218129.

[13] U. Spagnolini et al. "High Frequency Wireless RESTART Spoke3 Laboratories: From Devices to Networks". In: *2025 AEIT International Annual Conference (AEIT)*. 2025, pp. 1–6. DOI: 10.23919/AEIT67669.2025.11218102.

[14] N. D'Ambrosio et al. "Microwave-Induced Inhibition of Germination in Portulaca oleracea L. Seeds". In: *Agronomy* 15.10 (2025). ISSN: 2073-4395. DOI: 10.3390/agronomy15102418. URL: https://www.mdpi.com/2073-4395/15/10/2418.

Awards

- Best Student Paper Award at *2024 IEEE Sensors Applications Symposium (SAS)* with the paper entitled "Numerical Modeling of Monopolar Radio Frequency Ablation and Experimental Validation Through Fiber Bragg Gratings Sensors"
- Winner of the "France Excellence Program 2024" for the presented PhD thesis project proposal

International Conferences and Workshops Presentations

- *RESTART Plenary Dissemination Workshop* - 20-21 July 2023, Bari, Italy
- *AEIT International Annual Conference 2023* - 5-7 October 2023, Rome, Italy
- *RESTART Plenary Dissemination Workshop* - 30-31 January 2024, Bologna, Italy
- *4th URSI Atlantic Radio Science Meeting 2024* - 19-24 May 2024, Gran Canaria, Spain
- *BioEM 2024* - 16-21 June 2024, Crete, Greece
- *2024 IEEE International Symposium on Antennas and Propagation and ITNC-USNC-URSI Radio Science Meeting* - 14-19 July 2024, Florence, Italy
- *2024 IEEE Sensors Applications Symposium (SAS)* - 23-25 July 2024, Naples, Italy
- *BioEM 2025* - 22-27 June 2025, Rennes, France
- *RESTART Plenary Dissemination Workshop* - 30 June-2 July 2025, Naples, Italy

Projects

RESTART “RESearch and innovation on future Telecommunications systems and networks, to make Italy more smart”, 6GWINET: coordination of project partners, research activities, dissemination of results at meetings and conferences.

Certifications

- "*Antenna Modeling and Simulation Made Easy Fundamentals and Hands-on Exercises*", International ELEDIA Talent Research Program 2023 - ELEDIA Research Center, 2023
- "*Training for European Projects Proposal*" - Intellera Consulting S.p.a., 2023

Teaching Experience

Presented Seminar Lectures:

- "*Electromagnetical Dosimetry: numerical simulations and experimental validation*", M.Sc. courses
- "*Electroporation: from biophysics mechanisms to applications*", M.Sc. courses
- "*Finite Element Method for ablation techniques*", Doctoral course

Teaching Assignments:

- Didactical support for three B.Sc. Physics courses at the Department of Industrial Engineering - University of Naples Federico II

Thesis Supervised:

- "*Design, Development and Electromagnetic Characterization of Solid Phantoms Based on Sucrose and NaCl*", M.Sc. Thesis
- "*Design, Development and Electromagnetic Characterization of Solid Phantoms based on Oils and Surfactants*", M.Sc. Thesis
- "*Radiofrequency and Microwave Ablation of Liver Tumors: a Comparative Analysis of the Techniques*", B.Sc. Thesis
- "*Electrodes for the Thermal Ablation Of Tumors: Physical Principles and Technological Solutions*", B.Sc. Thesis

- "*Development of an Analytical Model for the Electromagnetic Design of Glucose-Based Phantoms*", M.Sc. Thesis
- "*Electromagnetic, Numerical and Experimental Characterization of PVP-Based Phantoms for Ultra-High Field Magnetic Resonance Applications*", M.Sc. Thesis
- "*Development and Realization of Phantoms for High-Field Magnetic Resonance Imaging*", M.Sc. Thesis
- "*Parametric Study for the Optimisation of Tumour Treatments through Radiofrequency Ablation*", M.Sc. Thesis